



저작자표시-비영리-변경금지 2.0 대한민국

이용자는 아래의 조건을 따르는 경우에 한하여 자유롭게

- 이 저작물을 복제, 배포, 전송, 전시, 공연 및 방송할 수 있습니다.

다음과 같은 조건을 따라야 합니다:



저작자표시. 귀하는 원저작자를 표시하여야 합니다.



비영리. 귀하는 이 저작물을 영리 목적으로 이용할 수 없습니다.



변경금지. 귀하는 이 저작물을 개작, 변형 또는 가공할 수 없습니다.

- 귀하는, 이 저작물의 재이용이나 배포의 경우, 이 저작물에 적용된 이용허락조건을 명확하게 나타내어야 합니다.
- 저작권자로부터 별도의 허가를 받으면 이러한 조건들은 적용되지 않습니다.

저작권법에 따른 이용자의 권리는 위의 내용에 의하여 영향을 받지 않습니다.

이것은 [이용허락규약\(Legal Code\)](#)을 이해하기 쉽게 요약한 것입니다.

[Disclaimer](#)

공학박사 학위논문

**Reflection traveltime tomography using
approximate stationary points**

근사 stationary point 를 이용한 반사주시
토모그래피

2019 년 8 월

서울대학교 대학원
에너지시스템공학부
이 향 월

Abstract

Reflection travelttime tomography using approximate stationary points

Xiangyue Li

Department of Energy Systems Engineering

The Graduate School

Seoul National University

Reflection travelttime tomography has been used to describe subsurface velocity structures in practice, which can be used as a background or initial model for prestack depth migration or full waveform inversion. Conventional reflection travelttime tomography is performed by solving an optimization problem based on a ray tracing method. As a result, reflection travelttime tomography requires heavy computational effort to carry out ray tracing and solve a large matrix equation. In addition, like most data-domain tomography methods, reflection travelttime tomography depends on initial guesses and suffers from non-uniqueness and uncertainty of solutions.

In this study, I propose a deterministic ray-based reflection travelttime tomography method by applying seismic interferometry, and this method does not suffer from the non-uniqueness problem and does not require *a priori* information on subsurface media. By adding a virtual layer on the top

of the real surface (whose properties are known) and applying convolution-type interferometry, I approximately determine the stationary points (i.e., incident raypaths in the virtual layer). In the case that we already know the information on the first real layer, correlation-type interferometry also can be used to determine stationary points. Then, I generate reflection points for a range of assumed velocities and estimate the velocity by considering the number of reflection points and traveltimes difference between the observed and calculated data instead of solving the conventional tomographic matrix. The reflection surface can then be recovered by using the estimated velocity. Once the first target layer is resolved, we can recover the whole media by recursively applying the same method to the lower layers.

Numerical examples using surface seismic profile data for homogeneous and inhomogeneous models and real field data (Congo data set) demonstrate that the proposed method successfully recovers the velocity and depth of subsurface media without initial guesses. However, the proposed method has some limitations for multi-layer models because the method does not yield sufficient reflection points for the deeper layers.

Keywords: reflection traveltimes tomography, seismic inversion, velocity estimation, non-uniqueness problem, ray tracing, seismic interferometry, stationary point, angle of incidence

Student number: 2013-30780

Contents

Abstract.....	i
Contents	iii
List of Tables	vii
List of Figures	ix
1 Introduction	1
1.1 Seismic tomography methods	1
1.2 Seismic interferometry	5
1.3 Objective and outline.....	8
2 Basic theory of traveltime interferometry.....	10
2.1 Principle of Fermat's interferometry.....	11
2.1.1 Correlation-type interferometry	11
2.1.2 Convolution-type interferometry.....	14
2.2 Characteristics of SI	16
2.2.1 Characteristic of correlation-type SI.....	16
2.2.2 Characteristic of convolution-type SI.....	21
3 Estimation of P-wave velocity and interface	25
3.1 Determination of approximate stationary point	26

3.2 Determination of approximate stationary points without <i>a priori</i> information	28
3.3 Estimation of P-wave velocity	31
3.3.1 Estimation of reflection point for target layer	32
3.3.2 Estimation of P-wave velocity	34
3.4 Estimation of interface	40
3.5 The main procedures of estimation method.....	42
3.6 Sensitivity analysis.....	45
3.6.1 Sensitivity to the accuracy of traveltime picking	45
3.6.2 Accuracy analysis on the slope of reflection surface	51
4 Applications of convolution-type SI.....	63
4.1 The homogeneous-layer model.....	64
4.2 The inhomogeneous-layer model.....	71
4.3 Fault model	77
4.4 Real data	92
4.5 Discussion.....	100
5 Comparison of different wave combinations	106
5.1 The homogeneous-layer model.....	109
5.2 The inhomogeneous-layer model.....	121
5.3 Discussion.....	128
6 Conclusions	130
References	132

초 록.....	138
-------------	-----

List of Tables

Table 3.1 Geometry of source and receiver used in Figure 3.13.....	55
Table 5.1 Velocities estimated by using three different types of combinations for the homogeneous-layer model.	120
Table 5.2 Velocities estimated by using three different types of combinations for the inhomogeneous-layer model.	127

List of Figures

- Figure 2.1 Ray diagrams of correlation-type interferometry for creating virtual events propagating from the virtual source R to the receiver R' with (a) the nonstationary (S) and (b) stationary (S^*) source points. The raypaths denoted by the solid and dashed lines indicate the actual and reconstructed raypaths..... 13
- Figure 2.2 Ray diagrams of convolution-type interferometry for creating SSP reflection SxS' with (a) the nonstationary (R) and (b) stationary (R^*) receiver points. Solid lines denote events for creating SSP data and dashed lines indicate the specular reflections..... 15
- Figure 2.3 (a) Correlation-type interferometry generates the virtual primary reflection SxS' by correlating the direct wave $S'R$ with the primary reflection SxR ; (b) the corresponding correlation gather generated by the primary reflection and the direct wave. Events denoted by the dashed and solid lines indicate raypaths passing through the stationary (R^*) and nonstationary (R) receivers, respectively; the dashed ellipse denotes the stationary zone. 18
- Figure 2.4 Examples of transforms to create virtual events by using correlation-type interferometry: (a) VSP to SWP transform; (b) SSP to VSP transform; (c) VSP to crosswell profile transform. 20
- Figure 2.5 (a) Convolution of the direct wave $S'R$ with the primary reflection SxR can create virtual primary reflection SxS' ; (b) the corresponding convolution gather generated by the primary

reflection and the direct wave. Events denoted by the dashed and solid lines indicate raypaths passing through the stationary (R^*) and nonstationary (R) receivers, respectively; the dashed ellipse denote the stationary zone.	22
Figure 2.6 Applications of convolution-type interferometry: (a) generating SSP data from VSP data; (b) generating multiple from SSP primary reflections.	24
Figure 3.1 Determination of approximate stationary points by applying convolution-type interferometry: (a) the estimated stationary point is different from actual receiver point; (b) the estimated stationary point is the same as an actual receiver point.	27
Figure 3.2 Determining approximate stationary points by assuming a virtual layer on the top of a given model. The dashed and solid raypaths indicate the virtual and actual raypaths.	30
Figure 3.3 Ray diagram for estimating the velocity of the lower (target) layer by applying Snell's law. The events denoted by the dashed and solid lines in the lower layer indicate raypaths obtained with the correct and incorrect velocities of the lower layer, respectively. Here, i , r , x_0 and x denote angles of incidence and transmission and estimated reflection points for the correct and incorrect velocities, respectively.	33
Figure 3.4 A simple model with an additional virtual layer on the free surface.	35

Figure 3.5 Estimation of velocity for the dipping layer shown in Figure 3.4.	37
Figure 3.6 The number of reflection points with respect to traveltime difference for different assumed velocities.....	39
Figure 3.7 Reflection surface obtained by picking the deepest reflection points among the reflection points (the grey dots) calculated for all sources and receivers by using the velocity estimated from Figure 3.5.....	41
Figure 3.8 Flowchart for the main processing of one layer estimation by applying convolution.	44
Figure 3.9 (a) A stair-step layer model. (b) Traveltimes picked with high and low accuracies.....	46
Figure 3.10 Information of the virtual layer added on the stair-step layer model.	47
Figure 3.11 Velocity estimations with (a) high- and (b) low-accuracy traveltimes for the stair-step layer model shown in Figure 3.9a.	48
Figure 3.12 (a) Interface estimated by using low-accuracy traveltimes. (b) RTM image obtained from the velocity estimated by low-accuracy traveltime. The dashed green line denotes the actual interface.....	50
Figure 3.13 Simple models with slopes of (a) 0°, (b) 10°, (c) 20°, (d) 30°, (e) 40°, (f) 50°, (g) 60°, (h) 70°, (i) 80° and (j) 90°.....	53

Figure 3.14 Velocity estimations of the models with slopes of (a) 0°, (b) 10°, (c) 20°, (d) 30°, (e) 40°, (f) 50°, (g) 60°, (h) 70°, (i) 80° and (j) 90° in Figure 3.13. The dark blue cross symbols and the red plus symbols denote travelt ime difference and the number of reflection points, respectively.	56
Figure 3.15 (a) Variations of the total number of reflection points (including reflection points with large travelt ime differences) for slopes of 0° to 90°, and (b) a zoom-in version for slopes of 0° and 10°.	60
Figure 3.16 Reflection surface estimations for the models with slopes of (a) 0°, (b) 10°, (c) 20°, (d) 30°, (e) 40°, (f) 50°, (g) 60°, (h) 70°, (i) 80° and (j) 90° in Figure 3.13. The dashed dark blue lines indicate the real reflection surface; the black color represents the number of reflection points (counted in each 5 m × 5 m grid square): the darker color indicates that more reflection points are concentrated.	61
Figure 4.1 A homogeneous-layer model including a low-velocity layer. Actual sources and receivers are located on the real surface at distances from 100 m to 1,150 m with a regular interval of 2 m.	65
Figure 4.2 Estimation of (a) velocity and (b) interface for the first layer of the homogeneous-layer model.	67
Figure 4.3 Velocity and interface estimation for the second layer of the homogeneous-layer model: (a) velocity estimation by the second and third methods; (b) interface estimation by using the estimated velocity.	69

Figure 4.4 (a) P-wave velocity image obtained by the proposed method for the whole model shown in Figure 4.1; (b) depth profiles of the estimated velocities and the references (the dashed black lines) extracted at distances of 400 m (the red line) and 750 m (the green line). The dashed white lines indicate real interfaces.....	70
Figure 4.5 An inhomogeneous-layer model excluding the virtual layer: velocity increases gradually with depth in each layer. Actual sources and receivers are distributed on the real surface at distances from 100 m to 1,150 m with a regular interval of 2 m (at a depth of 0 m); virtual sources are located on the virtual surface at distances of -100 m to 1,350 m with a regular interval of 0.4 m (at a depth of -60 m).	73
Figure 4.6 (a) Velocity and (b) interface estimation of the first layer for the inhomogeneous-layer model.	74
Figure 4.7 (a) Velocity and (b) interface estimation for the second layer shown in Figure 4.5.	75
Figure 4.8 (a) P-wave velocity model obtained by using the proposed method for the whole inhomogeneous-layer model; (b) comparison of the estimated velocities and the references (the dashed black lines) extracted at distances of 380 m (the red line) and 830 m (the green line). The dashed white lines indicate real interfaces.....	76
Figure 4.9 A fault model with the same velocity on both sides of the fault plane.....	79

Figure 4.10 Observed CSGs (without the direct waves) (a) before and (b) after F-K filtering.	80
Figure 4.11 Estimation of (a, c, e) velocity and (b, d, f) interface for the first layer of the fault model shown in Figure 4.9 by using (a, b) left-side data, (c, d) right-side data and (e, f) both-sides data.	81
Figure 4.12 Estimation of (a, b, c) velocity and (d) interface for the second layer in Figure 4.9 by using (a) left-side data, (b) right-side data and (c, d) both of them.	83
Figure 4.13 (a, b) Background velocity models and (c, d) RTM images for the fault model shown in Figure 4.9: (a) velocity model obtained by the proposed method; (b) the linearly increasing model; (c) RTM image obtained from the velocity model generated by the proposed method (a); (d) RTM image obtained using the linearly increasing model (b). The dotted green lines denote the real interfaces.	84
Figure 4.14 (a) A fault model whose velocities are different on both sides of the fault plane and (b) a CSG generated from the fault model.	87
Figure 4.15 Estimation of (a, b) velocity and (c) interface for the first layer in Figure 4.14a by using (a) left-side data, (b) right-side data and (c) both of them.	88
Figure 4.16 Estimation of (a, b) velocity and (c, d) interface for the second layer in Figure 4.14a by using (a, c) left- and (b, d) right-side data.	89

Figure 4.17 Velocity estimation for the third layer in Figure 4.14a by using (a) left- and (b) right-side data; (c) total number of reflection points versus assumed velocity; (d) zoom-in version of (a).....	90
Figure 4.18 (a, b) Background velocity models and (c, d) RTM images for the fault model shown in Figure 4.14a: (a) velocity model obtained by the proposed method; (b) the linearly increasing model; (c) RTM image obtained from the velocity model obtained by the proposed method (a); (d) RTM image obtained from the linearly increasing model (b). The dotted green lines denote the real interfaces.	91
Figure 4.19 The real data acquired by using a streamer including 120 traces in each CSG: (a) picking traveltimes in the common offset gather; (b) picking traveltimes in the CSG. The dotted orange lines indicate picked traveltimes of reflections.	93
Figure 4.20 Velocity and interface estimations for the real data by using the first picked reflections shown in Figure 4.19: (a) estimating velocity of sea water; (b) estimating structure of the sea bottom.	96
Figure 4.21 Velocity and interface estimations for the real data by using the second picked reflections shown in Figure 4.19: (a) estimating the apparent velocity ranging from about sea surface to the top of the salt dome; (b) estimating the velocity of the top of the salt dome; (c) estimating structure for the top of the salt dome.	97
Figure 4.22 Background velocity model and RTM image for the real data shown in Figure 4.19: (a) background velocity model obtained by the	

proposed method; (b) the corresponding RTM image generated from the real data.	99
Figure 4.23 Velocity estimations with different maximum offsets for (a) the first and (b) second layers of the inhomogeneous-layer model shown in Figure 4.5; (c) interfaces recovered with the velocities estimated from the different maximum offsets for the second layer.	104
Figure 5.1 Three types of wave combinations used to estimate velocity of the lower layer: (a) M1 uses convolution of the virtual direct wave and primary reflection; (b) M2 uses cross-correlation of the direct wave with primary reflection; (c) M3 uses convolution of two primary reflections. R and θ indicate the stationary receiver point and incident angle, respectively; surfaces denoted by the dashed and double lines denote virtual surface and interfaces needed to be inferred, respectively; raypaths indicated by the solid and dashed lines are the actual and virtual raypaths generated by assuming virtual sources (S' in M1 and M2), respectively.	107
Figure 5.2 (a) Velocity and (b) interface estimation of the first layer for the homogeneous-layer model by applying M1.	110
Figure 5.3 (a) Velocity and (b) interface estimation of the second layer for the homogeneous-layer model by applying M1.	112
Figure 5.4 (a) Velocity and (b) interface estimation of the second layer for the homogeneous-layer model by applying M2.	113

Figure 5.5 (a, b) Velocity and (c) interface estimation of the second layer for the homogeneous-layer model by applying M3.....	114
Figure 5.6 P-wave velocity images obtained by (a) M1, (b) M2 and (c) M3 for the homogeneous-layer model. The dashed white lines indicate real interfaces.	117
Figure 5.7 Velocity-depth profiles of velocities estimated by different types of wave combinations and references extracted at distances of (a) 380 m and (b) 830 m of the homogeneous-layer model.....	119
Figure 5.8 Estimation of (a, c) velocity and (b, d) interface for the second layer of the inhomogeneous-layer model with (a, b) M2 and (c, d) M3.....	122
Figure 5.9 P-wave velocity models obtained by (a) M1, (b) M2 and (c) M3 for the inhomogeneous-layer model. The dashed white lines indicate real interfaces.	124
Figure 5.10 Velocity-depth profiles estimated by different types of wave combinations and references extracted at distances of (a) 380 m and (b) 830 m of the inhomogeneous-layer model.	126

1 Introduction

1.1 Seismic tomography methods

Since accurate descriptions of subsurface velocity structures have become essential to increasing the success rate in oil and gas exploration, many studies have been devoted to developing and improving seismic tomography (inversion) techniques in both the data (full waveform inversion and traveltimes tomography) and the image (prestack time and depth migration tomography, migration velocity analysis, etc.) domains (Pon and Lines, 2004; Trinks *et al.*, 2005; Shin and Min, 2006; Cameron, Fomel and Sethian, 2007; Brossier, Operto and Virieux, 2009; Taillandier *et al.*, 2009; Jones, 2010; Gholami *et al.*, 2013; Li and Fomel, 2015).

Data-domain seismic tomography techniques recover subsurface material properties by minimizing an objective function built from the residuals between observed data and data calculated for an assumed (initial or updated) model, and minimizing this objective function is a nonlinear problem. These techniques are generally performed by converting the nonlinear problem into a linear problem and by solving a large matrix equation. Because field data result from a combination of several unknowns, the inverse problem of recovering the unknowns from field data always suffers from non-uniqueness and uncertainty of solutions.

A good initial starting model can be used to avoid this issue. When an initial model deviates from the true velocity model, many iterations are needed; nevertheless, distorted results can be obtained. Therefore, to mitigate this issue and to improve the reliability of the result, conventional tomography methods started with a good initial model or introduced a supplementary method. Lambaré *et al.* (2007) presented an improved initial velocity model for waveform inversion proposed by using Beyond Dix to provide an accurate fast-track prestack depth migration image from prestack time migration image; Shin and Cha (2008) developed a Laplace domain waveform inversion that is not sensitive to initial velocity model because the proposed algorithm can generate a long-wavelength velocity model; Oh and Min (2013) presented a weighting method with whom the global minimum solution can be obtained regardless of the initial guesses; Wu, Luo and Wu (2014) developed envelope inversion for recovering low-wavenumber components (i.e., smooth background) to reduce initial model dependence; Hondori *et al.* (2015) applied well data to the full waveform inversion.

Data-domain seismic tomography also can provide an initial starting model to other inversion methods (Shin and Cha, 2009; Prioux *et al.*, 2013). Among the various data-domain seismic tomography methods, reflection traveltime tomography (RTT) has been popularly used in practice. RTT estimates subsurface velocity structures by minimizing observed and model-based reflection traveltimes (Jones, 2010). Model-based reflection traveltimes are obtained by using a ray tracing method for an initial or assumed model. As a result, we obtain smoothed subsurface velocity

structures, which have been successfully used as background models for seismic migration and initial guesses for subsequent full waveform inversion, rather than detailed structures.

However, RTT requires much computational effort, specifically for the processes of ray tracing and solving the tomographic matrix. As the cell size becomes fine (i.e., the number of unknowns increases), the required computer memory and computational time greatly increase. Many studies have been devoted to improving the computational efficiency of ray tracing. Moser (1991) calculated raypaths and traveltimes to all points simultaneously by using the shortest path calculation method. This method does not suffer from the limitations of classical ray methods on the complexity and dimension of the velocity model. Zhao, Zhang and Teng (2004) developed the minimum traveltime tree algorithm for seismic ray tracing by predefining the propagation area of secondary waves to reduce computational effort for the calculation of seismic rays and traveltimes. On the other hand, there have been studies to mitigate the non-uniqueness problem of ray-based RTT. Vesnaver (1996) reduced (or zeroed) the null space by shifting the cell boundaries, splitting a cell into two or more parts, or merging cells. Wéber (2001) proposed the method of finding optimal triangular cell parameterization by minimizing the null space of the tomographic matrix.

However, it is still not easy to efficiently and accurately recover velocity and reflector depth without *a priori* information and does not suffer

from the non-uniqueness problem.

1.2 Seismic interferometry

Seismic interferometry (SI) (virtual source method) is a method that newly generates seismic responses for virtual sources by correlating or convolving seismic data recorded at different receiver positions with no information between those receivers (Schuster, 2001; Bakulin and Calvert, 2004, 2006; Wapenaar and Fokkema, 2006). In other words, SI can achieve sources (or receivers) redatuming as if virtual sources (or receivers) were located at specific positions (i.e., actual source or receiver positions).

SI can be applied to both passive and active data. In the early 2000s, it used mainly for surface waves. The application for body waves is increasing in recent 10 years.

For passive data, cross-correlation has been commonly used. It has been applied to seismic coda data and background noise data with long time observations. Campillo and Paul (2003) produced a low-frequency coherent part in the diffuse field by correlating seismic coda data, and showed that direct waves between two perfectly located positions can be extracted from the produced diffuse waves; Shapiro *et al.* (2005) correlated 30 relatively quiescent days of ambient seismic noise data to construct tomographic images; Draganov, Wapenaar and Thorbecke (2006) reconstructed reflections by correlating data generated from randomly distributed subsurface white-noise sources; Gerstoft *et al.* (2006) correlated seismic noise data recorded at 151 stations to extract the group velocity of surface

waves; Draganov *et al.* (2007) correlated 10 hours of seismic background noise data to reconstruct reflections; Lin *et al.* (2007) generated Rayleigh wave group velocity dispersion by correlating one-year of ambient noise data observed at 42 stations; Draganov *et al.* (2009) retrieved common shot gathers (CSGs) including reflections by applying SI to the 11 hours of ambient seismic noise data from 3200 receiver channels; Xu *et al.* (2012) observed surface waves, reflections and refractions in the CSG retrieved from 25 hours ambient seismic noise data by applying correlation-type interferometry; Zhang, Juhlin and Sopher (2014) observed both surface waves and body waves by applying correlation to 3 daytimes of active data generated by a weight drop source and 71 hours of ambient noise data; Roux *et al.* (2016) obtained velocity maps from densely distributed 1108 vertical geophones.

For active data, SI is generally used to reconstruct signals for redatuming, interpolation and extrapolation to improve resolution of subsurface imaging. Schuster (2005) derived Fermat's interferometric form to obtain interferometric traveltimes (i.e., redatum sources and receivers from surface to deeper layer) and estimated interferometric tomogram by using those reconstructed traveltimes; Bakulin and Calvert (2006) demonstrated that it is possible to image structures, which are difficult to implement with conventional methods, by using virtual CSGs reconstructed by redatuming source from above a complex overburden to the borehole (under the overburden); Xiao and Schuster (2006) redatumed common depth data below salt without information of the salt body or overburden; Yu and

Schuster (2006) presented cross-correlation ghost migration (interferometric imaging) to provide an improved image; Dong and Hanafy (2008) performed interpolation and extrapolation for the sparse 2D ocean bottom seismic data by applying SI; Hanafy and Schuster (2014) performed interpolation for the sparse 2D and 3D marine data.

1.3 Objective and outline

We generally sum (stack) the correlation or convolution gathers generated from various pairs of signals to reconstruct the necessary signals (Schuster, 2009; Dragoset *et al.*, 2010; Wapenaar *et al.*, 2010). This means that those correlation or convolution gathers, which are used for reconstructing signals, contain the signals that pass through the stationary points or their adjacent zones. Thus, we can derive the stationary points approximately from those gathers. Once the stationary points are determined, the directions of incident rays are decided.

Therefore, based on those stationary points (i.e., angles of incidence), which are derived from the characteristics of interferometric gathers, I propose an efficient and robust ray-based RTT method that does not require *a priori* information and also does not suffer from the non-uniqueness problem.

In the following chapters, I first explain the basic theory of traveltime interferometry. Then after explaining how to determine stationary points and how to estimate velocity and interface, the proposed method is demonstrated for both synthetic and real field data.

2 Basic theory of travelttime interferometry

This chapter describes the basic theory of correlation- and convolution-type interferometry based on Fermat's principle (i.e., travelttime interferometry). There are various combinations of waves to reconstruct data with cross-correlation- or convolution-type interferometry. In this chapter, surface seismic profile (SSP) data and vertical seismic profile (VSP) data are used to describe the principles.

2.1 Principle of Fermat's interferometry

2.1.1 Correlation-type interferometry

As in Figure 2.1a, sources are located on the surface and receivers are distributed both on the surface and in the well. Assume that traveltimes of both SSP reflection $\tau_{SxR'}$ and VSP direct wave τ_{SR} are already known. Based on Fermat's principle, that is, wave travels along the least time raypath, the traveltime of SSP reflection propagating from S to R' is

$$\tau_{SxR'} \leq \tau_{SR} + \tau_{RxR'} . \quad (2.1)$$

Traveltime of SSP reflection $\tau_{SxR'}$ denotes the specular reflection time (i.e., traveltime when the ray passes through the stationary point) for a source at S and a receiver at R'.

If the receivers R and R' are fixed, equation (2.1) is satisfied with all sources placed on the free surface. Then rearranging equation (2.1), we can derive

$$\tau_{RxR'} \geq \tau_{SxR'} - \tau_{SR} . \quad (2.2)$$

From equation (2.2), we can know that the signal reconstructed by cross-correlation-type interferometry gives the largest traveltime among the traveltimes generated by the sources located on the surface.

Thus, when the source is located at the stationary source point (S^* in Figure 2.1b), traveltime of the VSP reflection satisfies

$$\tau_{RxR'} = \tau_{S^*xR'} - \tau_{S^*R} . \quad (2.3)$$

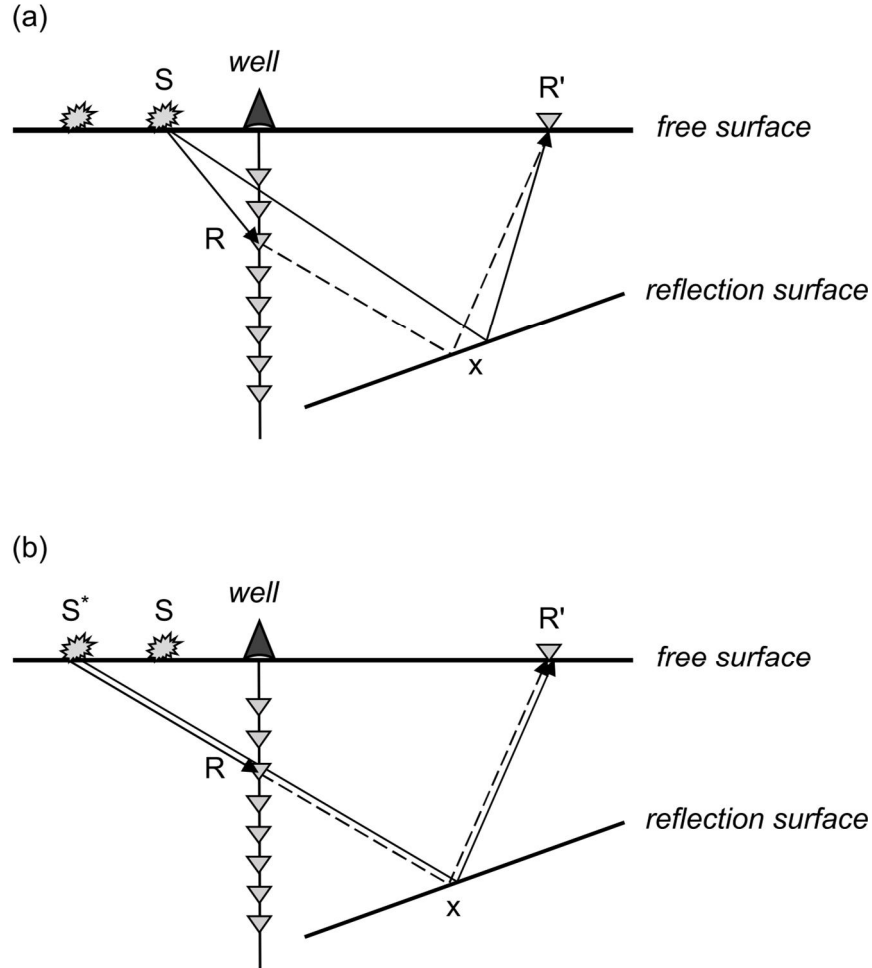


Figure 2.1 Ray diagrams of correlation-type interferometry for creating virtual events propagating from the virtual source R to the receiver R' with (a) the nonstationary (S) and (b) stationary (S^*) source points. The raypaths denoted by the solid and dashed lines indicate the actual and reconstructed raypaths.

2.1.2 Convolution-type interferometry

Convolution-type interferometry is similar to correlation-type SI. As in Figure 2.2a, VSP data are used to reconstruct SSP reflection data. Based on Fermat's principle, the traveltime of SSP reflection propagating from S to S' satisfies

$$\tau_{S \times S'} \leq \tau_{SR} + \tau_{S' \times R} . \quad (2.4)$$

When the receiver R is located at the stationary receiver point R^* (Figure 2.2b), the equation satisfies

$$\tau_{S \times S'} = \tau_{SR^*} + \tau_{S' \times R^*} . \quad (2.5)$$

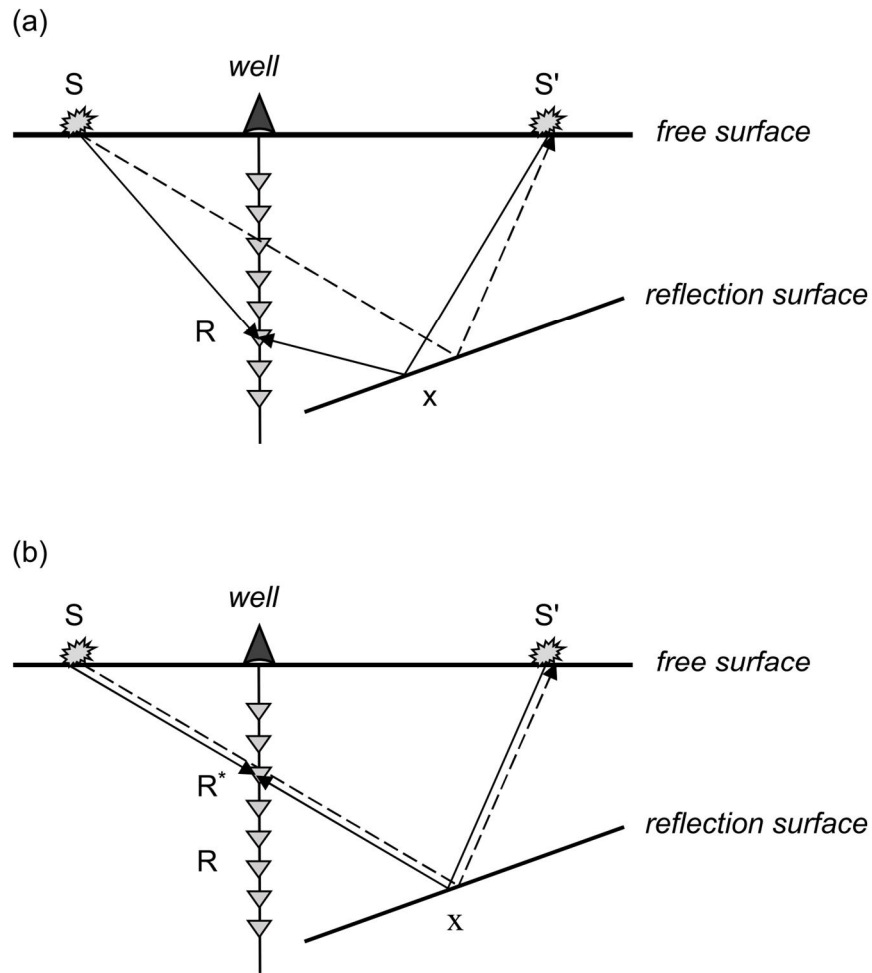


Figure 2.2 Ray diagrams of convolution-type interferometry for creating SSP reflection SxS' with (a) the nonstationary (R) and (b) stationary (R^*) receiver points. Solid lines denote events for creating SSP data and dashed lines indicate the specular reflections.

2.2 Characteristics of SI

2.2.1 Characteristic of correlation-type SI

Correlation of two seismic traces yields seismic event with phase decreased by their phase difference (Schuster, 2009). Figure 2.3a shows an example of reconstructing VSP data by correlation. In Figure 2.3a, correlating the primary reflection SxR with the direct wave $S'R$ yields the virtual primary reflection SxS' . When R is located at the stationary point R^* , the raypath $S'R$ coincides with a part of the raypath SxR . Figure 2.3b shows the correlation gather for reconstructing corresponding reflection event (e.g., SxS') for the designated source (S) and receiver (S') points.

As mentioned before, according to Fermat's principle, wave traveling through the stationary point or its adjacent zone will have the maximum traveltimes in the correlated gather (marked with the dashed ellipse in Figure 2.3b). The stationary point can appear as a zone rather than a point because of the sparse receiver array, source aperture limitation, finite frequency bandwidth, etc. In other words, when the ray passes through the stationary point, correlation cancels out the common raypath. Therefore, correlation-type SI can be used to reconstruct signals with shorter traveltimes and raypaths, such as generating single well profile (SWP) data from VSP data, generating VSP data from SSP data and generating crosswell profile data from VSP data (Figure 2.4).

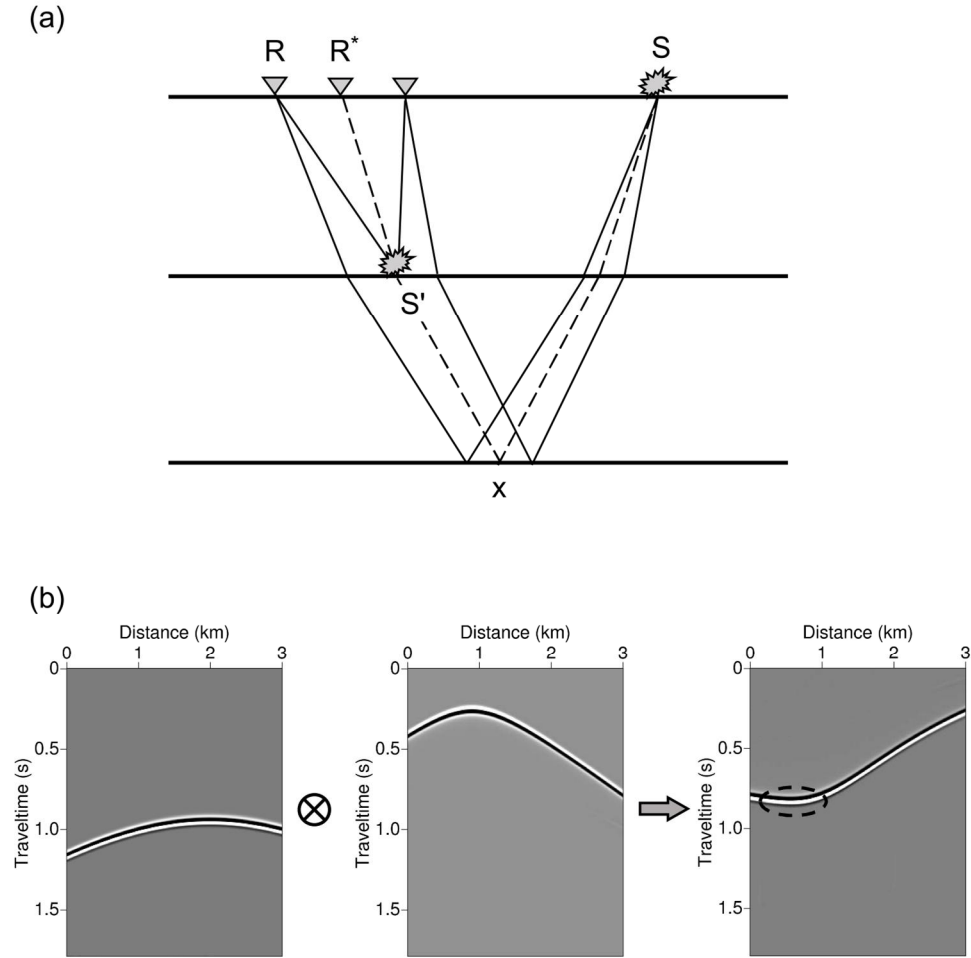


Figure 2.3 (a) Correlation-type interferometry generates the virtual primary reflection SxS' by correlating the direct wave $S'R$ with the primary reflection SxR ; (b) the corresponding correlation gather generated by the primary reflection and the direct wave. Events denoted by the dashed and solid lines indicate raypaths passing through the stationary (R^*) and nonstationary (R) receivers, respectively; the dashed ellipse denotes the stationary zone.

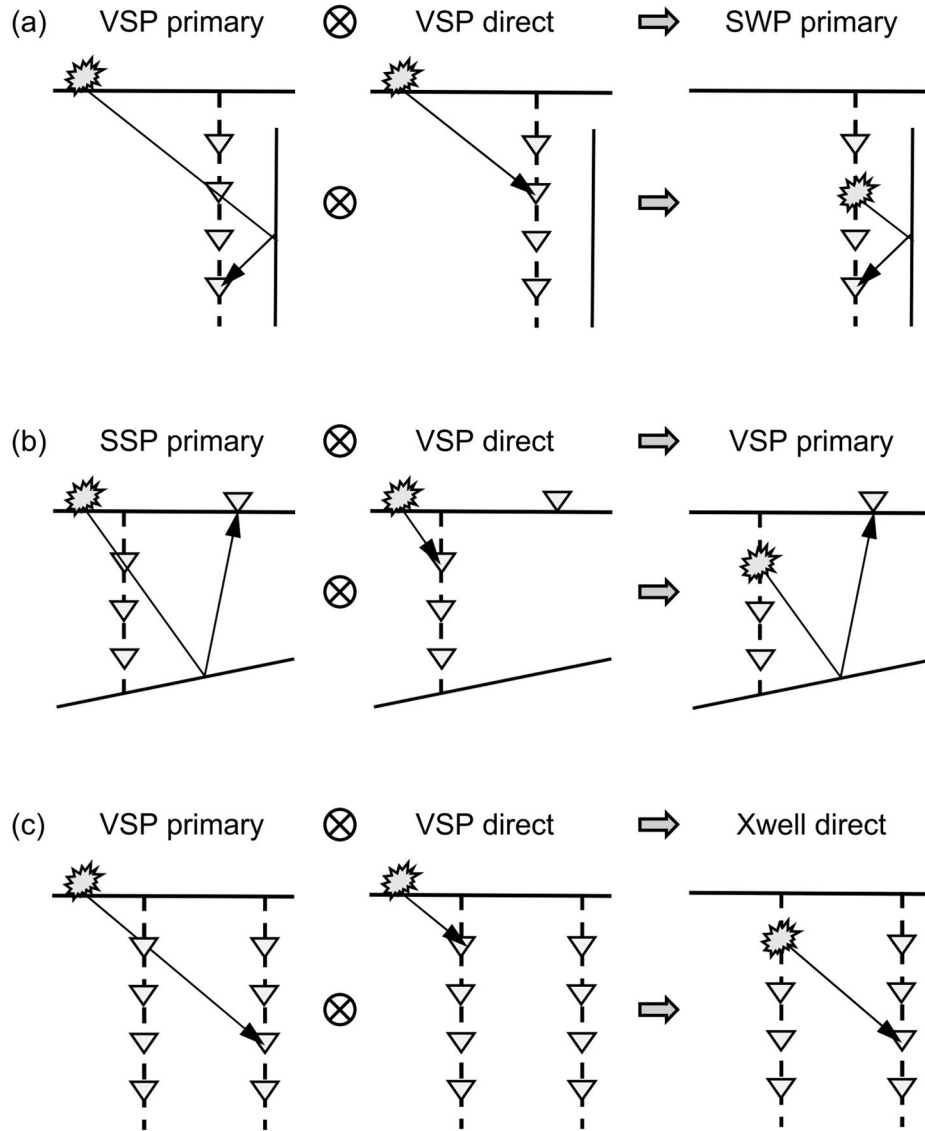


Figure 2.4 Examples of transforms to create virtual events by using correlation-type interferometry: (a) VSP to SWP transform; (b) SSP to VSP transform; (c) VSP to crosswell profile transform.

2.2.2 Characteristic of convolution-type SI

Similar to correlation, convolution of two traces gives event with phase elongated by their phase difference (Schuster, 2009). As shown in Figure 2.5a, by convolving the direct wave S'R with the primary reflection SxR, we can obtain virtual primary reflection SxS'.

Figure 2.5b shows the convolution gather, which is used to reconstruct reflection event (e.g., SxS'). Unlike the correlation gather, according to Fermat's principle, wave traveling through the stationary point or its adjacent zone will have the minimum traveltime in the convolved gather (marked with the dashed ellipse in Figure 2.5b).

Convolution-type SI joins raypaths to create a seismic event with longer traveltime and raypath. Thus, it can be utilized to reconstruct SSP data by convolving VSP direct wave with VSP reflection, predict multiple, etc. (Figure 2.6).

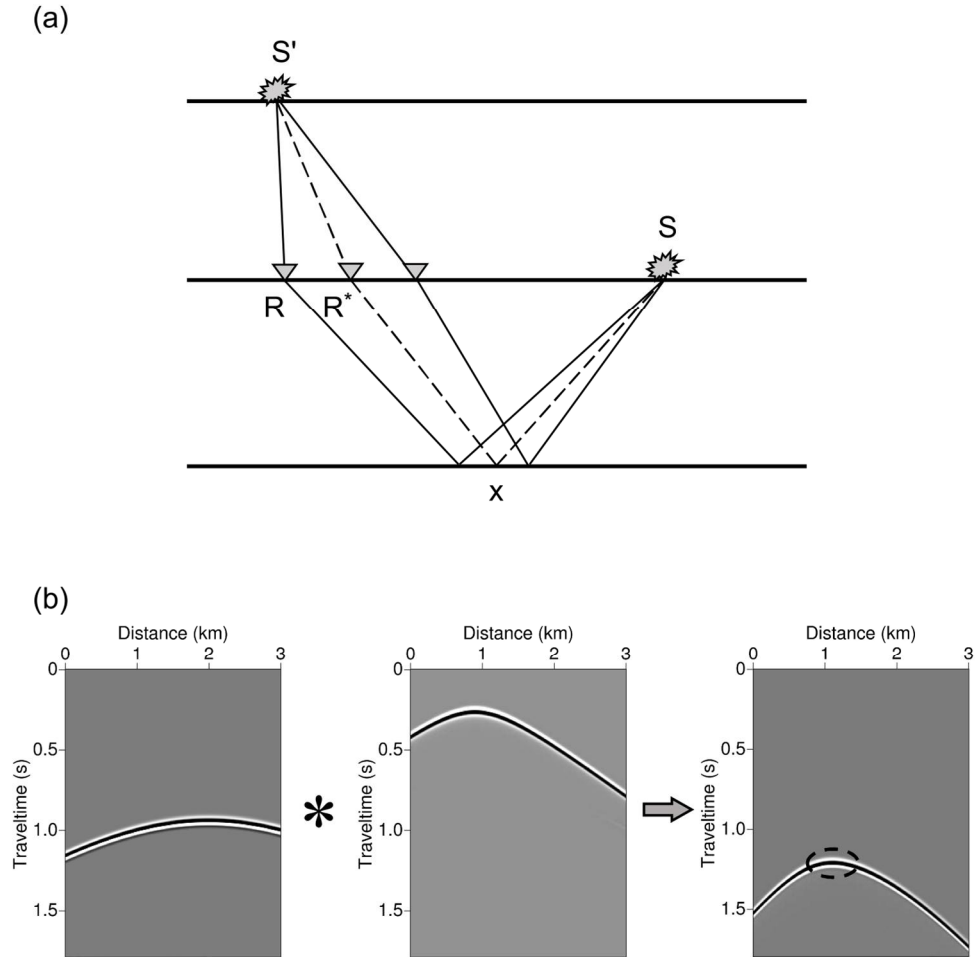


Figure 2.5 (a) Convolution of the direct wave $S'R$ with the primary reflection SxR can create virtual primary reflection SxS' ; (b) the corresponding convolution gather generated by the primary reflection and the direct wave. Events denoted by the dashed and solid lines indicate raypaths passing through the stationary (R^*) and nonstationary (R) receivers, respectively; the dashed ellipse denote the stationary zone.

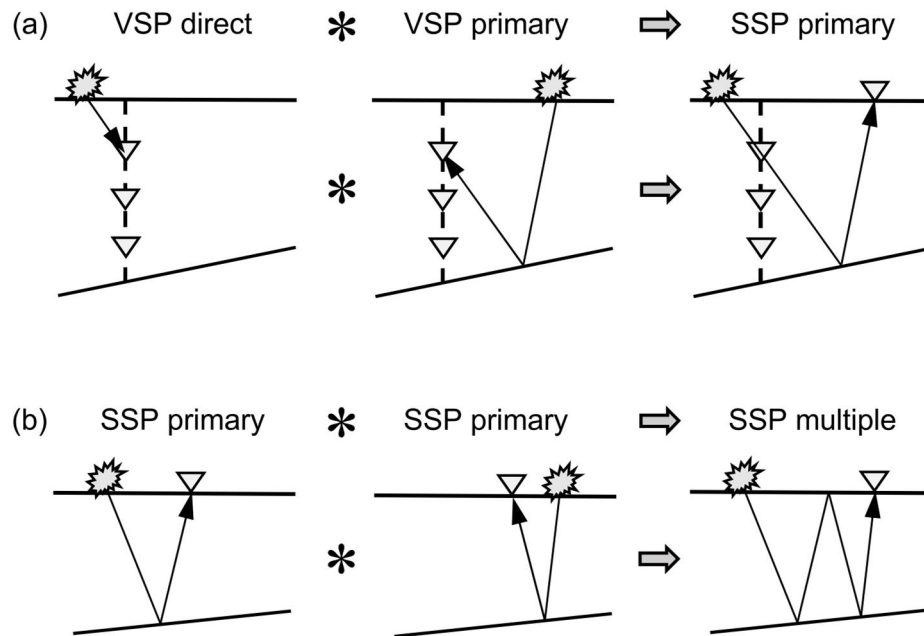


Figure 2.6 Applications of convolution-type interferometry: (a) generating SSP data from VSP data; (b) generating multiple from SSP primary reflections.

3 Estimation of P-wave velocity and interface

In this thesis, I assume that I only have SSP data and that the traveltimes of the primary reflections are picked with high accuracy from the real data.

3.1 Determination of approximate stationary point

Based on the characteristics of SI, if we know traveltimes of the waves used for creating correlation or convolution gather, we can approximately estimate stationary point by choosing the source or receiver that gives the maximum traveltime in the correlation gather or the minimum traveltime in the convolution gather.

Because the stationary point generally appears as a zone rather than a point, I roughly define the middle of the stationary zone as the stationary point (Figure 3.1). If the selected point is the same as an actual receiver point, the raypath S'R can be regarded as the incident raypath (Figure 3.1b). Once the stationary point is estimated in the correlation or convolution gather, the angle of incidence is accordingly determined. Although the estimated stationary point may not be completely correct, if the change of the incident angle is sufficiently small (i.e., if the ratio of thickness of the layer to the receiver interval is large enough and the sources (S') are distributed densely), it will have little effects on the accuracy of calculating the raypath.

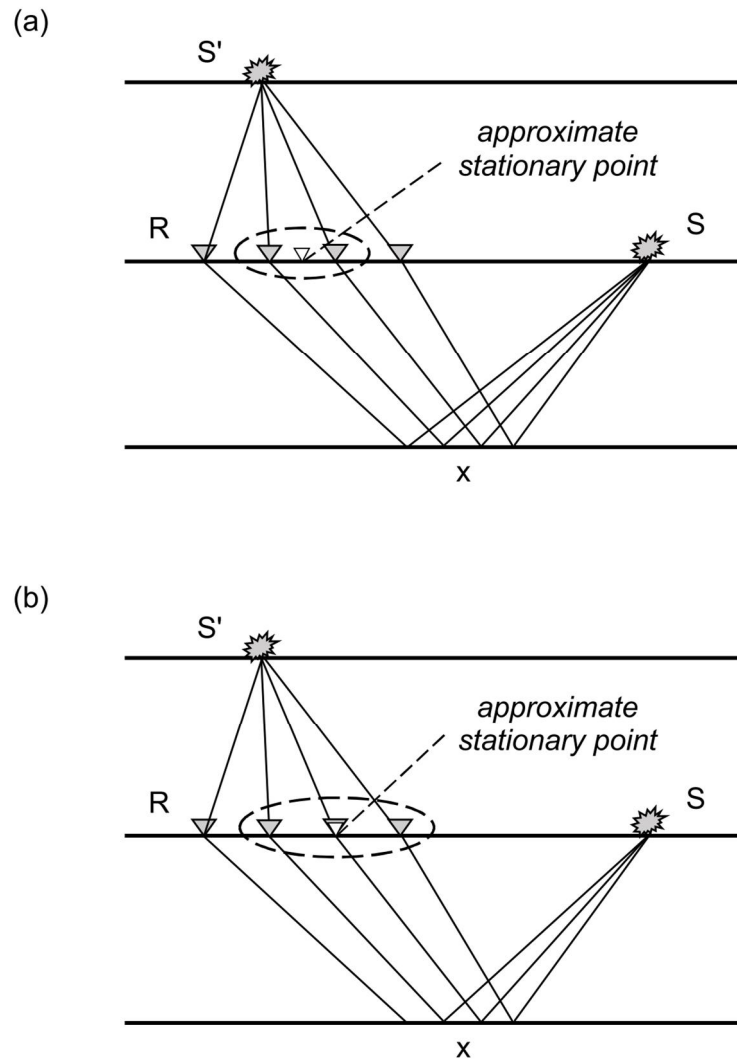


Figure 3.1 Determination of approximate stationary points by applying convolution-type interferometry: (a) the estimated stationary point is different from actual receiver point; (b) the estimated stationary point is the same as an actual receiver point.

3.2 Determination of approximate stationary points without *a priori* information

When the ray passes the stationary point, the correlation of two traces forms a response with a shorter raypath by cancelling out the common raypath (Schuster, 2009; Wapenaar *et al.*, 2010). This process requires the material properties of layers through which the common raypath passes if we only have SSP data.

In contrast, convolution forms a response with a longer traveltime. That is, convolution elongates raypaths by connecting raypaths (Schuster, 2009). For the uppermost layer, if we add a virtual layer (whose properties are already known) above the real surface (Figure 3.2), we can generate virtual responses by convolving the direct raypaths in the virtual layer and the reflection raypaths in the uppermost layer of the real media. Because reflection traveltimes are picked from real data, we only need to determine direct arrivals in the virtual layer. Accordingly, we do not require information on subsurface material properties.

In Figure 2.3a, because the top layer is a part of real subsurface media, we require *a priori* information of the shallow part for obtain traveltime of the direct waves (S'R), whereas as shown in Figure 3.2, the first layer corresponds to the virtual layer, therefore we already know its velocity and structure. In other words, the correlation-type SI can be applied to the cases that we can obtain information of the top layer beforehand, whereas the

convolution-type SI can be carried out without *a priori* information. Accordingly, for the imaging technique, I use the convolution-type SI shown in Figure 3.2 that convolves the virtual direct wave and actual primary reflection for the first layer estimation.

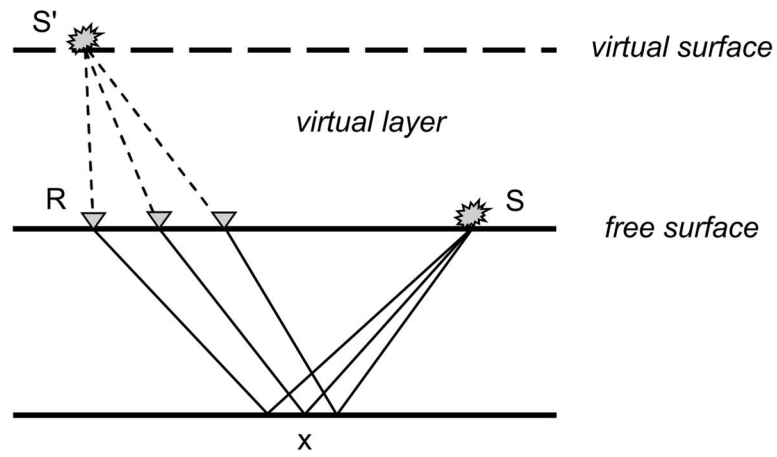


Figure 3.2 Determining approximate stationary points by assuming a virtual layer on the top of a given model. The dashed and solid raypaths indicate the virtual and actual raypaths.

3.3 Estimation of P-wave velocity

After the incident angle is determined in the upper layer (i.e., virtual layer) in Figure 3.2, we need to determine the raypath in the lower layer (which corresponds to the first layer of the original model without the virtual layer).

3.3.1 Estimation of reflection point for target layer

Now we know the velocity and incident angles in the upper medium, I estimate the velocity, raypaths and reflection surface in the lower medium (also called the ‘target’ layer). This estimation is a nonlinear problem. To efficiently solve this problem, a range of velocities are assumed for the lower layer. Then we can calculate the transmitted angles in the lower medium based on Snell’s law

$$\frac{v_2}{v_1} = \frac{\sin r}{\sin i}, \quad (3.1)$$

where v_1 , v_2 , i and r denote velocity of the upper and lower media, angles of incidence and transmission, respectively.

According to the reciprocity, we can also calculate the transmitted angle for the source point. The intersection of the two raypaths that propagate from the source and receiver points represents the reflection point (e.g., ‘x’ in Figure 3.3), from which we can calculate the traveltime of the reflection SxR from the designated source S to receiver R, as shown in Figure 3.3.

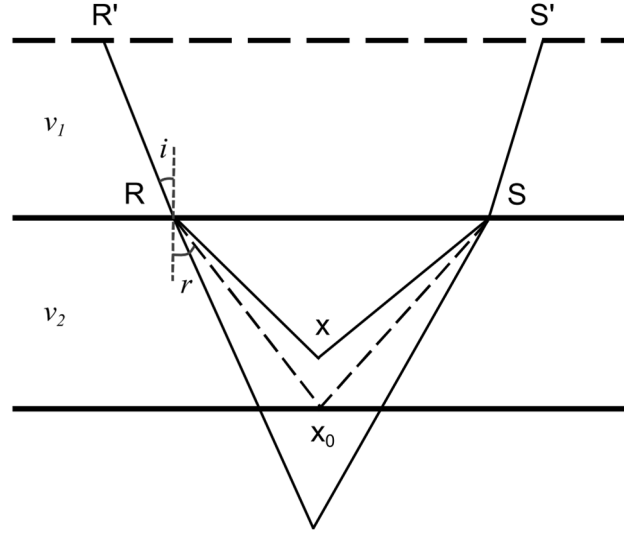


Figure 3.3 Ray diagram for estimating the velocity of the lower (target) layer by applying Snell's law. The events denoted by the dashed and solid lines in the lower layer indicate raypaths obtained with the correct and incorrect velocities of the lower layer, respectively. Here, i , r , x_0 and x denote angles of incidence and transmission and estimated reflection points for the correct and incorrect velocities, respectively.

3.3.2 Estimation of P-wave velocity

After estimating the reflection points for all assumed velocities, I determine the velocity of the lower layer; if that velocity is close to the true value, the difference between the observed and calculated traveltimes approaches zero. This principle can be applied by three methods.

A simple layered model shown in Figure 3.4, is used to explain the velocity and interface estimation. Note that the virtual layer (whose surface is denoted by the dashed line) is added on the top of the given model in Figure 3.4. Virtual sources are distributed on the virtual surface at distances ranging from 0 m to 1,000 m with a regular interval of 0.2 m; 100 actual sources and 167 receivers are distributed on the real surface at distances ranging from 100 m to 600 m with regular and irregular intervals, respectively.

The reflection points in the target media are already estimated and the traveltime differences are also calculated for all possible source-receiver pairs by assuming a range of velocities (from 1 km/s to 4 km/s with an interval of 0.002 km/s) for the target layer.

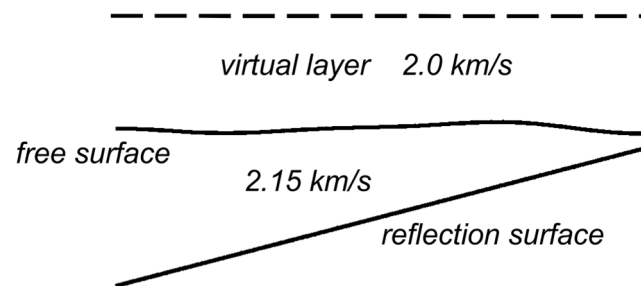


Figure 3.4 A simple model with an additional virtual layer on the free surface.

3.3.2.1 The first method: Considering average of traveltime differences

The first velocity estimation method is to simply choose the velocity that minimizes the average (absolute value) of the traveltime differences, such as root-mean-square (RMS).

If the stationary points and velocity are estimated with high accuracy, the estimated reflection points will be placed around the real reflection point (x_0 in Figure 3.3). Accordingly, traveltime difference will approach zero. Therefore, we can choose a velocity that gives zero traveltime difference.

Figure 3.5 shows the RMS value of the traveltime differences for the model shown in Figure 3.4. From Figure 3.5, we can easily choose the velocity that gives the minimum traveltime difference. Comparing the estimated velocity (2.082 km/s) with the true value (2.15 km/s), we note that the proposed method can estimate the velocity with a high accuracy (3% error), although the determined stationary points may not be correctly positioned.

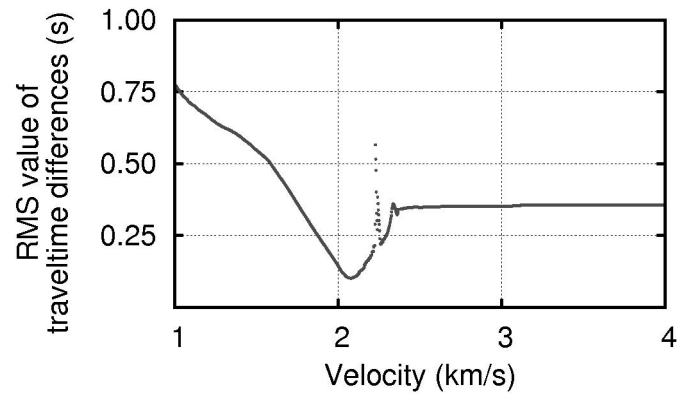


Figure 3.5 Estimation of velocity for the dipping layer shown in Figure 3.4.

3.3.2.2 The second and third methods: Considering traveltime difference and number of reflection points

The second and third methods are based on the phenomenon that the maximum numbers of reflection points for different velocities appear at different traveltime differences, as shown in Figure 3.6. Because the true velocity of the lower medium shown in Figure 3.4 is 2.15 km/s, the velocity of 1.98 km/s has the peak number of reflection points with approximately zero traveltime difference. In contrast, as the velocity deviates from the true value, the peak in the number of reflections moves away from zero traveltime difference. In addition, Figure 3.6 shows that a velocity close to the true value yields more reflection points at a traveltime difference equal to zero. From these observations, I define the second and third methods.

The second method is to plot the traveltime difference with the maximum number of reflection points versus velocity and then choose the velocity that gives a traveltime difference equal to zero as the velocity of the target layer. The third method is to count the number of reflection points at zero traveltime difference and then choose the velocity that gives the most reflection points. To reduce the uncertainty, we can determine velocity by considering both of them. The applications of the second and third methods are shown in the section 3.6 and the next chapters.

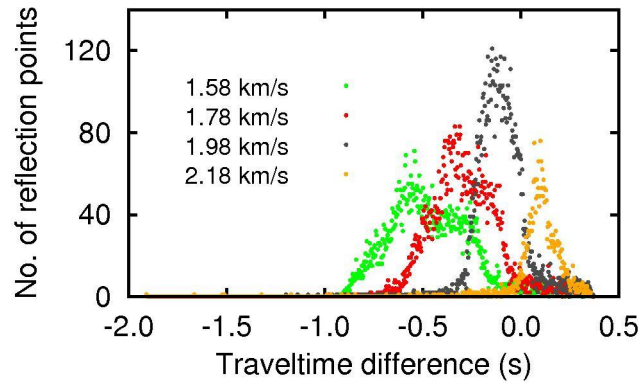


Figure 3.6 The number of reflection points with respect to traveltime difference for different assumed velocities.

3.4 Estimation of interface

Once the velocity is estimated, we can use the estimated velocity to recover the bottom boundary of the target layer. If traveltime picking and estimation of stationary points are performed with high accuracy, the reflection points, which are generated by combining the estimated velocity and the incident angles, will be placed on the real reflection surface. Therefore, the bottom boundary of the target layer can be recovered by those reflection points. (The application is shown in the next chapter.) Sometimes, the reflection points positioned by using the estimated stationary points are not sufficient to accurately resolve the whole interface because reflectors are only determined for designated sources and receivers and the determined stationary points may not be completely correct. Thus, to improve reliability of recovering the reflection surface, I plot all possible reflection points (the grey dots in Figure 3.7) for all sources and receivers by using the estimated velocity. Then, we can recover the bottom boundary of the target layer by picking the deepest reflection points (represented by the red line in Figure 3.7) (Russell, 1998). Comparing the estimated interface with the real interface (the dashed dark blue line in Figure 3.7), we see that the proposed method successfully resolves the reflection surface.

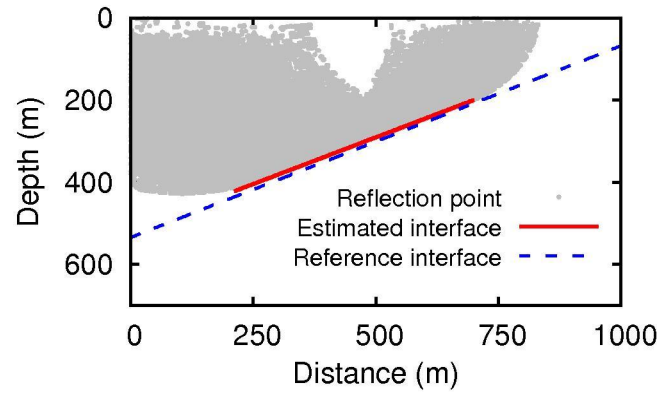


Figure 3.7 Reflection surface obtained by picking the deepest reflection points among the reflection points (the grey dots) calculated for all sources and receivers by using the velocity estimated from Figure 3.5.

3.5 The main procedures of estimation method

Once the first layer is resolved, lower layers can be recovered by recursively applying the same method downward. Figure 3.8 shows main processing of the proposed method for one layer. The procedures of the proposed method with convolution-type interferometry are summarized for the first layer as follows:

1. Pick the actual primary reflections.
2. Assume a virtual layer above the real surface, and calculate the traveltimes between the virtual sources and actual sources/receivers by using simple arithmetic calculation.
3. Choose a virtual source and an actual source, and generate a convolution gather by using the virtual and actual CSGs of the selected sources.
4. Select the middle point of the stationary zone as the approximate stationary point. When the selected point coincides with an actual receiver point, this point is used to calculate the incident angle.
5. Repeat steps 3 and 4 for all virtual sources and actual sources.
6. Repeat steps 3 to 5 for all actual receivers instead of actual sources.
7. Assume a range of velocities for the first layer (i.e., target layer), and use the incident angles estimated in the previous steps to calculate the transmitted angles by applying Snell's law.
8. Plot the reflection points (i.e., the points of intersections) by using two raypaths that start from each actual source-receiver pair, and calculate the traveltimes for all assumed velocities.

9. Estimate the velocity for the first layer 1) by plotting the RMS value of the traveltime differences versus velocity, 2) by plotting the traveltime differences with the most reflection points versus velocity or 3) by counting the number of reflection points with zero traveltime difference for each velocity.
10. Estimate the reflector for the first layer by using the estimated velocity.
11. Repeat steps 3 to 10 to resolve the lower layers.

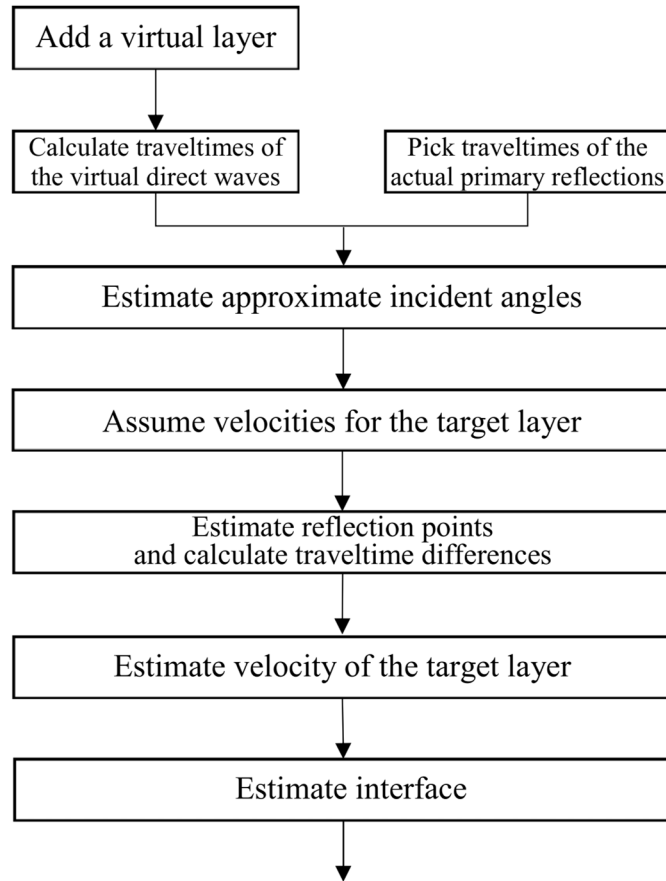


Figure 3.8 Flowchart for the main processing of one layer estimation by applying convolution.

3.6 Sensitivity analysis

3.6.1 Sensitivity to the accuracy of traveltime picking

Because the velocities of layers are estimated by comparing observed and calculated traveltimes, the accuracy of the proposed method may depend on the accuracy of picking primary reflections. For the stair-step layer model shown in Figure 3.9a, I investigate the dependence of the proposed method on the accuracy of picking primary reflections.

Figure 3.9b shows primary reflection traveltimes picked from CSGs with high and low accuracies. In this analysis, a virtual layer (Figure 3.10) is added on the given model to determine stationary points for velocity estimation. Figures 3.11a and 3.11b show velocity estimations for the traveltimes with high and low accuracies, respectively. Traveltime difference with the maximum number of reflection points (the second velocity estimation method) and the number of reflection points with zero traveltime difference (the third velocity estimation method) are used for the velocity estimation. In Figure 3.11, we can choose the velocities that give zero traveltime difference (the second velocity estimation method) with the most reflection points (the third velocity estimation method). From Figures 3.11a and 3.11b, the velocities are estimated to be 2.3 km/s and 2.32 km/s, respectively, which are very close to the true value of 2.35 km/s.

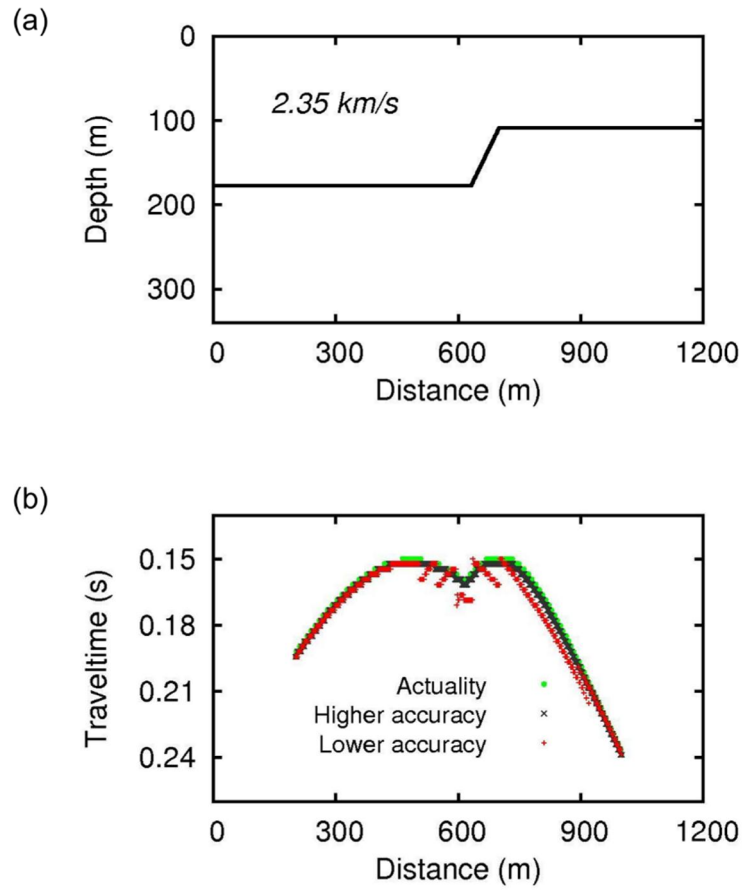


Figure 3.9 (a) A stair-step layer model. (b) Traveltimes picked with high and low accuracies.

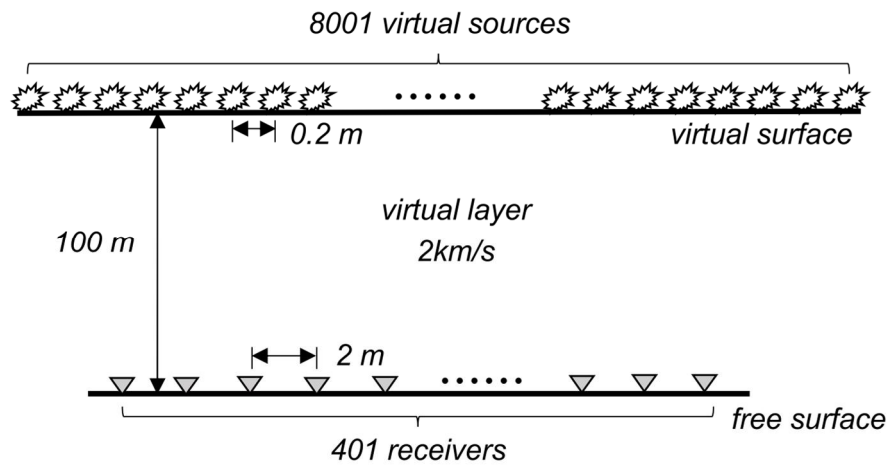


Figure 3.10 Information of the virtual layer added on the stair-step layer model.

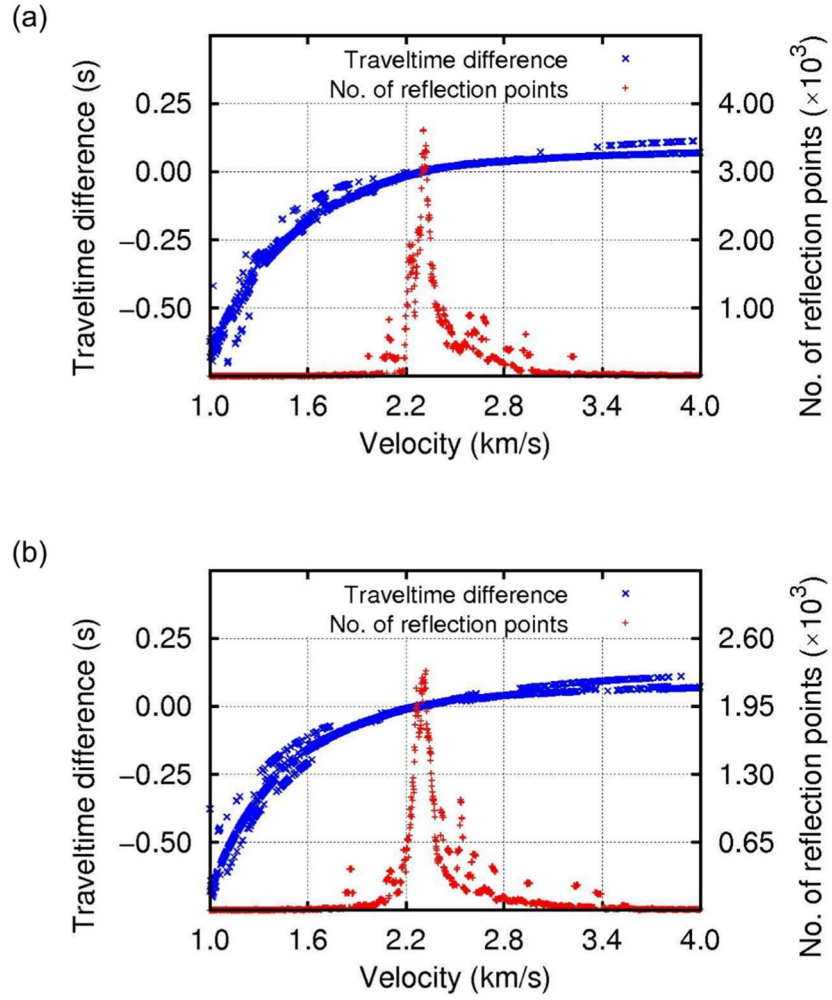


Figure 3.11 Velocity estimations with (a) high- and (b) low-accuracy traveltimes for the stair-step layer model shown in Figure 3.9a.

From these results, I can say that the proposed velocity estimation method is not sensitive to the accuracy of picking primary reflections. This finding is because the proposed velocity estimation method is related to the selection of receivers with the shortest propagation time instead of the traveltimes of each trace in the gather. In addition, by using a large amount of data, we can mitigate the effect of the low-accuracy data.

Figure 3.12a shows the interface estimated by using the low-accuracy traveltimes. The estimated interface slightly deviates from the actual interface, and this deviation indicates that the interface estimation is sensitive to the accuracy of traveltimes picking to some extent. Figure 3.12b shows a reverse time migration (RTM) image, where the interface is well recovered, obtained from the velocity estimated by the proposed method. As a result, I suggest additionally applying prestack depth migration for interface estimation when it is not easy to accurately pick primary reflection traveltimes.

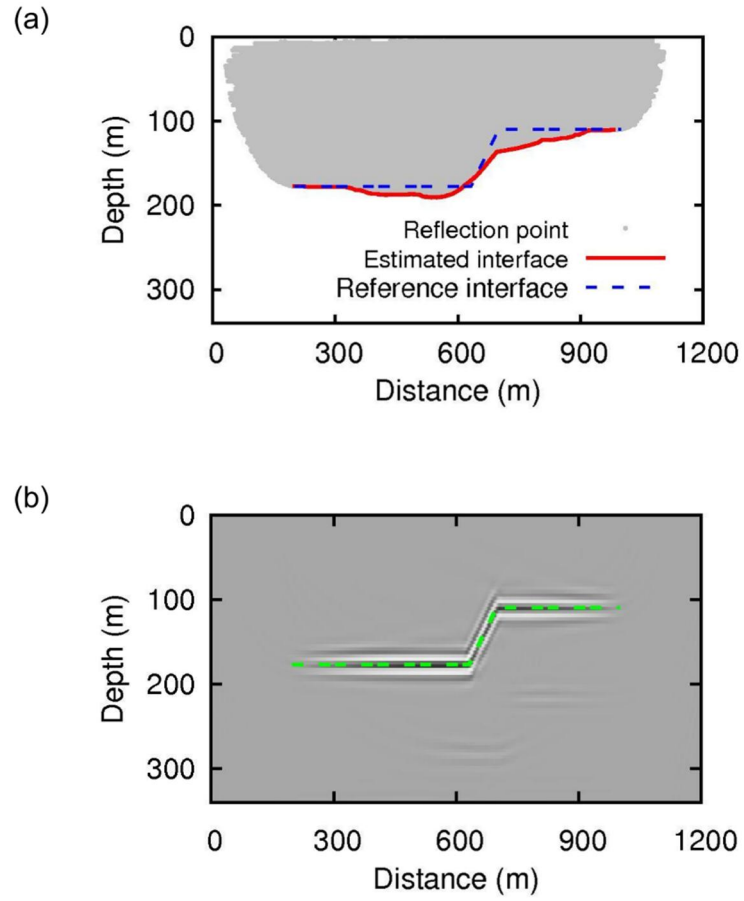


Figure 3.12 (a) Interface estimated by using low-accuracy traveltimes. (b) RTM image obtained from the velocity estimated by low-accuracy traveltimes. The dashed green line denotes the actual interface.

3.6.2 Accuracy analysis on the slope of reflection surface

To demonstrate the accuracy of estimated velocity and interface for different slopes of reflection surfaces, the proposed method is applied to the simple models with various slopes from 0° to 90° , as shown in Figure 3.13. Table 3.1 shows information on the virtual layer and geometry used in this analysis.

As mentioned before, the velocity is first estimated and then the interface is inferred by the estimated velocity. In this analysis, we use the second and third velocity estimation methods to determine the velocity of the target layer. Figure 3.14 shows the traveltime difference that gives maximum number of reflection points (the second method) and the number of reflection points with zero traveltime difference (the third method), which were obtained by changing the velocity for the target layer at an interval of 0.02 km/s. In Figure 3.14, velocities are estimated to be 3.0 km/s for slopes from 0° to 30° , 2.98 km/s for 40° to 80° and 2.96 km/s for 90° by choosing the velocities that give zero traveltime difference with the most reflection points. From Figure 3.14, we can see that for gentle slopes, reflection points with zero traveltime difference are sufficiently generated and the traveltime differences with reflection points concentrated show a similar tendency. In contrast, when the slope is steep, for instance 80° , the number of reflection points significantly decreases. Moreover, unlike the cases with relatively small slopes, the traveltime differences do not show a certain tendency, although it also gives minimum difference (absolute value) near the true

velocity.

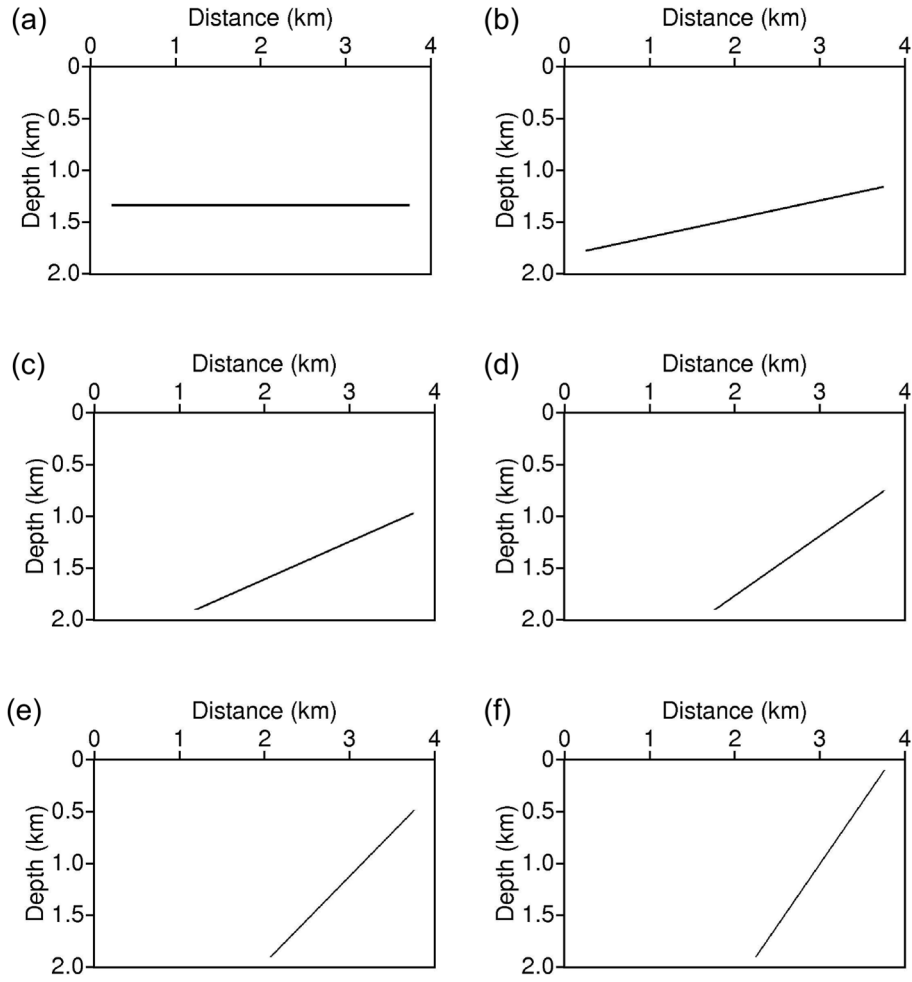


Figure 3.13 Simple models with slopes of (a) 0°, (b) 10°, (c) 20°, (d) 30°, (e) 40°, (f) 50°, (g) 60°, (h) 70°, (i) 80° and (j) 90°.

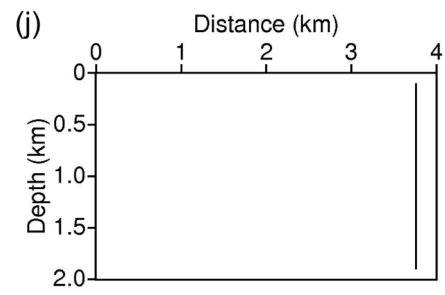
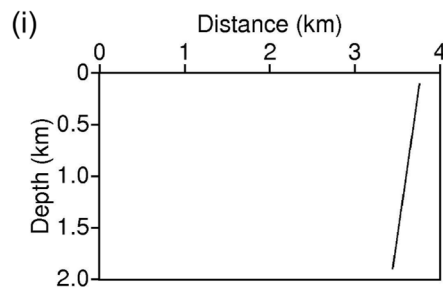
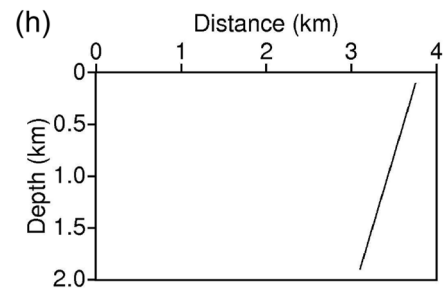
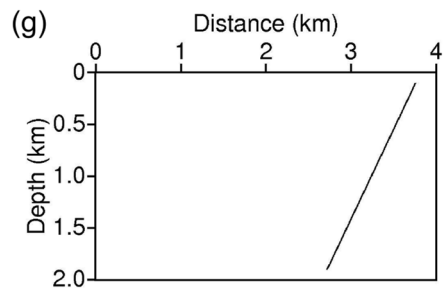


Figure 3.13 (Continued)

Table 3.1 Geometry of source and receiver used in Figure 3.13.

	Virtual layer (2.0 km/s)	Actual layer (background 3.0 km/s)	
	Virtual source	Actual source	Receiver
Total No.	3,601	601	601
Interval	0.0025 km	0.005 km	0.005 km
First location (horizontal direction)	-3.5 km	0.5 km	0.5 km
Last location (horizontal direction)	5.5 km	3.5 km	3.5 km
Depth (vertical direction)	-1.3 km	0 km	0 km

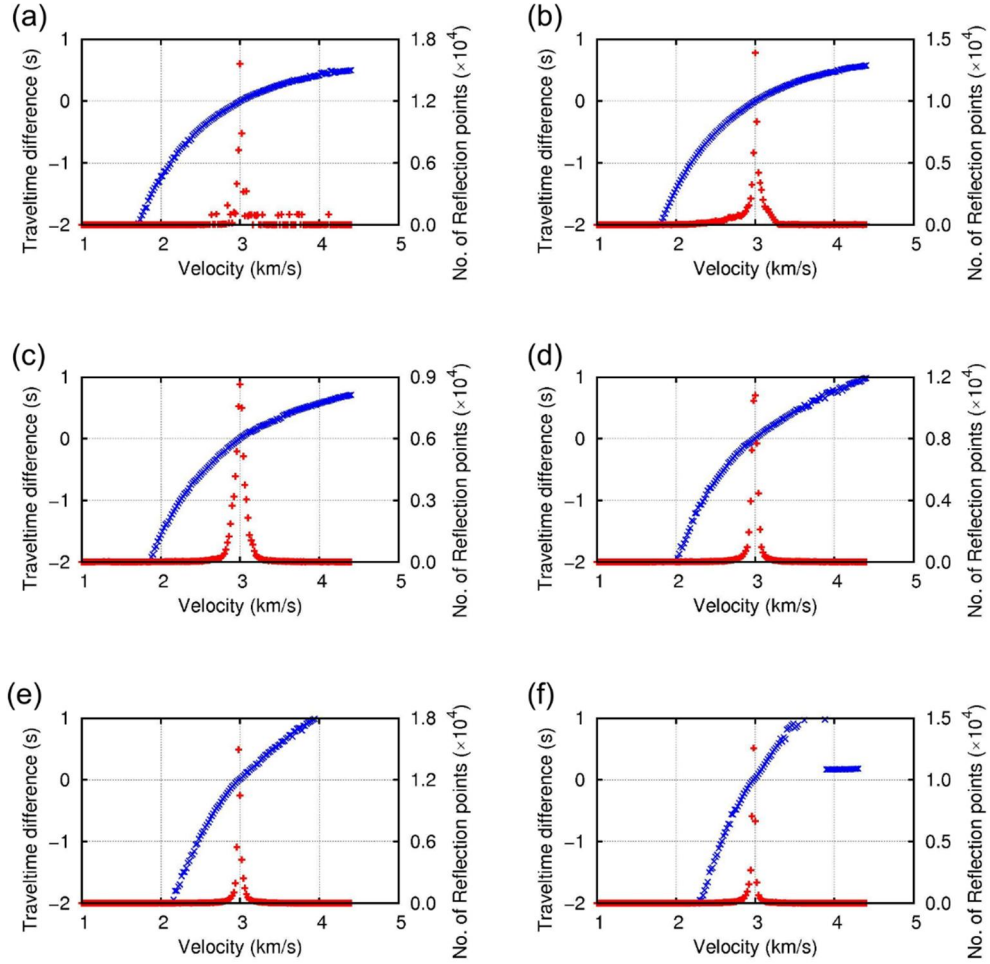


Figure 3.14 Velocity estimations of the models with slopes of (a) 0° , (b) 10° , (c) 20° , (d) 30° , (e) 40° , (f) 50° , (g) 60° , (h) 70° , (i) 80° and (j) 90° in Figure 3.13. The dark blue cross symbols and the red plus symbols denote traveltime difference and the number of reflection points, respectively.

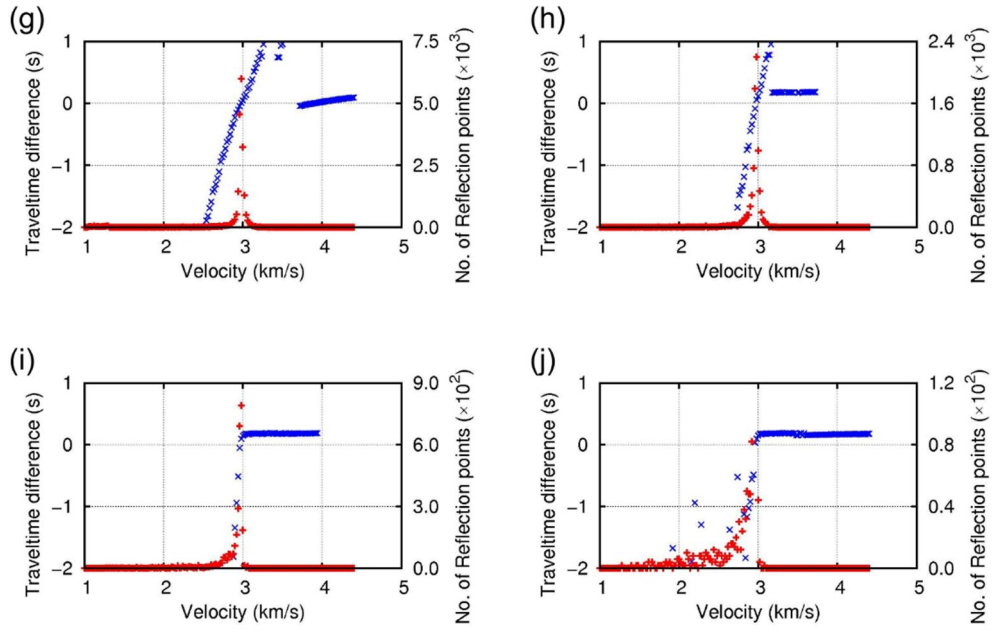


Figure 3.14 (Continued)

Figure 3.15 shows the variations of the total number of reflection points (shown as percentage), which include reflection points with large traveltime differences. Comparing the curves obtained from different slopes, it is obvious that when the velocity is larger than the true value, the total number of reflection points decreases faster as the slope increases. Therefore, we can roughly estimate the slope from the variation of the total number of reflection points. In addition, for steep slopes, as the assumed velocity exceeds the true value, the total number of reflectors decreases rapidly. The decreasing rate becomes larger for steeper slopes. For gentle slopes, the total numbers of reflection points decrease, but the greatest curvature occurs at higher velocity than the true value. These observations can be used to determine the range of velocity for the target layer. In other words, the velocity where the total number of reflection points begins to decrease rapidly can be used to determine the upper limit of velocity for the target layer. The main reason why the total number of reflection points decreases more rapidly as the velocity becomes higher can be that the amount of energy refracted along the interface becomes larger as the velocity becomes higher.

Figure 3.16 shows the estimated reflection surface. Considering steep slopes, the reflection surfaces are estimated by counting the number of reflection points instead of plotting all reflection points: the position where the reflection points are concentrated is likely to be the real reflector. From Figure 3.16, it is observed that the proposed method can also estimate the reflection surfaces with large slopes well. For the cases with slopes of 80°

and 90° , it is difficult to estimate the deeper part of the reflection surface.

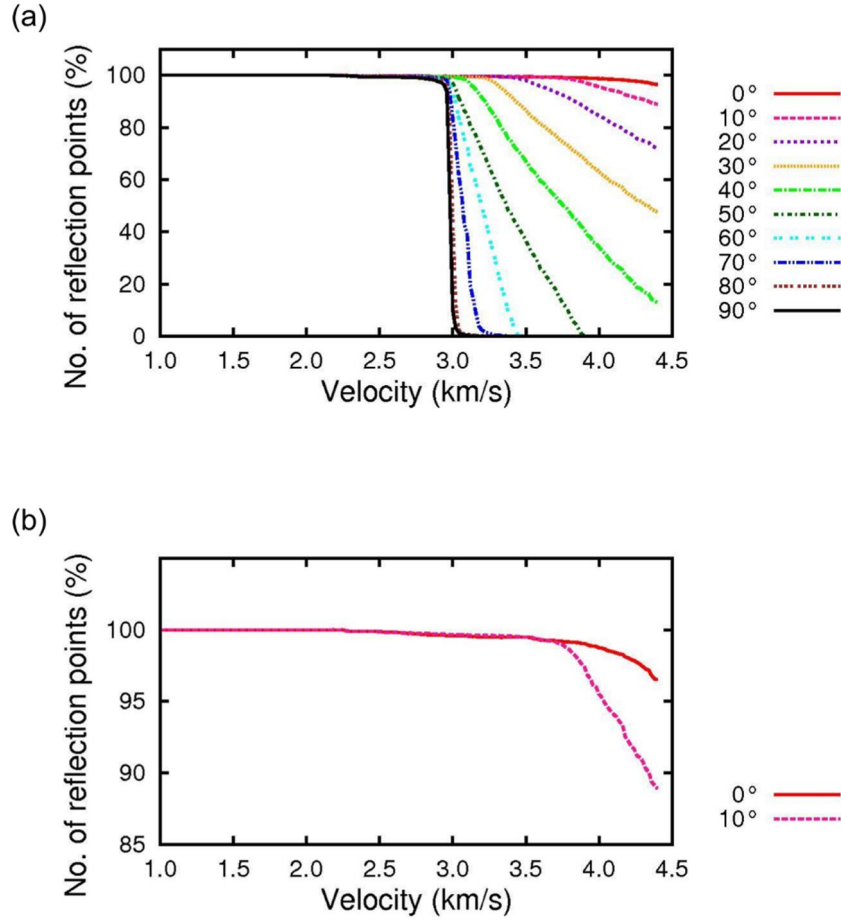


Figure 3.15 (a) Variations of the total number of reflection points (including reflection points with large traveltime differences) for slopes of 0° to 90°, and (b) a zoom-in version for slopes of 0° and 10°.

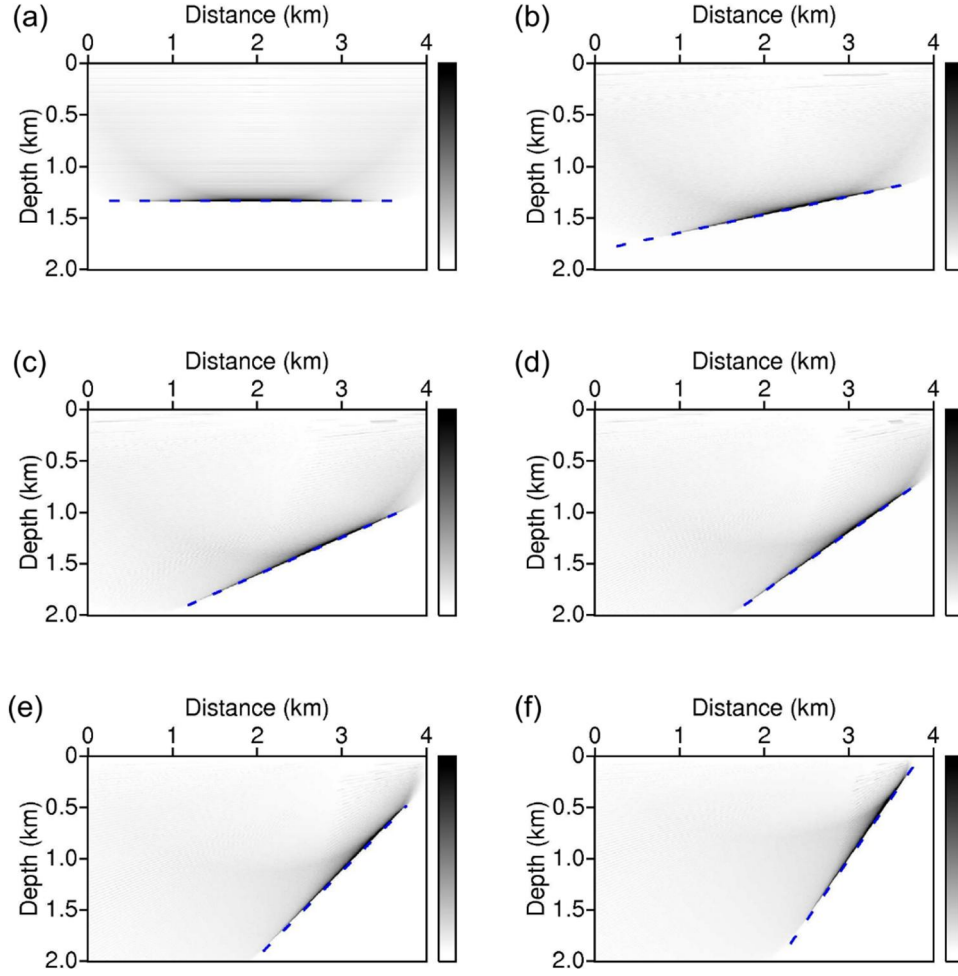


Figure 3.16 Reflection surface estimations for the models with slopes of (a) 0°, (b) 10°, (c) 20°, (d) 30°, (e) 40°, (f) 50°, (g) 60°, (h) 70°, (i) 80° and (j) 90° in Figure 3.13. The dashed dark blue lines indicate the real reflection surface; the black color represents the number of reflection points (counted in each $5 \text{ m} \times 5 \text{ m}$ grid square): the darker color indicates that more reflection points are concentrated.

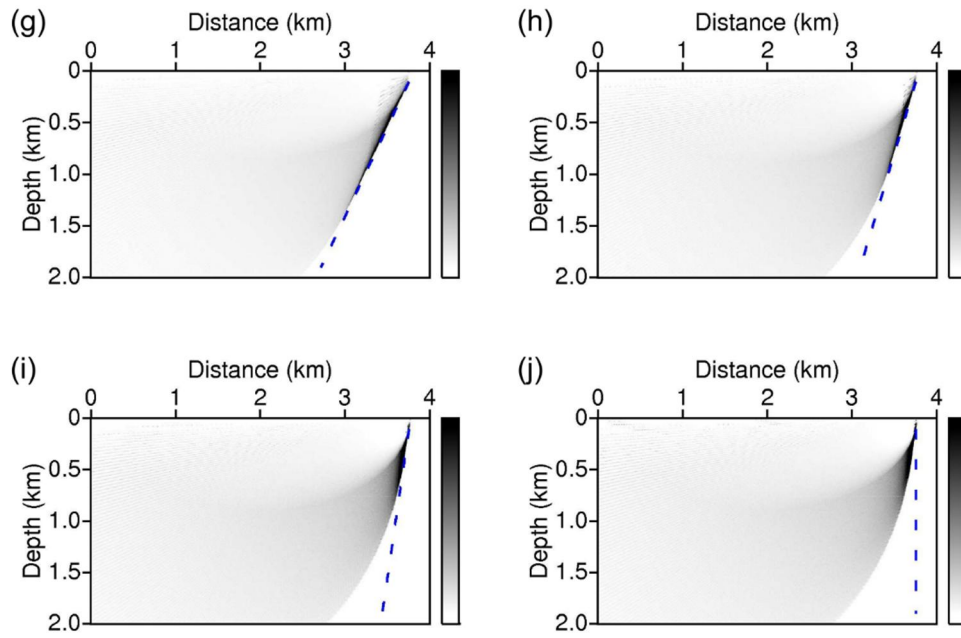


Figure 3.16 (Continued)

4 Applications of convolution-type SI

Because the proposed method resolves the subsurface media layer by layer, this method is more suitable for layered models than for complicated models. Hence, I assume two kinds of layered models. To investigate the feasibility of the proposed method for low-velocity layers, I first apply the proposed method to a homogeneous-layer model with a low-velocity layer. Because the proposed method is designed under the assumption that layers are homogeneous, I need to investigate the feasibility of this method for inhomogeneous layers. For this reason, I use an inhomogeneous-layer model whose velocity gradually increases in each layer. The proposed method is also applied to two kinds of simple dip-slip fault models and real field data (Congo data set).

4.1 The homogeneous-layer model

Figure 4.1 shows the homogeneous-layer model (excluding the virtual layer) with a low-velocity layer. It is assumed that the velocity of the third layer is lower than that of the second layer.

I first add a virtual layer, whose velocity and thickness are 1.3 km/s and 60 m, respectively, on the top of the model. The virtual layer is located at depths between -60 m and 0 m. Virtual sources are distributed on the virtual surface at distances ranging from -100 m to $1,350$ m with a regular interval of 0.4 m (at a depth of -60 m); 525 actual sources and 525 receivers are regularly distributed on the real surface (at a depth of 0 m).

I calculate the traveltimes of the virtual direct waves propagating from the virtual sources to the actual sources and receivers. Convolution gathers, from which we approximately determine the stationary points for the incident angles, are generated by convolving the virtual direct waves and the actual primary reflections (that is, a simple addition of the two traveltimes). To improve the reliability of the proposed method, the stationary points are not estimated when the stationary zone includes the first or last receiver in the convolution gather.

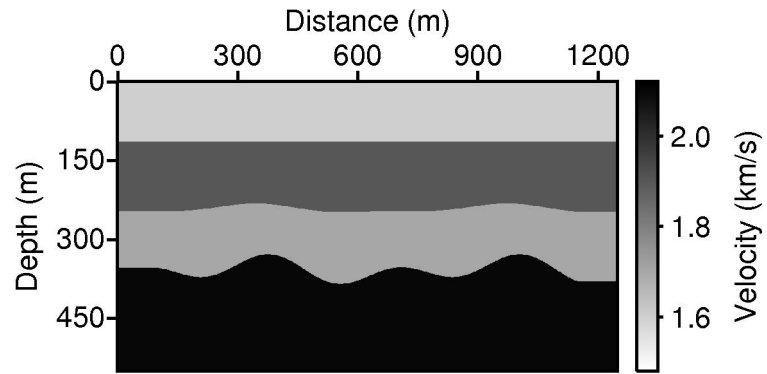


Figure 4.1 A homogeneous-layer model including a low-velocity layer. Actual sources and receivers are located on the real surface at distances from 100 m to 1,150 m with a regular interval of 2 m.

I first estimate the velocity and interface for the first layer by assuming that the velocity of the first layer ranges from 0.65 km/s to 2.6 km/s at an interval of 0.0013 km/s. For each assumed velocity, I locate the reflection points by applying Snell's law and calculate the traveltime differences between the observed and calculated data. Figure 4.2a shows the velocity estimation for the first layer shown in Figure 4.1 by using the first velocity estimation method. From Figure 4.2a, we can easily estimate the velocity of the first layer to be 1.599 km/s by selecting the velocity that gives the minimum traveltime difference. In practice, when we apply the first method to infer velocity, we need to carefully exclude reflection points with large deviations to reduce the error. Figure 4.2b shows the interface (bottom of the first layer) recovered from reflection points estimated by using the approximate stationary points.

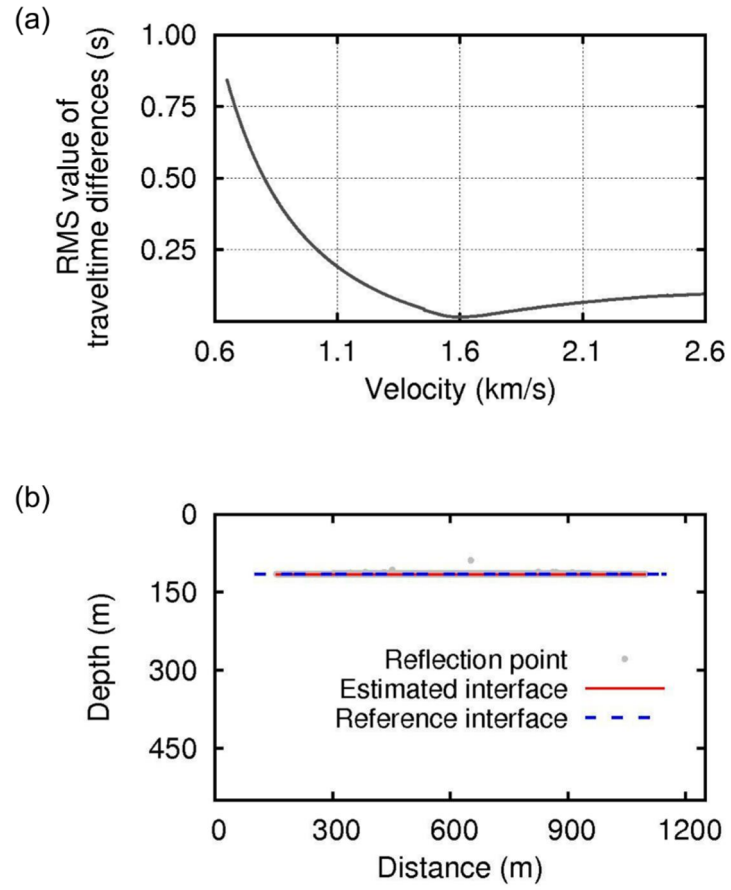


Figure 4.2 Estimation of (a) velocity and (b) interface for the first layer of the homogeneous-layer model.

After the velocity and structure of the first layer are reconstructed, the lower layers are estimated in a similar way. To improve the reliability of the results for the lower layers, the second and third velocity estimation methods are used together (Figure 4.3a). Figure 4.3a shows that the velocity with zero traveltime difference (the second method) coincides with the velocity with the maximum number of reflection points (the third method). The velocity estimated from Figure 4.3a is 1.873 km/s, which is very close to the true velocity of 1.9 km/s. Figure 4.3b shows the interface recovered from the deepest reflection points after plotting all possible reflection points for all sources and receivers. As shown in Figure 4.3b, the estimated interface (represented by the red line) matches up with the actual interface (denoted by the dashed dark blue line).

Figure 4.4a shows the velocity structures reconstructed by the proposed method for the whole model. I also compare the velocity-depth profiles estimated by the proposed method with the references at distances of 400 m and 750 m (Figure 4.4b). Figure 4.4 shows that the proposed method can successfully estimate the velocities and structures of the homogeneous-layer model, even though the stationary points are not accurately positioned.

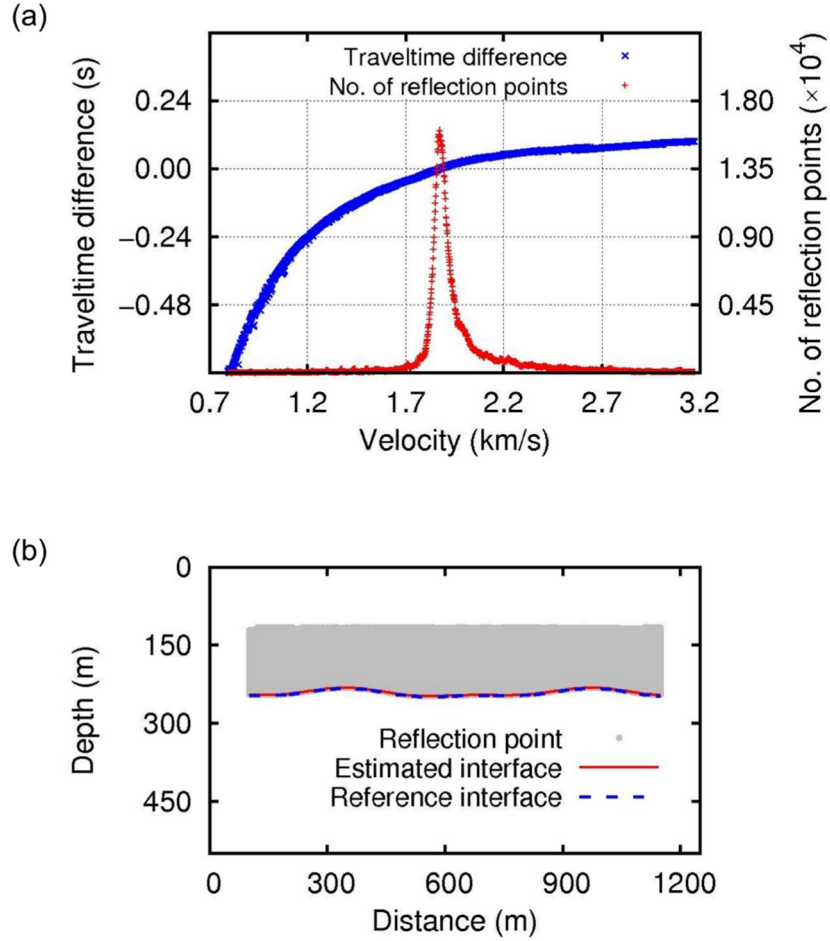


Figure 4.3 Velocity and interface estimation for the second layer of the homogeneous-layer model: (a) velocity estimation by the second and third methods; (b) interface estimation by using the estimated velocity.

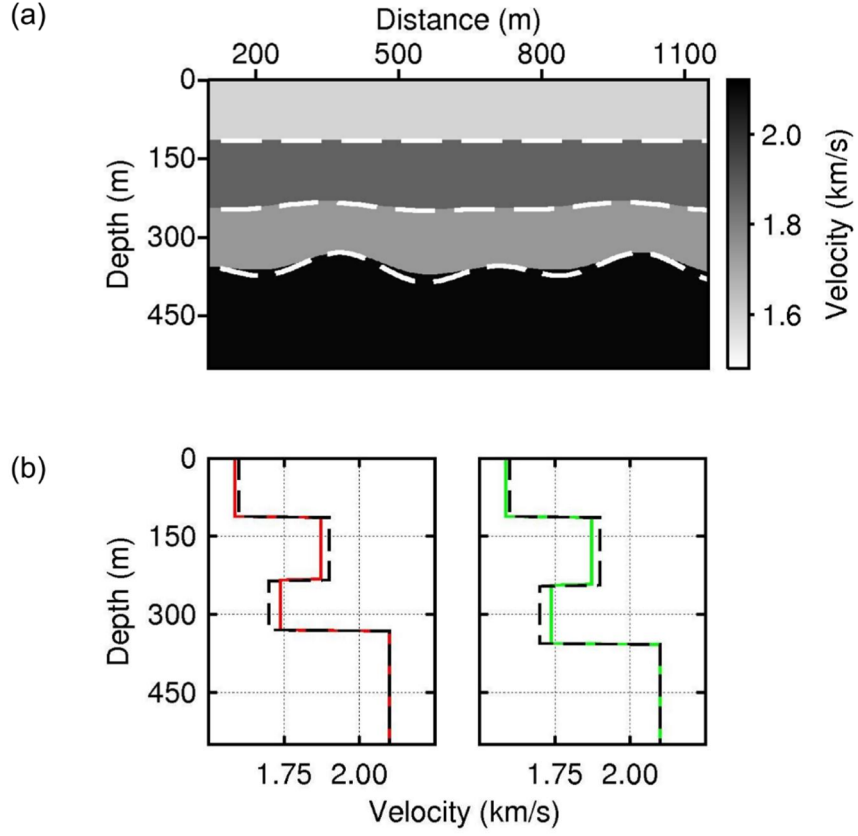


Figure 4.4 (a) P-wave velocity image obtained by the proposed method for the whole model shown in Figure 4.1; (b) depth profiles of the estimated velocities and the references (the dashed black lines) extracted at distances of 400 m (the red line) and 750 m (the green line). The dashed white lines indicate real interfaces.

4.2 The inhomogeneous-layer model

Figure 4.5 shows the inhomogeneous-layer model, whose velocity gradually increases in each layer. Although this model does not satisfy the basic assumption of the proposed method, I apply the same method that was applied to the homogeneous-layer model. I assume that the velocity and thickness of the virtual layer are 1.2 km/s and 60 m, respectively. As in the homogeneous-layer model, actual sources and receivers are distributed at a depth of 0 m, and virtual sources are located on the top of the virtual layer.

Figure 4.6a shows the traveltimes difference with the maximum number of reflection points and the number of reflection points with zero traveltimes difference for the first layer; from this figure, the velocity is estimated to be 1.718 km/s. Although the velocity gradually changes inside the layer, the proposed method gives only a representative velocity. Figure 4.6b shows the bottom surface of the first layer, and its depth is estimated to be 115.1 m, which is very close to the true depth of 114 m. After resolving the first layer, I move on to the second layer. Figure 4.7 shows the estimation of the velocity and reflection surface for the second layer. The velocity estimated for the second layer is 2.076 km/s, and the interface is well recovered.

Figure 4.8a shows the velocity image for the whole inhomogeneous-layer model. As shown in Figure 4.8b, I display the velocity-depth profiles at distances of 380 and 830 m. Figure 4.8 shows that, although the proposed method does not fully recover the true velocity structures due to its basic

assumption, the interfaces are well recovered.

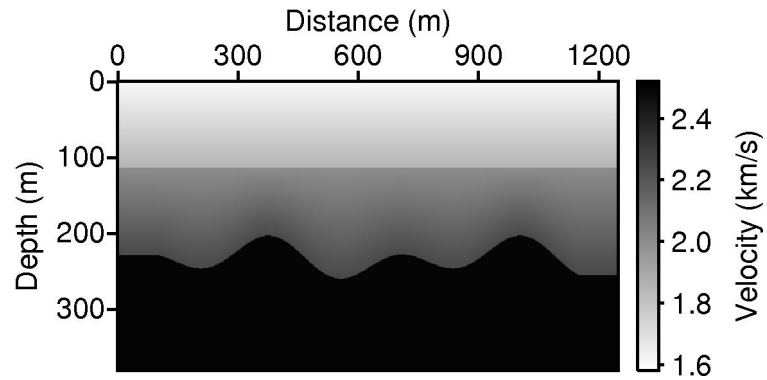


Figure 4.5 An inhomogeneous-layer model excluding the virtual layer: velocity increases gradually with depth in each layer. Actual sources and receivers are distributed on the real surface at distances from 100 m to 1,150 m with a regular interval of 2 m (at a depth of 0 m); virtual sources are located on the virtual surface at distances of -100 m to 1,350 m with a regular interval of 0.4 m (at a depth of -60 m).

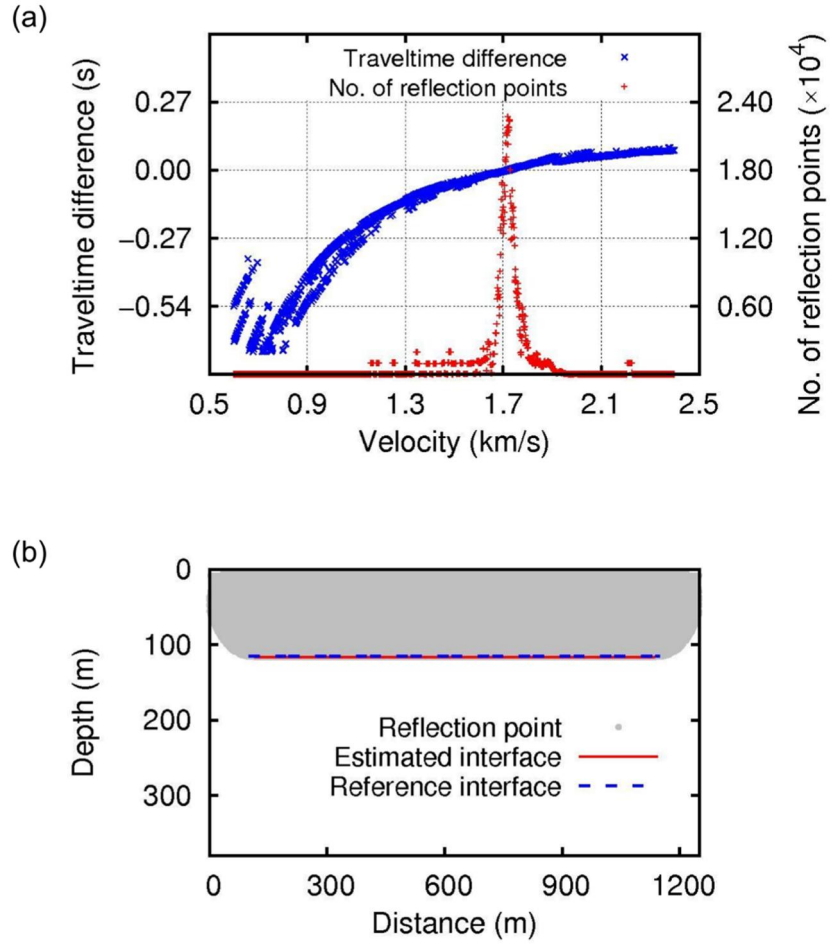


Figure 4.6 (a) Velocity and (b) interface estimation of the first layer for the inhomogeneous-layer model.

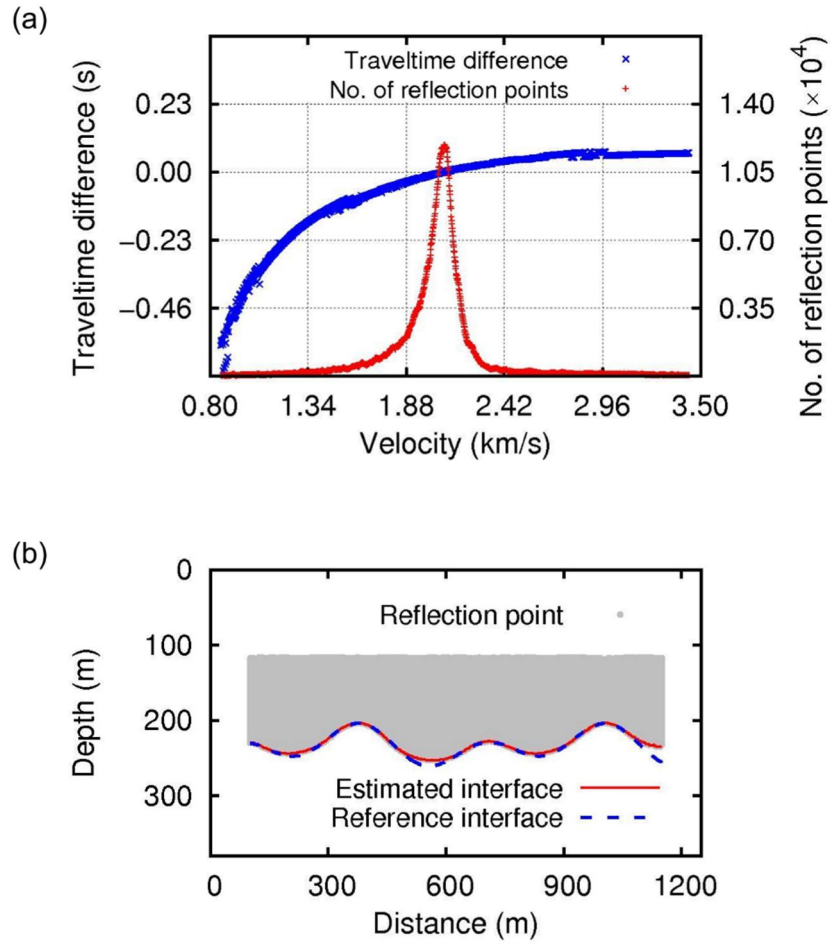


Figure 4.7 (a) Velocity and (b) interface estimation for the second layer shown in Figure 4.5.

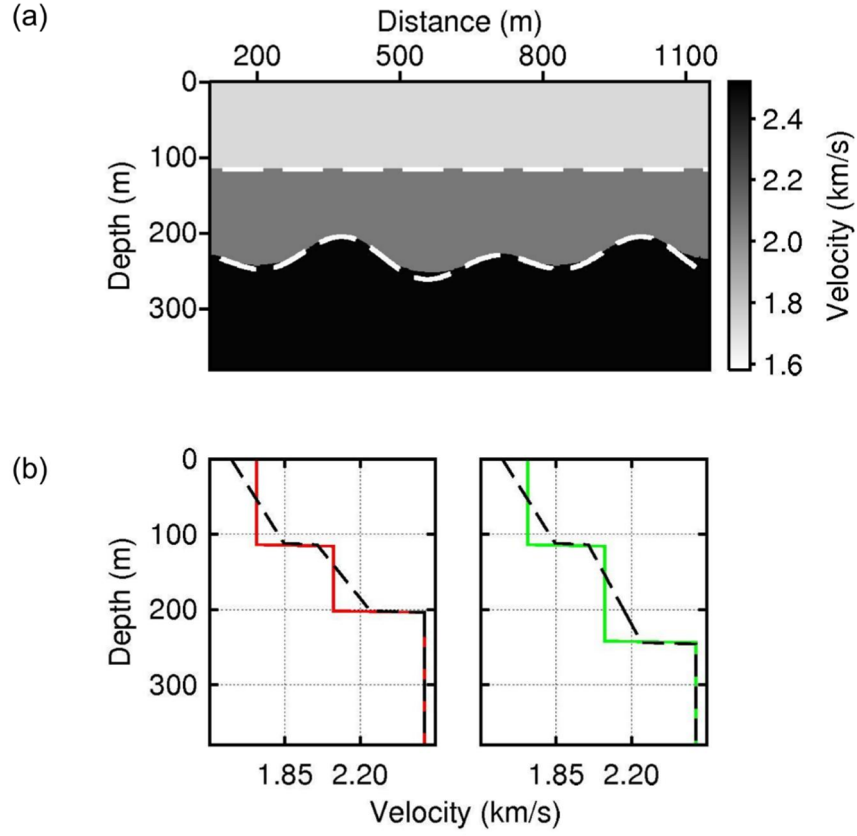


Figure 4.8 (a) P-wave velocity model obtained by using the proposed method for the whole inhomogeneous-layer model; (b) comparison of the estimated velocities and the references (the dashed black lines) extracted at distances of 380 m (the red line) and 830 m (the green line). The dashed white lines indicate real interfaces.

4.3 Fault model

The proposed method is also applied to the simple dip-slip fault model shown in Figure 4.9. Figure 4.10a shows an observed shot gather generated for the source located at a distance of 1.15 km. In Figure 4.10a, it is observed that the reflected waves in the left and right sides are separated, from which it is noticed that there exists a fault. The signals with good continuities are only picked for the velocity and structure estimations, whereas the signals with large slopes and small amplitudes are ignored. To easily pick reflections with good continuity, F-K filtering is applied before picking traveltimes (Figure 4.10b).

To estimate the incident angles, a virtual layer (whose velocity is 1.5 km/s) is added on the top of the actual surface, and 2,999 virtual sources at a depth of -0.75 km are used to calculate traveltimes of the virtual direct waves. Because the signals are separated in left and right sides, the velocity is estimated separately from data on each side.

Figure 4.11 shows the estimation of the first layer. The velocities obtained from data on each side (left or right) are identical (Figures 4.11a and 4.11c), and the velocity estimated combining both of them is also identical (Figure 4.11e). The interface is also recovered separately for left (Figure 4.11b) and right (Figure 4.11d) sides of the model. Because the estimated velocities are the same, the final interface is obtained combining the interfaces estimated separately from the data of the left- and right-sides

(Figure 4.11f).

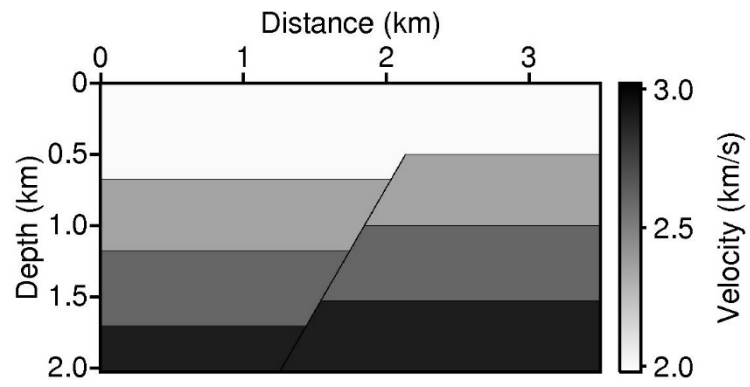


Figure 4.9 A fault model with the same velocity on both sides of the fault plane.

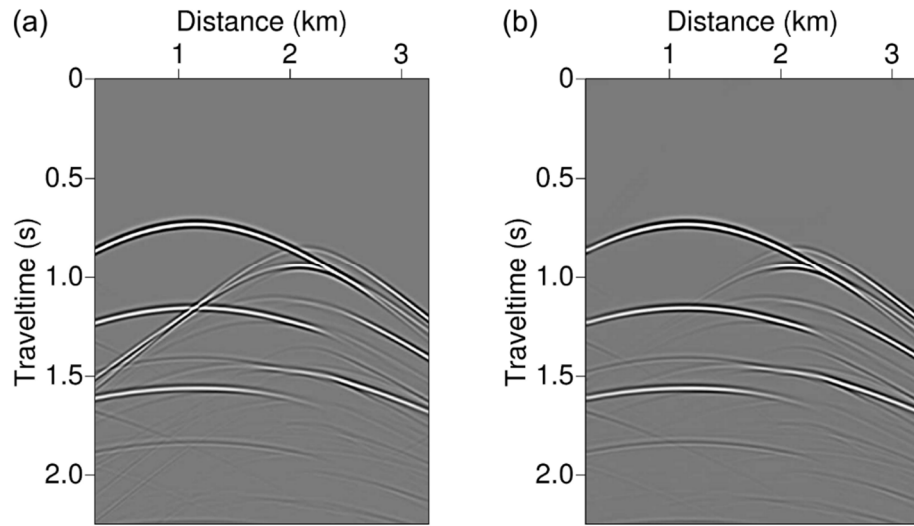


Figure 4.10 Observed CSGs (without the direct waves) (a) before and (b) after F-K filtering.

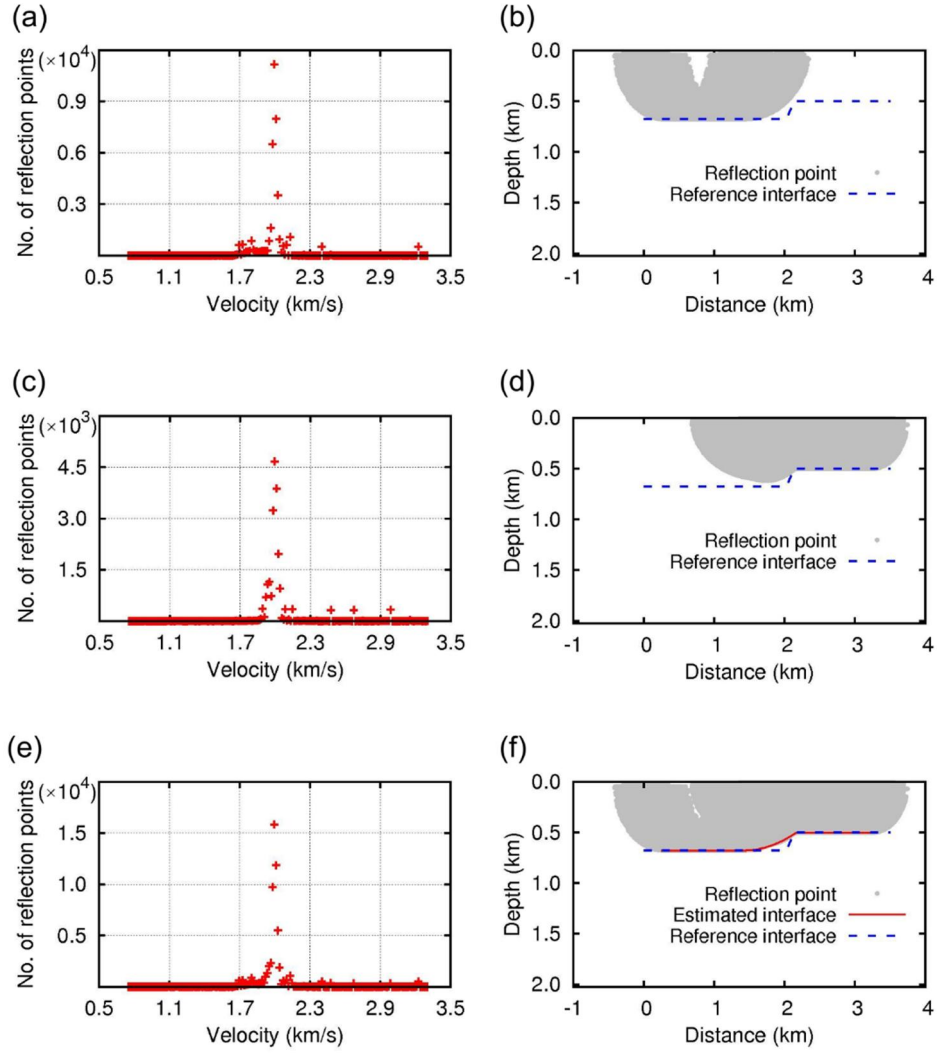


Figure 4.11 Estimation of (a, c, e) velocity and (b, d, f) interface for the first layer of the fault model shown in Figure 4.9 by using (a, b) left-side data, (c, d) right-side data and (e, f) both-sides data.

Estimation of the second layer is also similar to the first layer: the velocities inferred from the left side, right side and both of them are identical (Figure 4.12a). Thus, the interface can be obtained by combining the interfaces estimated from the left- and right-side data (Figure 4.12b).

For the third layer, velocities also give the same value, but it does not give a reliable connected reflection surface. Therefore, RTM is performed to recover the structure. The velocity model obtained by the proposed method (after smoothing) is used as a background model (Figure 4.13a). The linearly increasing model is also used as a background model for comparison (Figure 4.13b). Comparing the two results (Figures 4.13c and 4.13d), it is obvious that the proposed method gives a better result. It not only provides a more accurate structure, but also mitigates the migration effect (banana-shape).

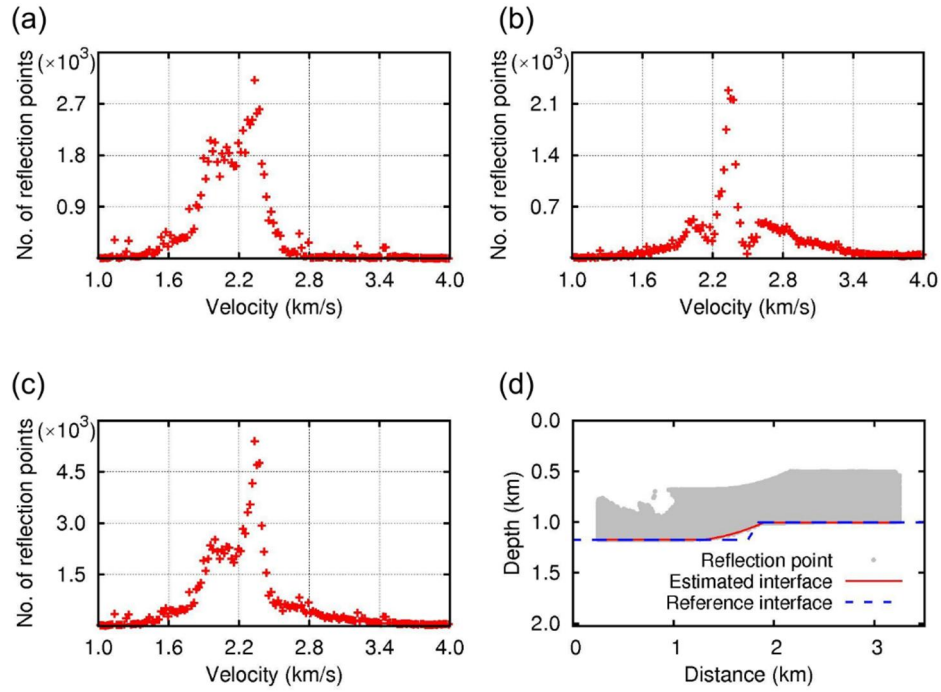


Figure 4.12 Estimation of (a, b, c) velocity and (d) interface for the second layer in Figure 4.9 by using (a) left-side data, (b) right-side data and (c, d) both of them.

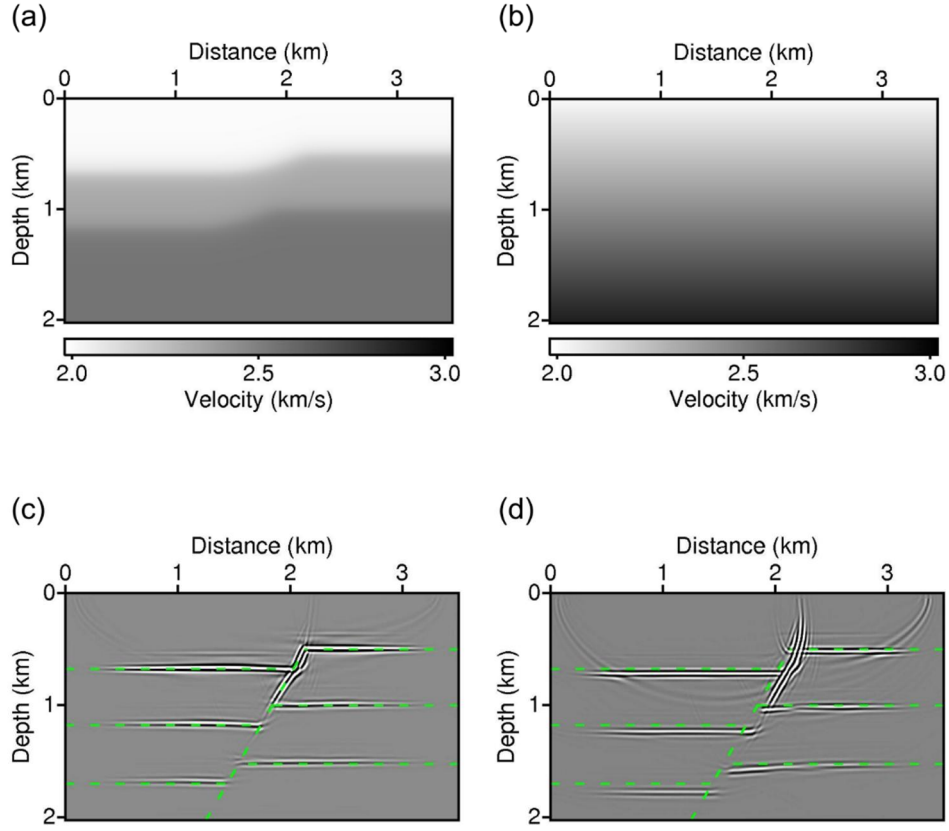


Figure 4.13 (a, b) Background velocity models and (c, d) RTM images for the fault model shown in Figure 4.9: (a) velocity model obtained by the proposed method; (b) the linearly increasing model; (c) RTM image obtained from the velocity model generated by the proposed method (a); (d) RTM image obtained using the linearly increasing model (b). The dotted green lines denote the real interfaces.

To investigate if the proposed method can also provide a reliable result when the velocities on both sides of the fault plane are different, the fault model shown in Figure 4.14a is used. The source and receiver geometry is the same as in the previous fault model. The F-K filter is also applied to improve the continuity of picked traveltimes.

Figure 4.15 shows the estimated velocity and interface of the first layer. As before, the velocities estimated using the left-side data, right-side data and both of them give the same value. Therefore, the interface is recovered by considering the whole data.

Unlike the first layer, the velocities estimated for the second layer by using the data on either side are different (Figures 4.16a and 4.16b). Thus, the interfaces estimated separately are not combined (Figures 4.16c and 4.16d).

Figure 4.17 shows the velocity estimation of the third layer. Comparing Figures 4.17a and 4.17b, it is observed that the left-side data gives the most reflection points at a low velocity of 1.936 km/s (Figure 4.17a). Note that the estimated velocity of the upper layer is 2.175 km/s. However, in the observed CSG (Figure 4.14b), it does not show polarity reversal. Moreover, in Figure 4.17c, although the number of total reflection points decreases near 2.35 km/s, it shows a flat pattern before 2.8 km/s (denoted by the dashed red ellipse). The dropping phenomenon before 2.45 km/s may be caused by the limitation of the upper reflection surface (i.e., the top of the

target layer). The stationary points are determined from all of the possible data. However, only part of the upper interface has been recovered. As a result, the number of total reflection points decreased. As mentioned before, the total reflection point curve will rapidly decrease when it passes through the true value (or the most possible value). In Figure 4.17c, it shows a short flatness. Considering this phenomenon and the characteristic of the observed seismogram, the potential velocity can be estimated to be a value between 2.4 km/s and 2.8 km/s. Thus, I choose the value of 2.458 km/s from the flat range as the velocity of the third layer (left side) (Figure 4.17d).

After obtaining the whole velocity structure, a smoothed version of the velocity model estimated by the proposed method is used as a background model for RTM to obtain a more accurate subsurface image. Comparing the RTM image with that obtained from the linearly increasing model, it is noted that the proposed method can provide a reliable starting model for subsequent imaging methods (Figure 4.18).

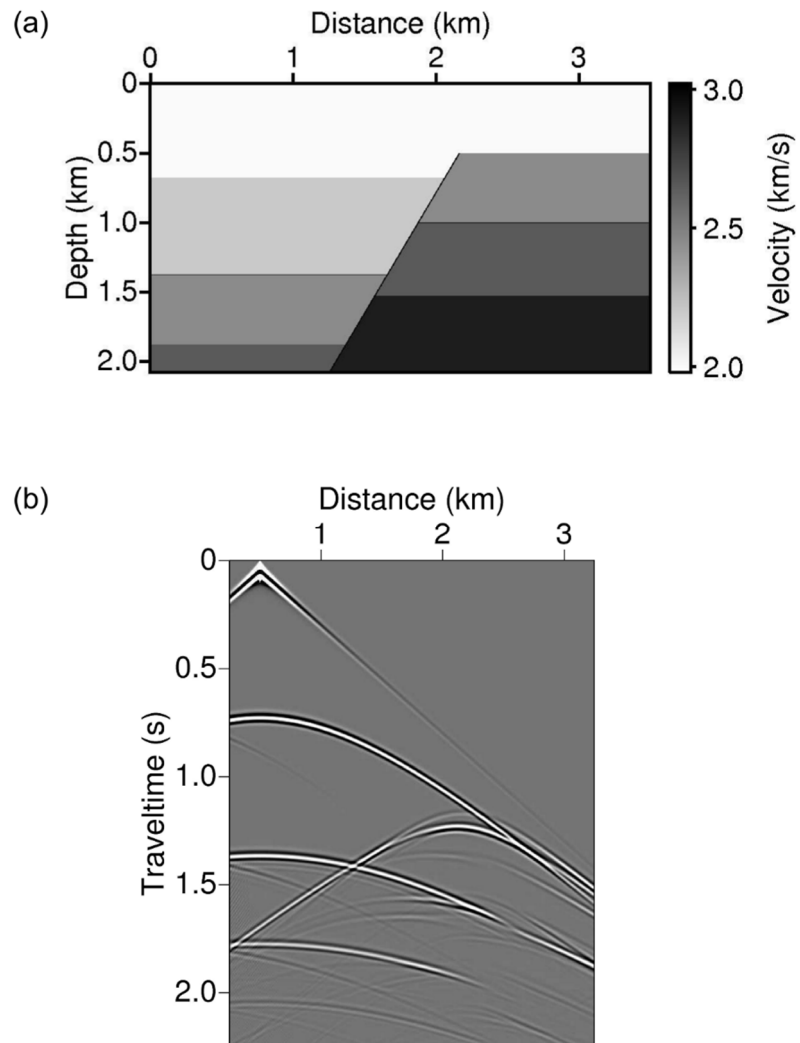


Figure 4.14 (a) A fault model whose velocities are different on both sides of the fault plane and (b) a CSG generated from the fault model.

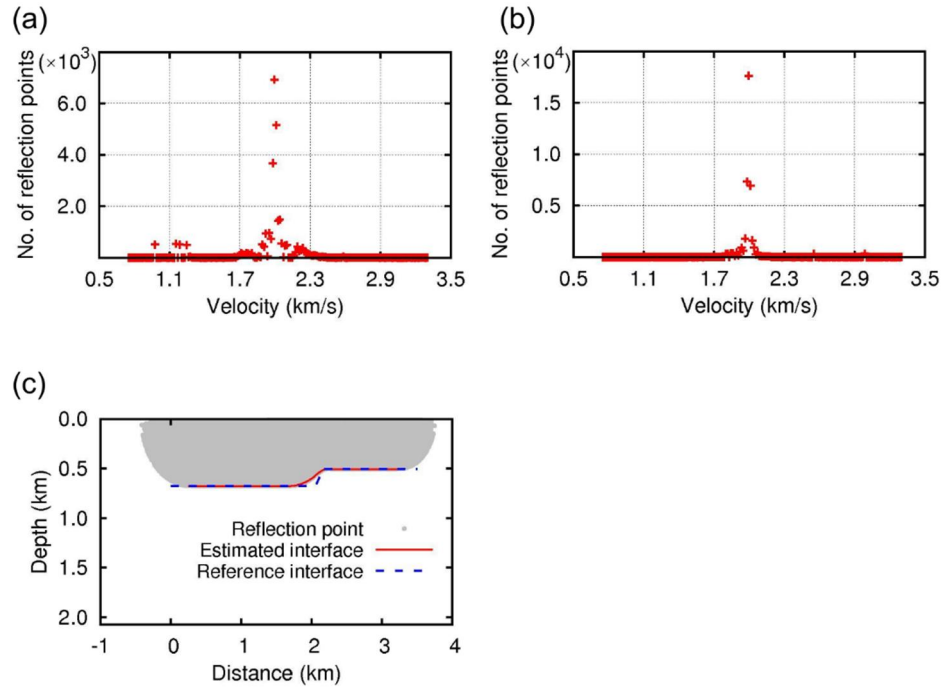


Figure 4.15 Estimation of (a, b) velocity and (c) interface for the first layer in Figure 4.14a by using (a) left-side data, (b) right-side data and (c) both of them.

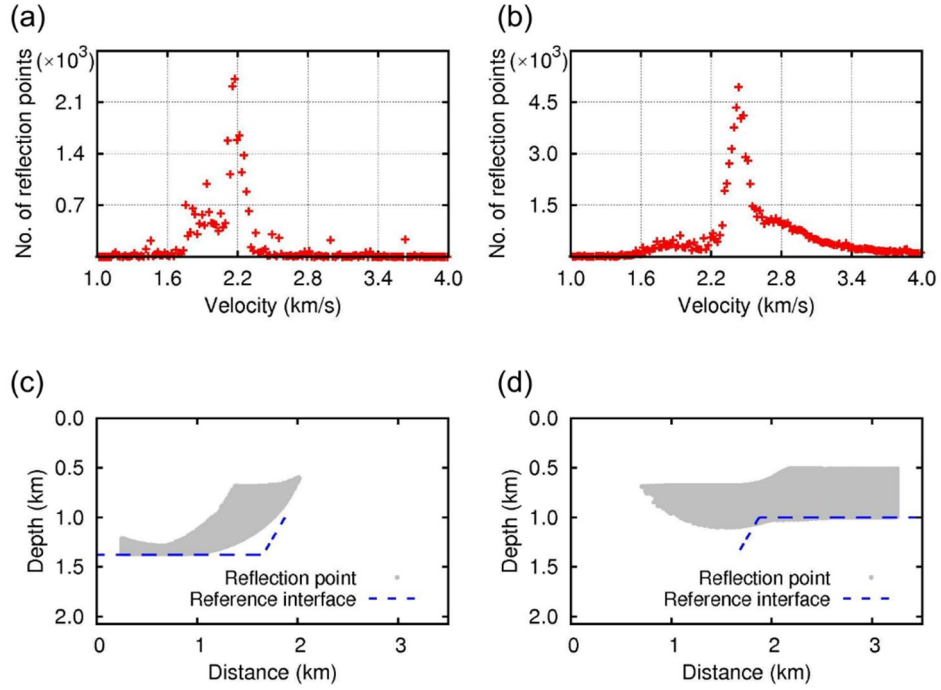


Figure 4.16 Estimation of (a, b) velocity and (c, d) interface for the second layer in Figure 4.14a by using (a, c) left- and (b, d) right-side data.

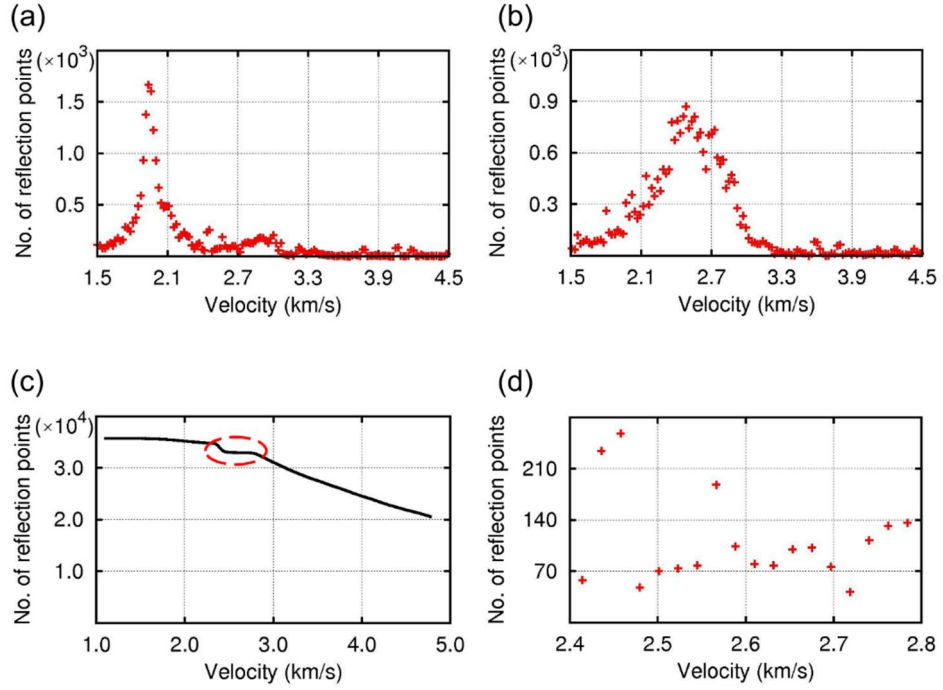


Figure 4.17 Velocity estimation for the third layer in Figure 4.14a by using (a) left- and (b) right-side data; (c) total number of reflection points versus assumed velocity; (d) zoom-in version of (a).

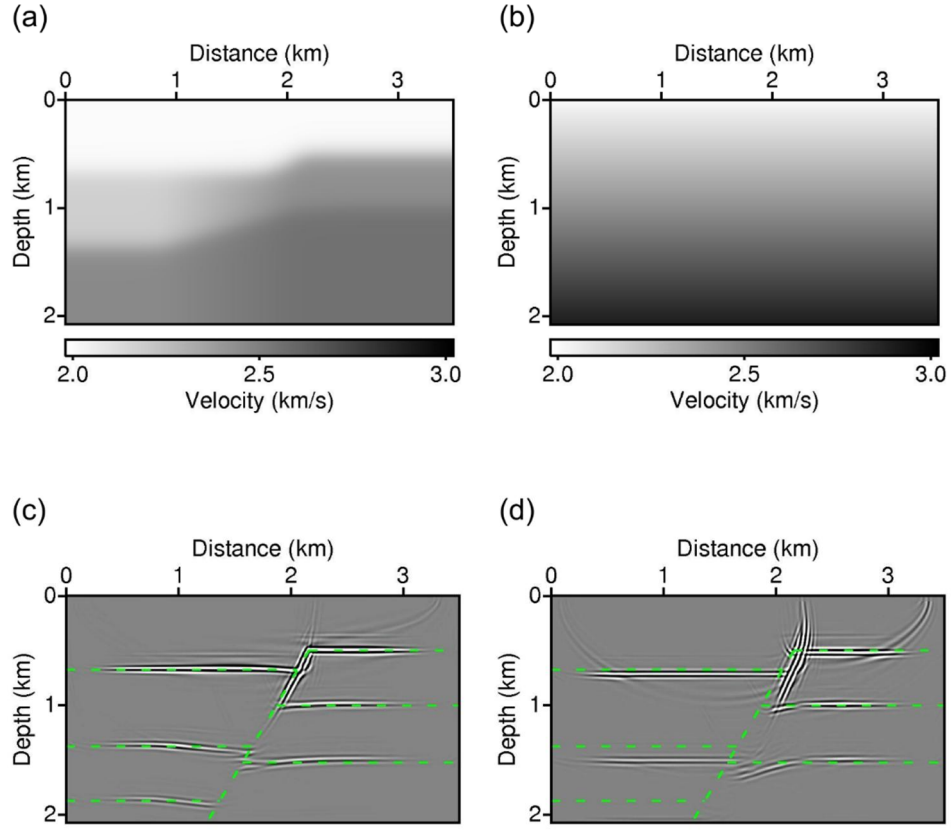


Figure 4.18 (a, b) Background velocity models and (c, d) RTM images for the fault model shown in Figure 4.14a: (a) velocity model obtained by the proposed method; (b) the linearly increasing model; (c) RTM image obtained from the velocity model obtained by the proposed method (a); (d) RTM image obtained from the linearly increasing model (b). The dotted green lines denote the real interfaces.

4.4 Real data

To demonstrate the applicability of the proposed method to real field data, I apply the method to marine seismic data (Congo data) acquired in the Gulf of Mexico (Figure 4.19). I selected 111 shot gathers with the sources ranging from 3.14 km to 8.64 km from the full data set. Figure 4.19b shows a representative CSG with 120 channels. The shot jump interval is 50 m, the receiver interval is 25 m, and the nearest offset is 138 m. The frequency spectrum of data ranges from 5 Hz to 120 Hz.

I began by picking primary reflections. In general, marine data feature strong multiple reflections; therefore, it is difficult to distinguish primary reflections from multiples in raw CSGs. Furthermore, it is not easy to select hyperbolic reflections from identical layers across a number of CSGs. For this reason, I first pick primary reflections in a common offset gather. If we distribute the picked points to CSGs, they will appear as a point in each CSG. Based on these points, I pick the whole hyperbola in each CSG. Figure 4.19a shows reflections picked in a common offset gather recorded at the nearest receiver, and Figure 4.19b shows hyperbola picked in a CSG in the aforementioned manner. Although a number of reflections are observed in the shot or receiver gathers, I only consider two main primary reflections in this experiment. Because I do not consider all the primary reflections, the velocities estimated by the proposed method can act as representative velocities for several adjacent layers rather than true velocities.

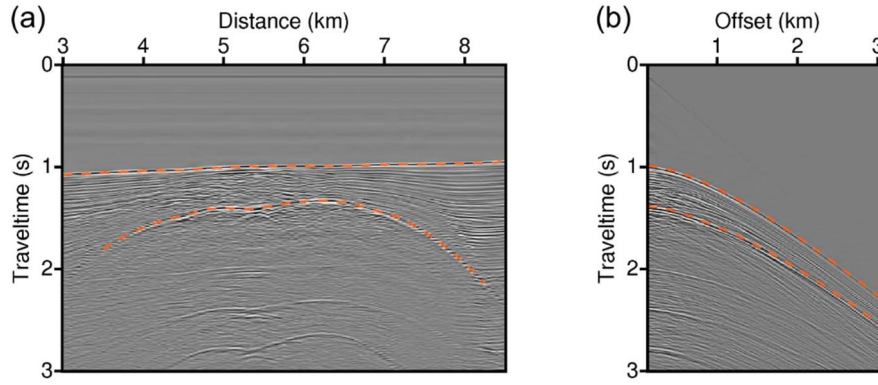


Figure 4.19 The real data acquired by using a streamer including 120 traces in each CSG: (a) picking traveltimes in the common offset gather; (b) picking traveltimes in the CSG. The dotted orange lines indicate picked traveltimes of reflections.

To determine the stationary points, a virtual layer with a velocity of 1.52 km/s and a depth of 0.75 km is added, similar to the synthetic examples. The virtual sources are located at the virtual surface (from -8.5 km to 17 km with an interval of 0.005 km).

Figures 4.20 shows estimation of velocity (velocity of sea water) and interface (sea bottom) for the first layer. From Figure 4.20a, we can easily estimate the velocity of sea water to be 1.4972 km/s. The sea bottom is inferred by using the estimated velocity (Figure 4.20b). To easily recover the reflection surface, I divide the selected deepest reflection points into several parts and apply curve fitting to each part.

As I mentioned before, because I do not consider all reflections above the salt body, the top of the salt dome is estimated by determining the representative velocity for the layers between the sea bottom and the top of the salt body. For convenience, the bulk layer covering the region from the sea bottom to the top of the salt body will be designated the second layer. Before I proceed to determine the velocity of the second layer, I estimate the velocity representing the layers between the sea surface and the top of the salt body, which corresponds to the RMS velocity to the top of the salt body. This RMS velocity helps us determine the velocity range of the second layer. In field data experiment, we are prone to suffer from insufficiency of data, in which case the number of reflectors with zero traveltimes difference does not show an ideal pattern. For this reason, we need to narrow the range of velocity. Figure 4.21a shows the number of reflectors with zero traveltimes

difference for the RMS velocity. In Figure 4.21a, the RMS velocity is estimated to be approximately 1.6 km/s, which means that the velocity of the second layer is larger than 1.6 km/s. Therefore, I assume that the velocity of the second layer ranges from 1.6 km/s to 4.5 km/s. Figure 4.21b shows the number of reflectors with zero traveltimes difference for the second layer, from which the velocity of the second layer is estimated to be 1.7 km/s. Figure 4.21c shows the top of the salt dome inferred by using the estimated velocity.

After I obtain the velocity structure by using the proposed method, I perform RTM by using the estimated velocity as a background velocity. Figures 4.22 shows the background velocity and RTM image. In Figure 4.22b, it is observed that the shallow layers and the top of the salt body are well described. These results show that the proposed method can be effectively used to obtain an initial guess for a subsequent seismic imaging technique in cases in which there is a lack of *a priori* information of subsurface structures.

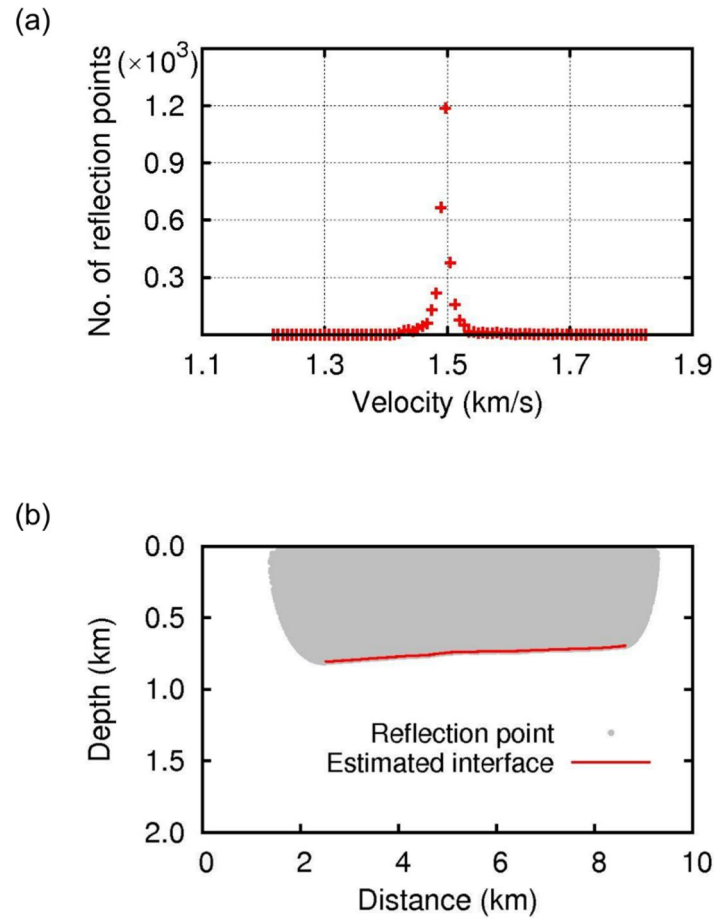


Figure 4.20 Velocity and interface estimations for the real data by using the first picked reflections shown in Figure 4.19: (a) estimating velocity of sea water; (b) estimating structure of the sea bottom.

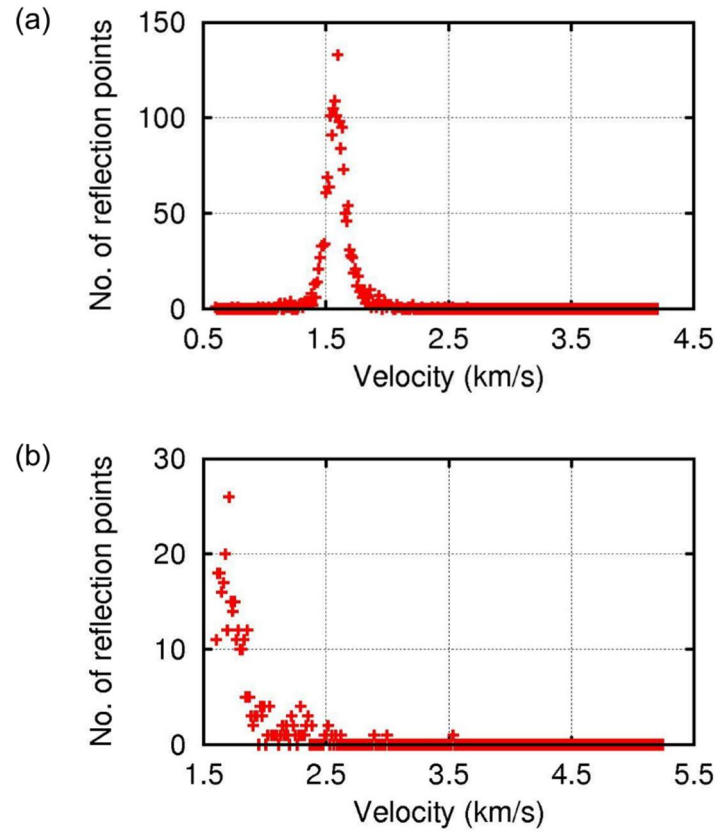


Figure 4.21 Velocity and interface estimations for the real data by using the second picked reflections shown in Figure 4.19: (a) estimating the apparent velocity ranging from about sea surface to the top of the salt dome; (b) estimating the velocity of the top of the salt dome; (c) estimating structure for the top of the salt dome.

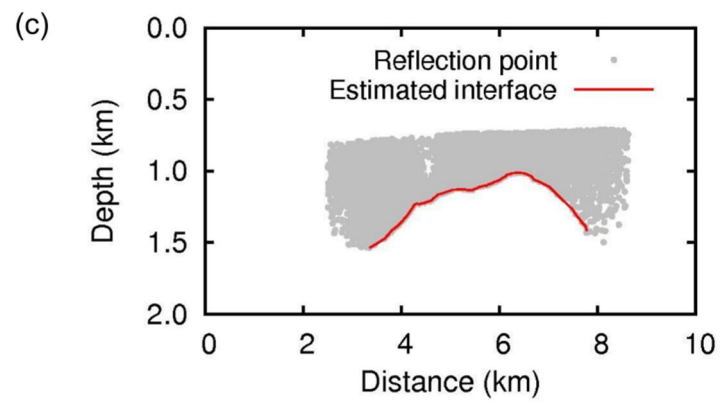


Figure 4.21 (Continued)

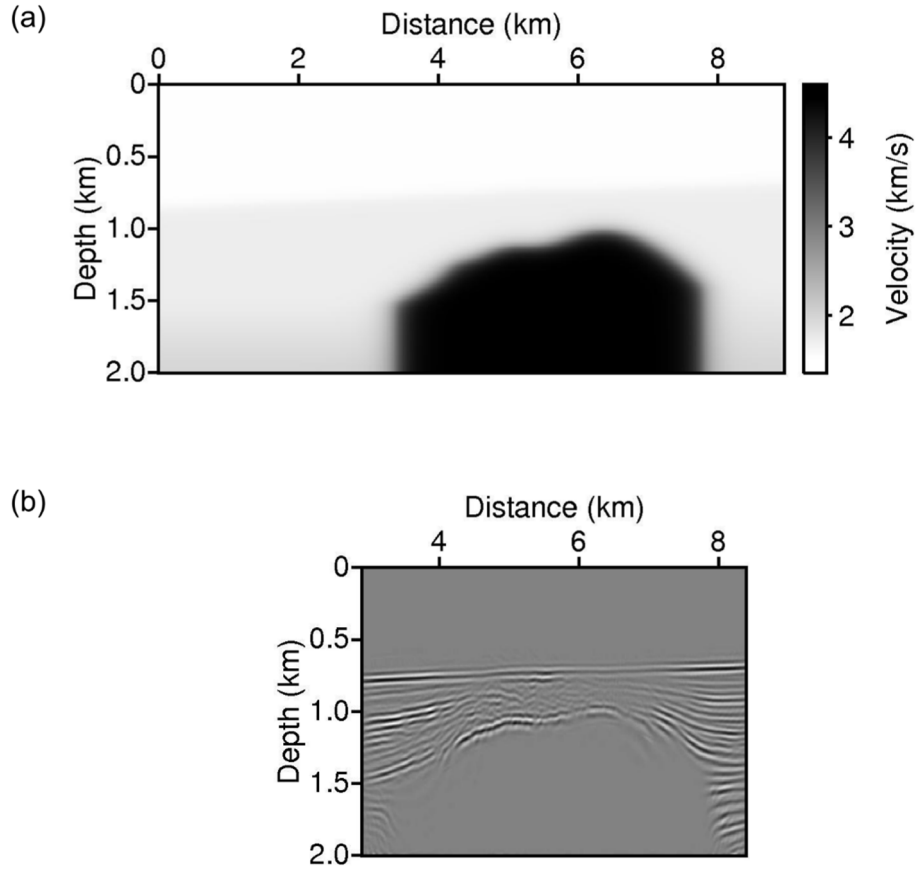


Figure 4.22 Background velocity model and RTM image for the real data shown in Figure 4.19: (a) background velocity model obtained by the proposed method; (b) the corresponding RTM image generated from the real data.

4.5 Discussion

Conventional RTT methods recover both velocities and structures at the same time by solving nonlinear problems based on large matrix equations. Accordingly, these methods are prone to suffer from the non-uniqueness problem and depend on initial guesses. In the proposed method, velocities and structures are sequentially reconstructed. By determining stationary points via convolution-type SI, we can avoid the non-uniqueness problem and do not have to solve a large matrix equation. Therefore, we can save the computer memory and computational time required for solving a large matrix equation and do not have to apply parallel computation. To apply convolution-type SI, I assume a virtual layer whose properties are already known, and this method enables us to recover subsurface structures without *a priori* information. Although the velocity of the virtual layer can be assumed randomly, to obtain more stationary points, it is better to assume a value within the general subsurface velocity range, such as 1.5 km/s, 2.0 km/s and 3.0 km/s. In these aspects, I can say that the proposed method is computationally efficient and robust compared to conventional methods.

The proposed method can estimate velocity by using three methods: considering the average of the traveltimes differences, considering traveltimes differences with the most number of reflection points and considering the numbers of reflection points with zero traveltimes differences. All three methods can infer the velocity with high accuracy. However, the average can be affected by the estimated reflection points with large traveltimes

differences. Therefore, it is necessary to remove the large deviation values before calculating the average value. If the traveltime difference with the most reflection points is used alone, it is impossible to exclude the values that gives zero traveltime difference with a small amount of reflection points. Thus, considering the numbers of reflection points with zero traveltime differences is a better way to avoid these problems. However, if the stationary points are not sufficient, it will give a range of velocities instead of a value with the most reflection points (Figure 5.5 in the next chapter). Therefore, I suggest first checking the total reflection point curve and then using two or three methods together to reduce errors.

For the inhomogeneous-layer model shown in Figure 4.5, although the proposed method well describes layer interfaces, this model does not describe the velocity changes in each layer and instead provides a representative velocity (or an apparent velocity) for each layer. The apparent velocity can vary with offset. Thus, the proposed method is also applied to data with different maximum offsets. Figure 4.23a shows the velocity estimation for the first layer, shown in Figure 4.5. As shown in Figure 4.23a, although the numbers of reflection points are different, the estimated velocities are almost identical except for the nearest offset. This result is because the interface (bottom of the first layer) is flat, in which case the variation in the apparent velocity with offset is not too large. Figure 4.23a also shows that the data with larger offsets (200 m, 300 m and 400 m) have similar numbers of reflection points because the amount of large-offset data is small compared to that of near- and middle-offset data, and the reflection

points are mainly generated by the near- and middle-offset data. Figures 4.23b and 4.23c show the estimation of the velocity by considering the number of reflection points with zero traveltime difference and the reconstruction of the reflection interface for the second layer, respectively. When the maximum offset is 50 m, the number of reflection points smoothly changes with velocity (Figure 4.23b). In this case, we cannot determine an appropriate velocity. When there are a relatively high number of reflection points, the velocities (Figure 4.23b) and interfaces (Figure 4.23c) estimated for the second layer slightly change with offset. These results show that with only near-offset data, we cannot properly estimate velocities and interfaces. Comparing the numbers of reflection points obtained for the first and second layers, the number of reflection points clearly decreases moving downward. Considering that the proposed method requires good continuity of picked traveltimes laterally, the error increases as the number of layers increases. Therefore, I propose applying the proposed method to data with a sufficiently large offset or, more precisely, applying the method to a sufficient amount of data.

In the proposed method, we need to determine incident angles in both source and receiver positions to locate the reflectors; therefore, the estimation of incident angles is carried out in both shot and receiver gathers. When the shot jump interval is double the receiver interval, as in the Congo data, the number of traces in the common receiver gathers are half that of the CSGs. In the Congo data, the number of traces is 120 in CSGs, but only 60 in receiver gathers. In this case, insufficient data can affect the number of

reflection points estimated by using the incident angles, particularly for lower layers. Another difficulty encountered in field data experiments is picking traveltimes. It is not easy to distinguish primary reflections from multiples in the shallow marine environment and select hyperbolas originating from identical layers across CSGs. One simple way to avoid those problems is to remove multiples before applying the proposed method. Further research is needed to develop an effective method for picking primary reflections.

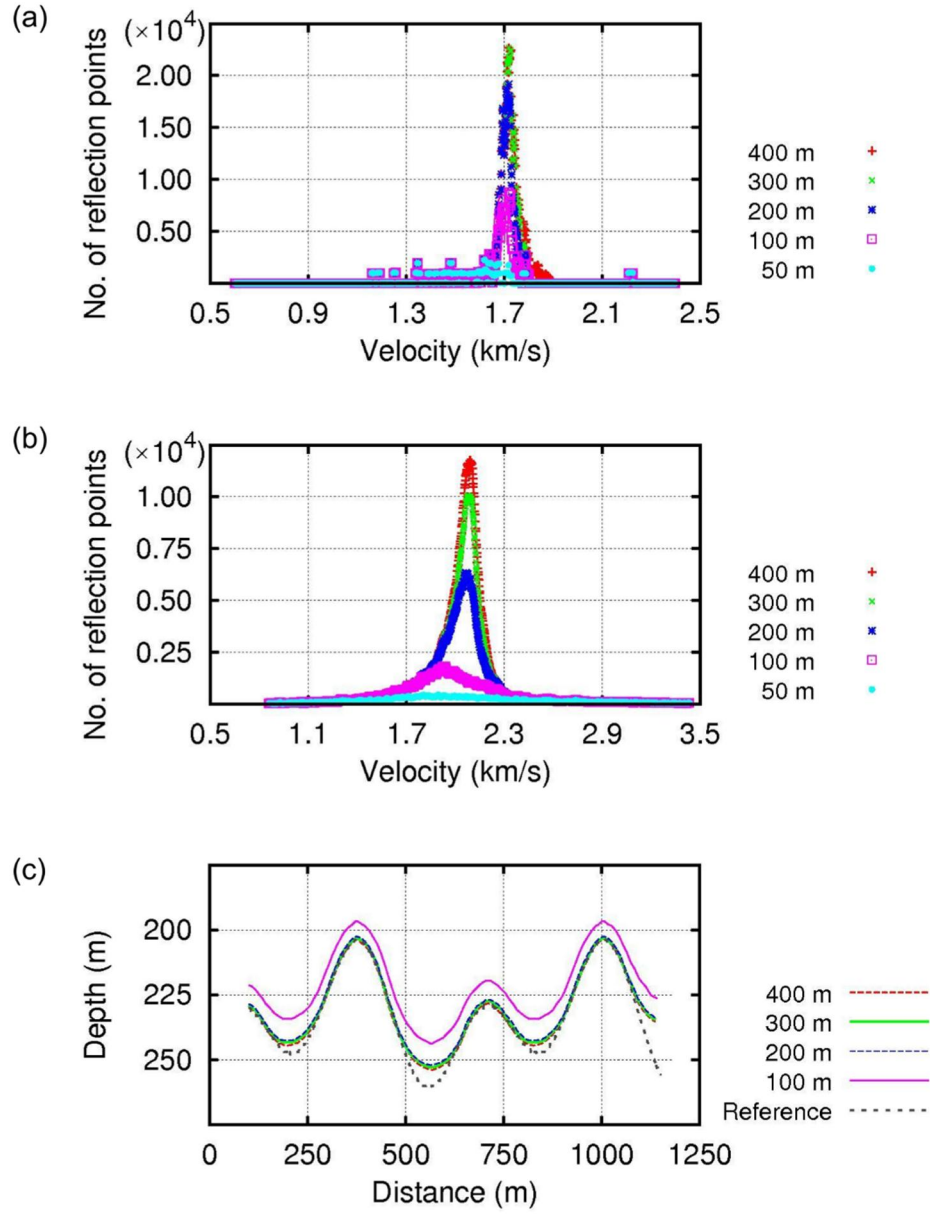


Figure 4.23 Velocity estimations with different maximum offsets for (a) the first and (b) second layers of the inhomogeneous-layer model shown in Figure 4.5; (c) interfaces recovered with the velocities estimated from the different maximum offsets for the second layer.

5 Comparison of different wave combinations

As I mentioned before, we can use different types of wave combinations to estimate stationary points. Figure 5.1 shows characteristics of the three methods. M1 (Figure 5.1a) requires a virtual layer above the real surface. The stationary point R is estimated from the convolution gather of the virtual direct wave S'R and the actual primary reflection SxR generated at the interface. M2 (Figure 5.1b) uses correlation of the direct wave (S'R) of the first layer with the primary reflection (SxR) from lower interface. M2 works on the original method under the assumption that information of the first layer is already known. M3 (Figure 5.1c) uses the convolution gather generated by the primary reflection (S'x'R) of the first layer and the primary reflection (SxR) of the lower layer. Unlike M1 and M2, M3 generates a multiple. In the case that we already know the velocity and structure of the first layer, we can determine the propagation direction of the ray x'R. Therefore, we can derive the incident angle θ of the second layer from the propagation direction of the ray RR'. Because M2 and M3 require information of the first layer, velocity and structure derived by M1 are used for the information of the first layer. In this chapter, the three types of wave combinations are also applied to the homogeneous- and inhomogeneous-layer models.

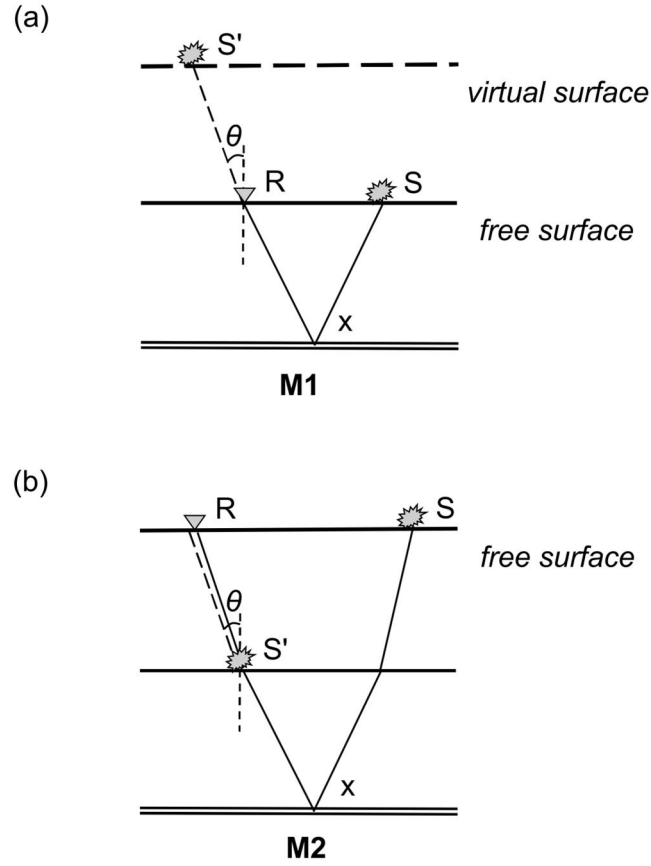


Figure 5.1 Three types of wave combinations used to estimate velocity of the lower layer: (a) M1 uses convolution of the virtual direct wave and primary reflection; (b) M2 uses cross-correlation of the direct wave with primary reflection; (c) M3 uses convolution of two primary reflections. R and θ indicate the stationary receiver point and incident angle, respectively; surfaces denoted by the dashed and double lines denote virtual surface and interfaces needed to be inferred, respectively; raypaths indicated by the solid and dashed lines are the actual and virtual raypaths generated by assuming virtual sources (S' in M1 and M2), respectively.

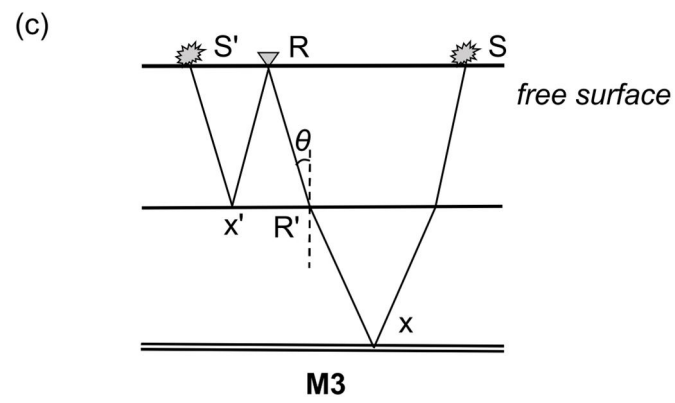


Figure 5.1 (Continued)

5.1 The homogeneous-layer model

The homogeneous-layer model with a low-velocity layer shown in Figure 4.1, which is used in the previous chapter, is also used in the comparison of three different types of wave combinations. Because M1 does not require *a priori* information to resolve the first layer, I first recover velocity and interface of the first layer by using M1, and the estimated velocity and interface will be also used in both M2 and M3.

Unlike in the previous chapter, in this section, the second and third velocity estimation methods are used for the first layer velocity estimation (Figure 5.2a). Figure 5.2a shows traveltime difference with maximum number of reflection points and the number of reflection points whose traveltimes are the same as recorded ones. In Figure 5.2a, the velocity of the first layer is inferred to be 1.5873 km/s (whose reference velocity is 1.6 km/s) by choosing velocity that gives zero traveltime difference with the largest number of reflection points. Figure 5.2b shows reflection points obtained by using the inferred velocity for all possible sources and receivers. Then the interface between the first and second layers is recovered from the deepest reflection points.

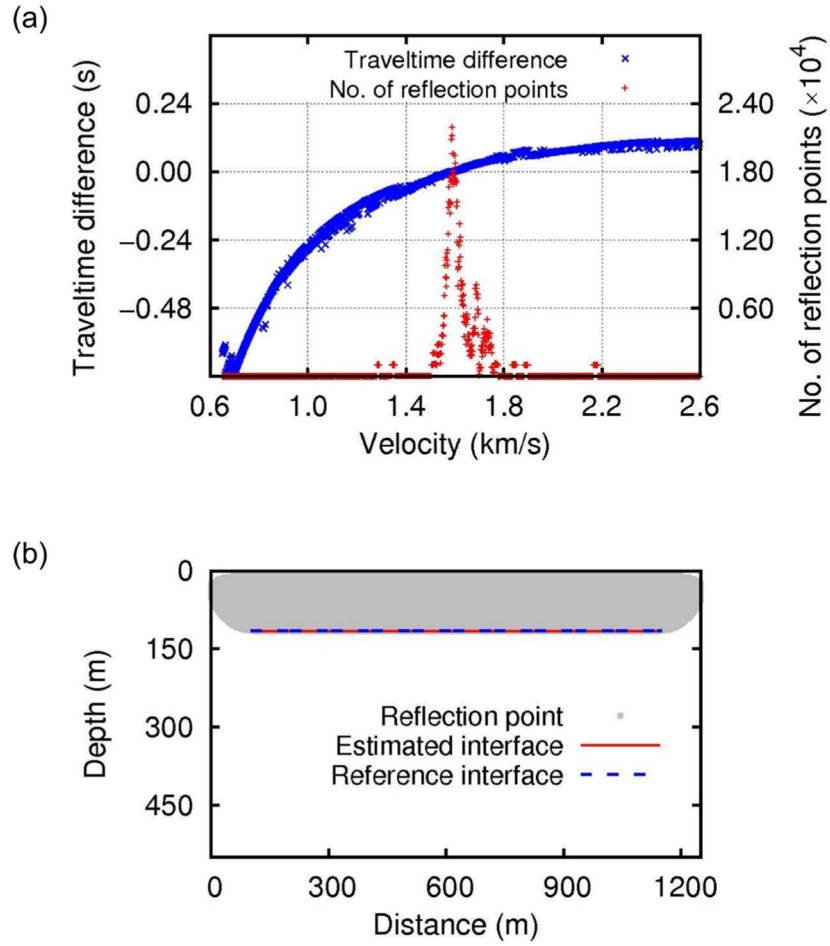


Figure 5.2 (a) Velocity and (b) interface estimation of the first layer for the homogeneous-layer model by applying M1.

After the velocity and structure of the first layer are estimated, lower layers are resolved in a similar way. Figures 5.3, 5.4 and 5.5 show velocity and interface estimations by applying three different combinations: in M1, virtual sources are the same as the first layer estimation; in M2, virtual sources, shown as S' in Figure 5.1b, are located at distances ranging from 100 m to 1150 m with a spacing of 0.4 m along the bottom of the first layer; in M3, both sources and receivers used to generate convolution gathers are the actual ones. In the velocity estimation of the second layer, the second and third methods are considered together. In M2, we need an additional process of redatuming sources and receivers to the interface of the first and second layers. Unlike M1 and M2 (Figures 5.3a and 5.4a), M3 shows a different tendency. That is, the number of reflection points that gives zero traveltime difference is large over a range of velocities rather than a specific velocity (Figure 5.5a), which is because M3 does not yield sufficient stationary points. In this case, the RMS value of traveltime differences is considered together (Figure 5.5b) to choose an appropriate velocity. In Figure 5.5b, we can easily choose velocity (1.9063 km/s) that yields minimum traveltime difference. Figure 5.5c shows interface recovered by M3. Results are similar to those obtained by M1 and M2 (Figures 5.3b and 5.4b).

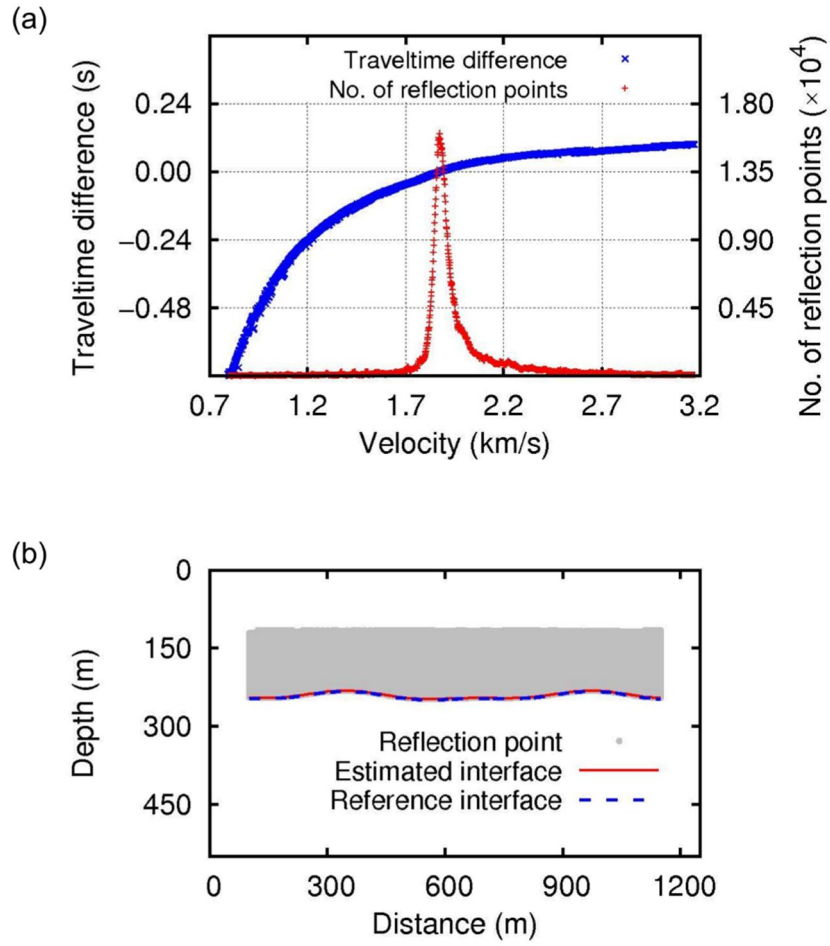


Figure 5.3 (a) Velocity and (b) interface estimation of the second layer for the homogeneous-layer model by applying M1.

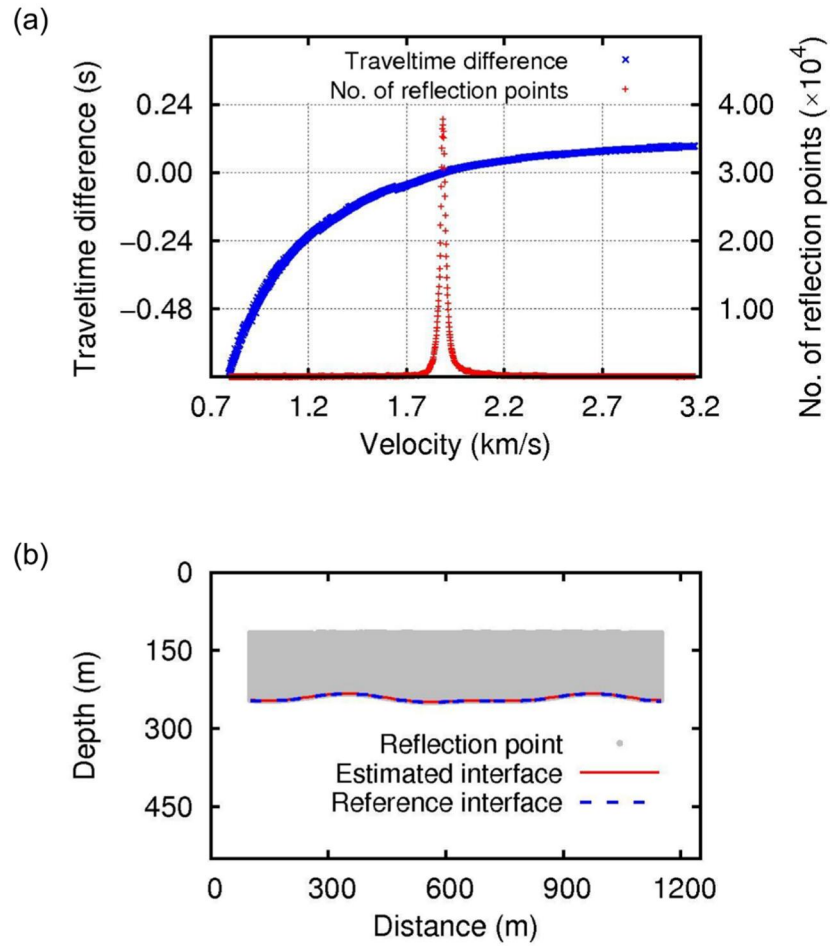


Figure 5.4 (a) Velocity and (b) interface estimation of the second layer for the homogeneous-layer model by applying M2.

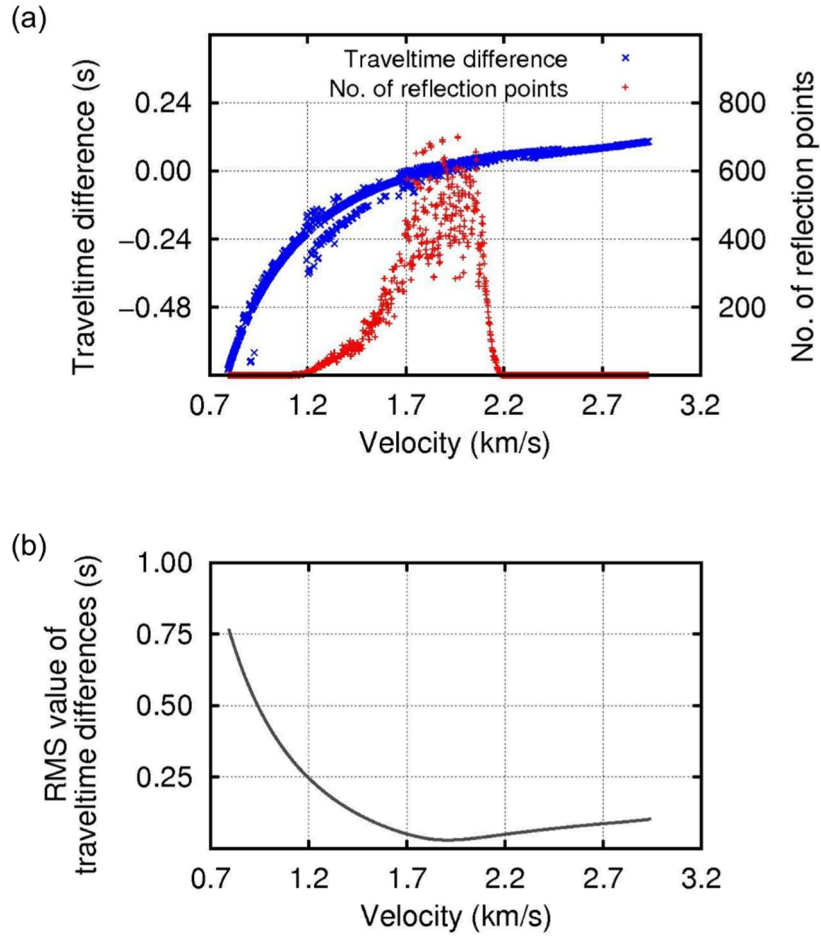


Figure 5.5 (a, b) Velocity and (c) interface estimation of the second layer for the homogeneous-layer model by applying M3.

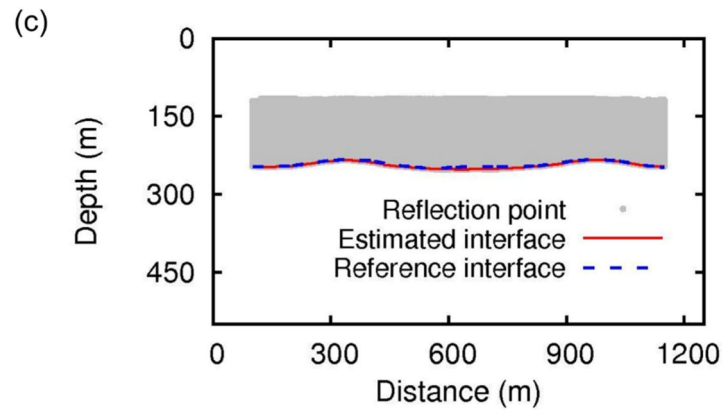


Figure 5.5 (Continued)

Figure 5.6 shows P-wave velocity images inferred by M1, M2 and M3 for the whole model. In Figure 5.7, estimated velocity-depth profiles are compared with the references at distances of 380 m and 830 m. The estimated velocity values are shown in Table 5.1. Figures 5.6 and 5.7 indicate that all of the three types of combinations can successfully estimate P-wave velocities and structures of subsurface media, although the stationary points estimated by M3 are not sufficient to determine velocities.

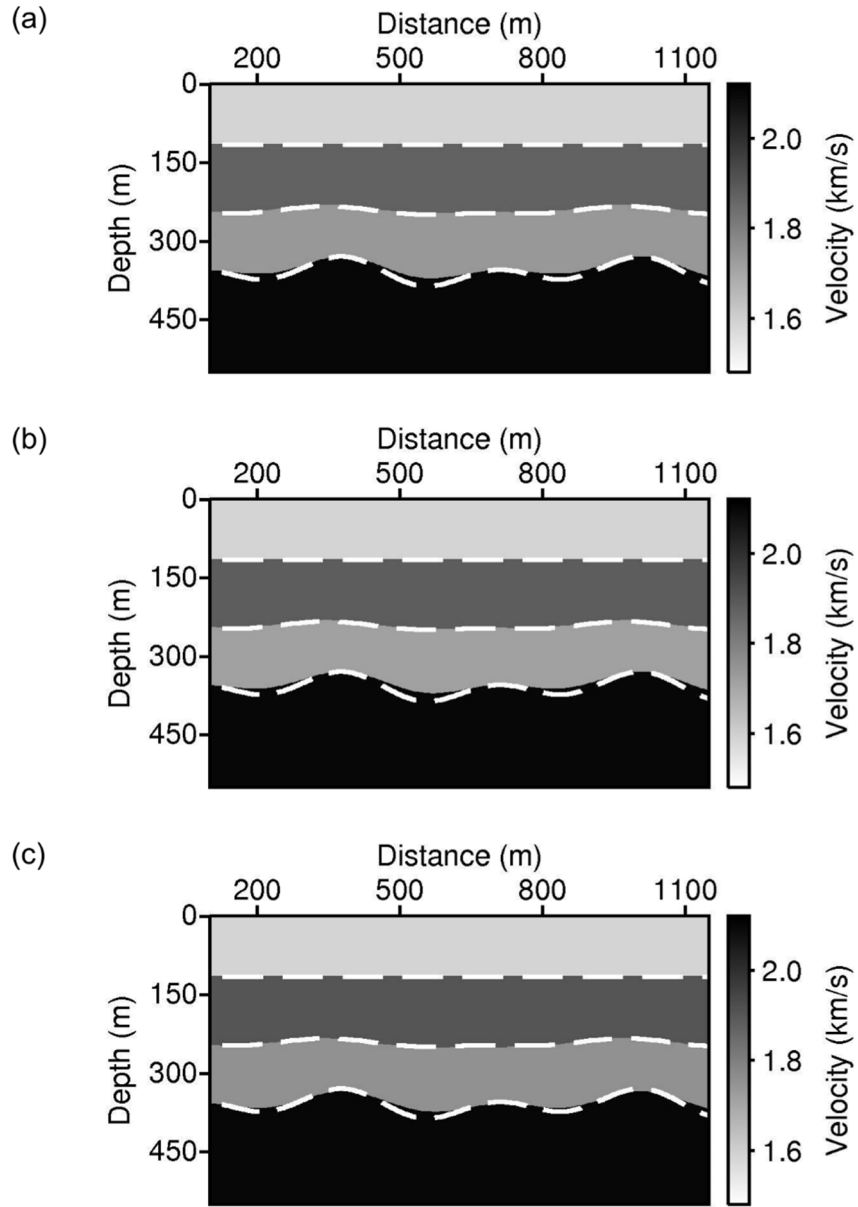


Figure 5.6 P-wave velocity images obtained by (a) M1, (b) M2 and (c) M3 for the homogeneous-layer model. The dashed white lines indicate real interfaces.

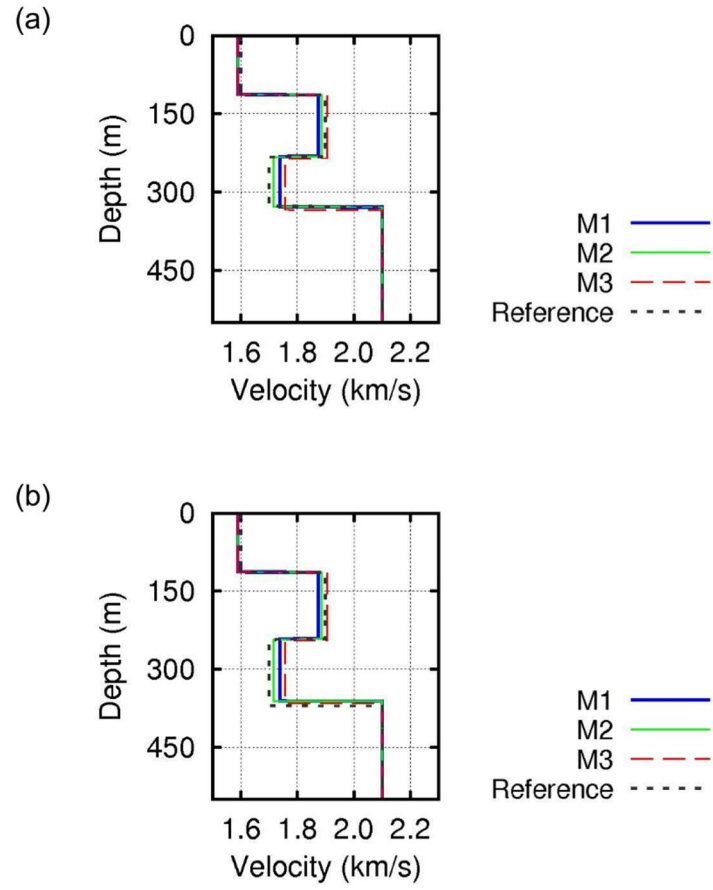


Figure 5.7 Velocity-depth profiles of velocities estimated by different types of wave combinations and references extracted at distances of (a) 380 m and (b) 830 m of the homogeneous-layer model.

Table 5.1 Velocities estimated by using three different types of combinations for the homogeneous-layer model.

	1 st layer (1.60 km/s)		2 nd layer (1.90 km/s)		3 rd layer (1.70 km/s)	
	Estimated velocity (km/s)	Error (%)	Estimated velocity (km/s)	Error (%)	Estimated velocity (km/s)	Error (%)
M1	1.5873	0.79	1.8730	1.42	1.7380	2.24
M2	-	-	1.8857	0.75	1.7141	0.83
M3	-	-	1.9063	0.33	1.7557	3.28

5.2 The inhomogeneous-layer model

To verify feasibility of the different types of wave combinations for inhomogeneous-layer models, I apply three different combinations to the model whose velocity is gradually increasing in each layer (Figure 4.5). To estimate velocity and structure, I use the same way that was applied for the homogeneous-layer model.

Figure 5.8 shows velocities and interfaces estimated by M2 (estimated velocity is 2.088 km/s) and M3 (estimated velocity is 2.126 km/s) for the second layer. (The first and second layers estimated by M1 are shown in the previous chapter.)

Figure 5.9 shows the P-wave velocity images inferred by the three combinations of waves for the whole inhomogeneous-layer model. In Figure 5.10, I compare the estimated velocities and structures with the references. The estimated velocities are not correct (Figure 5.10 and Table 5.2) because I estimate velocities by assuming that velocity is constant in each layer. However, the recovered interfaces match well with the references (Figures 5.9 and 5.10).

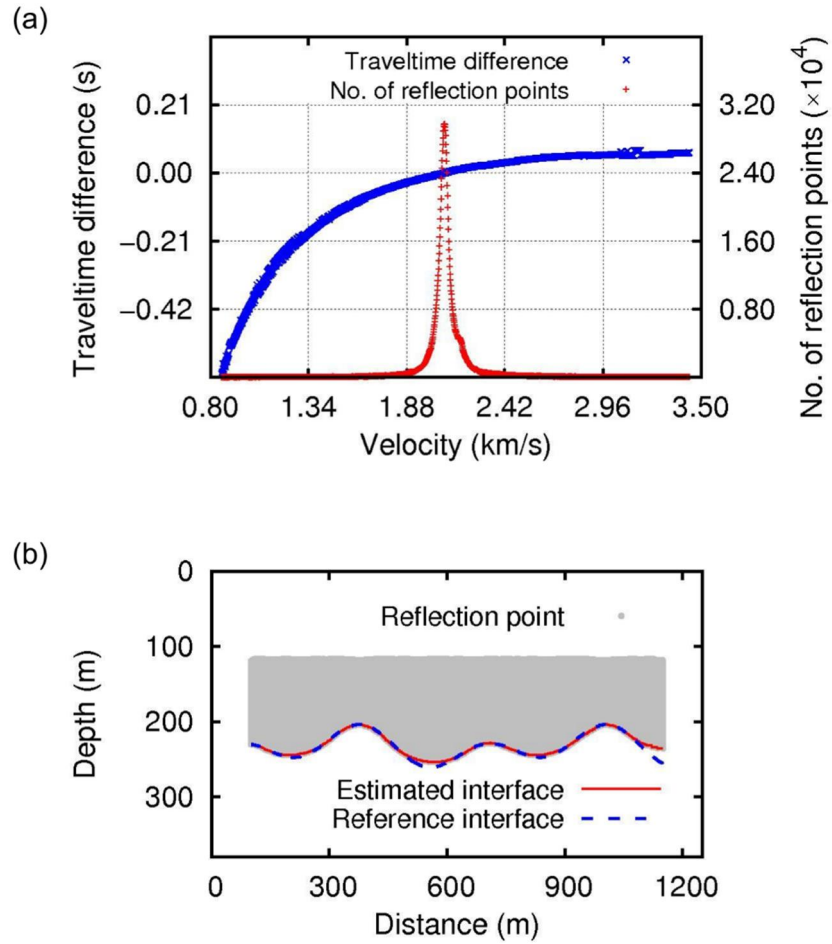


Figure 5.8 Estimation of (a, c) velocity and (b, d) interface for the second layer of the inhomogeneous-layer model with (a, b) M2 and (c, d) M3.

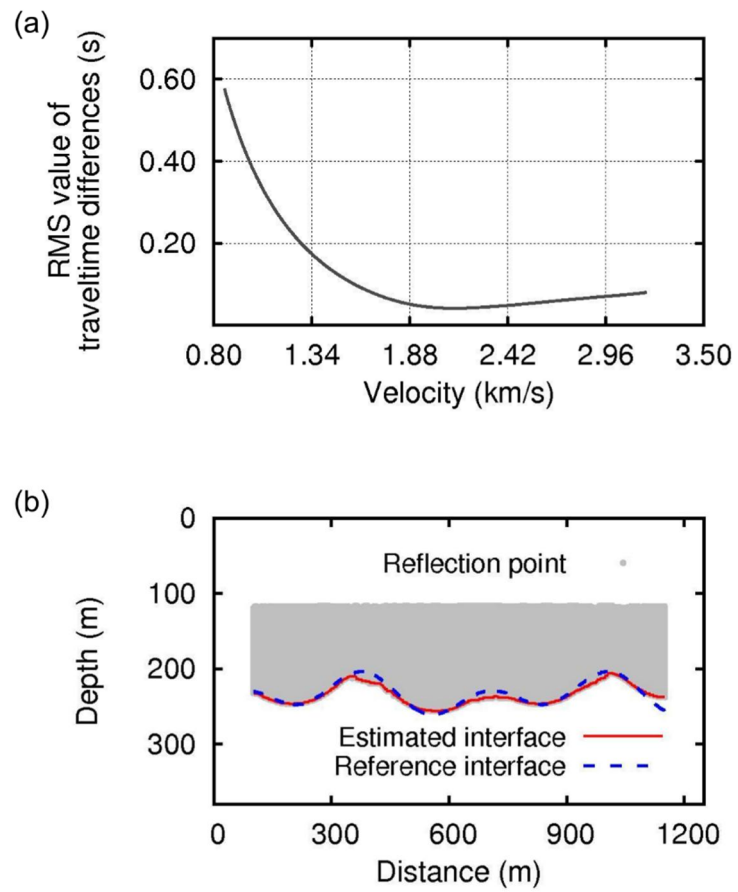


Figure 5.8 (Continued)

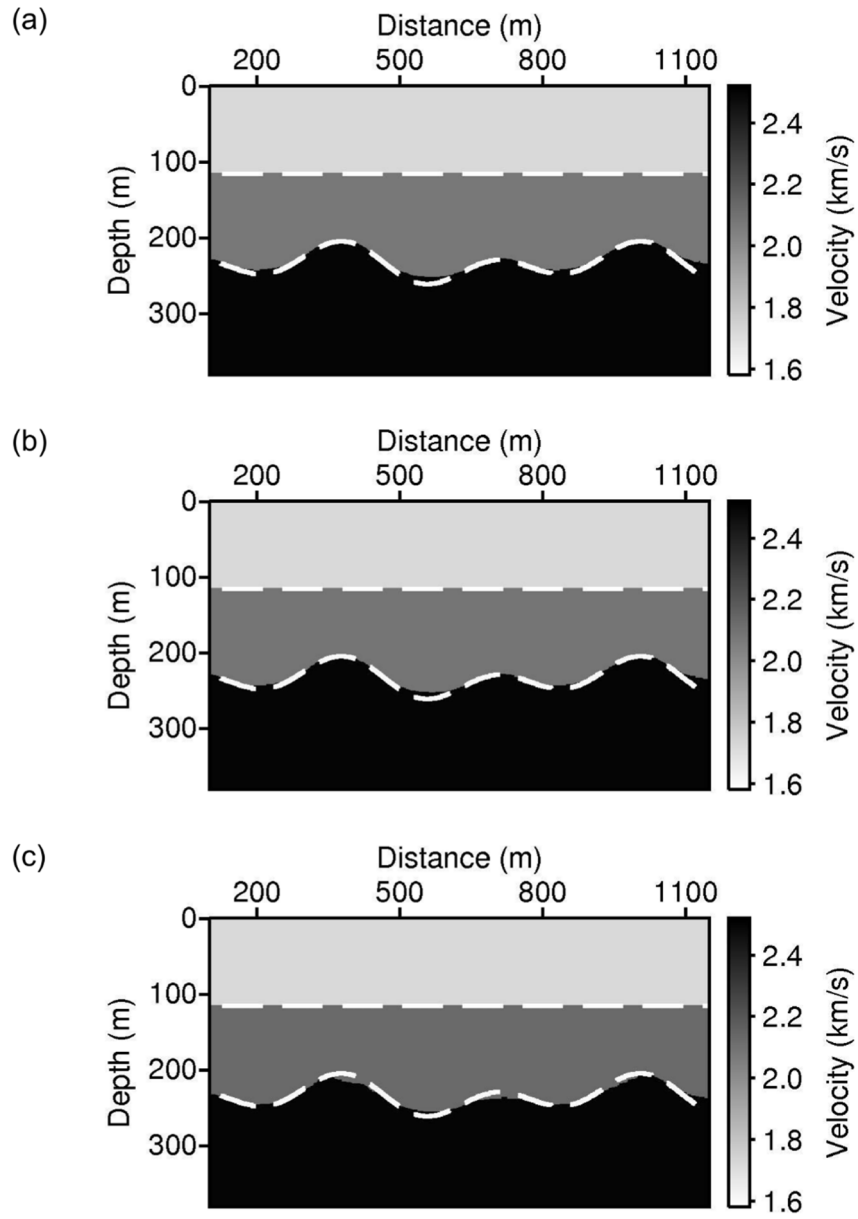


Figure 5.9 P-wave velocity models obtained by (a) M1, (b) M2 and (c) M3 for the inhomogeneous-layer model. The dashed white lines indicate real interfaces.

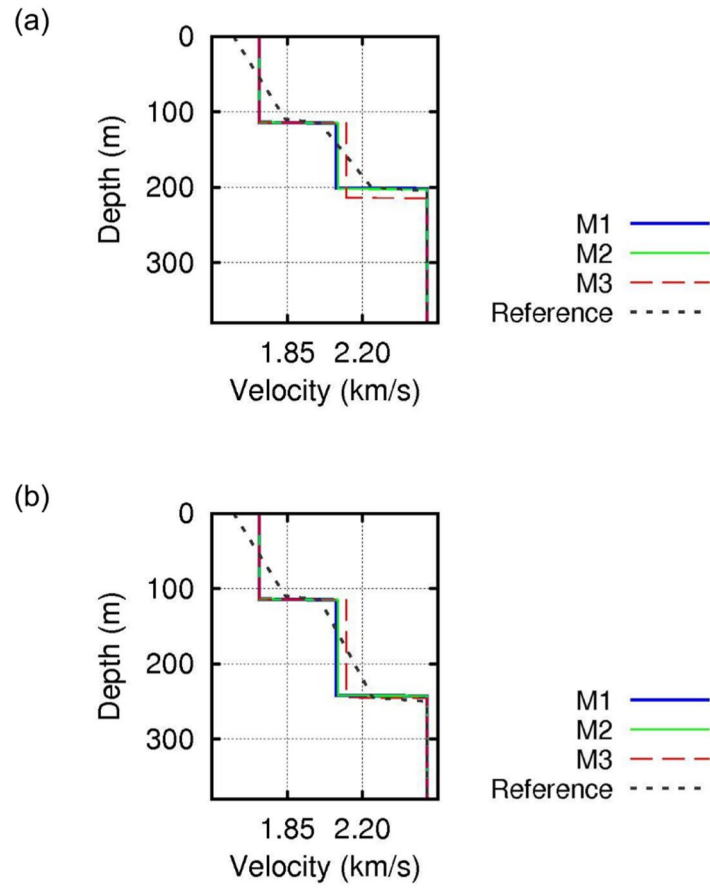


Figure 5.10 Velocity-depth profiles estimated by different types of wave combinations and references extracted at distances of (a) 380 m and (b) 830 m of the inhomogeneous-layer model.

Table 5.2 Velocities estimated by using three different types of combinations for the inhomogeneous-layer model.

	velocity of the 1 st layer (km/s)	velocity of the 2 nd layer (km/s)
Reference	1.6 ~ 1.85	2.0 ~ 2.25
M1	1.718	2.076
M2	-	2.088
M3	-	2.126

5.3 Discussion

In the process of determining stationary points based on SI, we can use various combinations of waves. Among them, I dealt with three cases: convolution of direct wave and primary reflection with an additional virtual layer (M1), cross-correlation of direct wave and primary reflection (M2) and convolution of primary reflections (M3).

Comparing M2 and M3 with M1 for the homogeneous- and inhomogeneous-layer models, we noted that M1 and M2 are better than M3. In particular, M2 gives more accurate P-wave velocity structures than the other methods, which is because the estimated stationary points are closer to the target layer to be resolved (i.e., redatumed sources and receivers are close to the target layer). On the other hand, M3, based on convolution of primary reflections, does not generate sufficient amount of stationary points, velocity inferred by the number of reflection points has a range of values rather than a specific value. As a result, the RMS value of traveltime differences was considered as well as traveltime differences themselves. Considering that while M2 requires information of the first layer and also requires redatuming of the sources and receivers, M1 does not require any information of subsurface media, I think that M1 is better than the other methods in recovering P-wave velocity structures if the recorded data is enough.

6 Conclusions

I propose a subsurface imaging technique for efficiently estimating velocities and depth structures without initial guesses. Like conventional RTT methods, the proposed method recovers the velocity and reflection surface by minimizing the differences between the observed and calculated traveltimes of primary reflections. However, by adding a virtual layer on the top of the given model and determining the incident angles based on convolution-type SI, the proposed method does not require initial guesses and mitigates the non-uniqueness problem. Once the incident angles are determined, I assume a range of velocities for the lower (target) layer and estimate the raypaths and the reflection points for each assumed velocity. When the assumed velocity is close to the real velocity, traveltime differences approach zero, and the number of reflection points with zero traveltime difference becomes large. Based on these characteristics, I determine the layer velocities, from which reflection surfaces are recovered.

The numerical examples show that the proposed method successfully reconstructs the velocities and reflection surfaces of the homogeneous model. For the inhomogeneous model, although the velocity is not correctly estimated, layer interfaces are well reconstructed. In the experiment with real field data, although the data may not be sufficient, the estimated velocity is adequate to be used as a background velocity model for migration. In addition, unlike conventional ray-based RTT in the data domain, the proposed velocity estimation method is not sensitive to the

accuracy of traveltime picking, although interface estimation is slightly affected by inaccurate traveltimes. As a result, if we cannot pick traveltimes accurately, I propose using a subsequent imaging technique such as migration to properly recover reflection surfaces. However, because the number of reflection points decreases as we move to the lower layers, the accuracy of estimating the velocity and interface will decrease. Accordingly, the proposed method may not be suitable for complicated models with many layers.

The proposed method can be used to mitigate nonlinearity and uncertainty for seismic inverse problems. Subsurface images obtained by the proposed method can be used as initial guesses for conventional imaging techniques. For example, in elastic multi-parameter inversion, the P-wave velocity estimated by the proposed method can be used to invert other parameters, such as the S-wave velocity and density. Further study is needed to modify the proposed method so that the whole media can be recovered simultaneously rather than sequentially.

References

- Bakulin A. and Calvert R. 2004. Virtual source: New method for imaging and 4D below complex overburden. 74th Annual International Meeting, SEG, Expanded Abstracts, 2477-2480.
- Bakulin A. and Calvert R. 2006. The virtual source method: Theory and case study. *Geophysics* 71, SI139-SI150.
- Brossier R., Operto S. and Virieux J. 2009. Seismic imaging of complex onshore structures by 2D elastic frequency-domain full-waveform inversion. *Geophysics* 74, WCC105-WCC118.
- Cameron M. K., Fomel S. B. and Sethian J. A. 2007. Seismic velocity estimation from time migration. *Inverse Problems* 23, 1329-1369.
- Campillo M. and Paul A. 2003. Long-range correlations in the diffuse seismic coda. *Science* 299, 547-549.
- Dong S. and Hanafy S. 2008. Interferometric interpolation and extrapolation of sparse 2D OBS data. UTAM Annual Meeting, 3-18.
- Draganov D., Wapenaar K. and Thorbecke J. 2006. Seismic interferometry: Reconstructing the earth's reflection response. *Geophysics* 71, SI61-SI70.
- Draganov D., Wapenaar K., Mulder W., Singer J. and Verdel A. 2007. Retrieval of reflections from seismic background-noise measurements. *Geophysical Research Letters* 34, L04305.

- Draganov D., Campman X., Thorbecke J., Verdel A. and Wapenaar K. 2009. Reflection images from ambient seismic noise. *Geophysics* 74, A63-A67.
- Dragoset B., Verschuur E., Moore I. and Bisley R. 2010. A perspective on 3D surface-related multiple elimination. *Geophysics* 75, 75A245-75A261.
- Gerstoft P., Sabra K. G., Roux P., Kuperman W. A. and Fehler M. C. 2006. Green's functions extraction and surface-wave tomography from microseisms in southern California. *Geophysics* 71, SI23-SI31.
- Gholami Y., Brossier R., Operto S., Prieux V., Ribodetti A. and Virieux J. 2013. Which parameterization is suitable for acoustic vertical transverse isotropic full waveform inversion? Part 2: Synthetic and real data case studies from Valhall. *Geophysics* 78, R107-R124.
- Hanafy S. M. and Schuster G. T. 2014. Interferometric interpolation of sparse marine data. *Geophysical Prospecting* 62, 1-16.
- Hondori E. J., Mikada H., Asakawa E. and Mizohata S. 2015. A new initial model for full waveform inversion without cycle skipping. 85th Annual International Meeting, SEG, Expanded Abstracts, 1446-1450.
- Jones I. F. 2010. Tutorial: Velocity estimation via ray-based tomography. *First Break* 28, 45-52.
- Lambaré G., Herrmann P., Guillaume P., Zimine S., Wolfarth S., Hermant O. and Butt S. 2007. From time to depth imaging with 'Beyond Dix'.

First Break 25, 71-76.

- Li S. and Fomel S. 2015. A robust approach to time-to-depth conversion and interval velocity estimation from time migration in the presence of lateral velocity variations. *Geophysical Prospecting* 63, 315-337.
- Lin F. C., Ritzwoller M. H., Townend J., Bannister S. and Savage M. K. 2007. Ambient noise Rayleigh wave tomography of New Zealand. *Geophysical Journal International* 170, 649-666.
- Moser T. J. 1991. Shortest path calculation of seismic rays. *Geophysics* 56, 59-67.
- Oh J. W. and Min D. J. 2013. Weighting technique using backpropagated wavefields incited by deconvolved residuals for frequency-domain elastic full waveform inversion. *Geophysical Journal International* 194, 322-347.
- Pon S. and Lines. L. R. 2004. Sensitivity analysis of seismic depth migrations: Canadian structural model. 2004 CSEG National Convention, Abstracts.
- Prieux V., Lambaré G., Operto S. and Virieux J. 2013. Building starting models for full waveform inversion from wide-aperture data by stereotomography. *Geophysical Prospecting* 61, 109-137.
- Roux P., Moreau L., Lecointre A., Hillers G., Campillo M., Ben-Zion Y., Zigone D. and Vernon F. 2016. A methodological approach towards high-resolution surface wave imaging of the San Jacinto Fault Zone

- using ambient-noise recordings at a spatially dense array. *Geophysical Journal International* 206, 980-992.
- Russell B. 1998. A simple seismic imaging exercise. *The Leading Edge* 17, 885-889.
- Schuster G. T. 2001. Theory of daylight/interferometric imaging: Tutorial. 63rd Conference and Exhibition, EAGE, Extended Abstracts, A032.
- Schuster G. T. 2005. Fermat's interferometric principle for target-oriented traveltimes tomography. *Geophysics* 70, U47-U50.
- Schuster G. T. 2009. Seismic interferometry. *Cambridge University Press*.
- Shapiro N. M., Campillo M., Stehly L. and Ritzwoller M. H. 2005. High-resolution surface-wave tomography from ambient seismic noise. *Science* 307, 1615-1618.
- Shin C. and Min D. J. 2006. Waveform inversion using a logarithmic wavefield. *Geophysics* 71, R31-R42.
- Shin C. and Cha Y. H. 2008. Waveform inversion in the Laplace domain. *Geophysical Journal International* 173, 922-931.
- Shin C. and Cha Y. H. 2009. Waveform inversion in the Laplace-Fourier domain. *Geophysical Journal International* 177, 1067-1079.
- Taillandier C., Noble M., Chauris H. and Calandra H. 2009. First-arrival traveltimes tomography based on the adjoint-state method. *Geophysics* 74, WCB57-WCB66.

- Trinks I., Singh S. C., Chapman C. H., Barton P. J., Bosch M. and Cherrett A. 2005. Adaptive travelttime tomography of densely sampled seismic data. *Geophysical Journal International* 160, 925-938.
- Vesnaver A. L. 1996. Irregular grids in seismic tomography and minimum-time ray tracing. *Geophysical Journal International* 126, 147-165.
- Wapenaar K. and Fokkema J. 2006. Green's function representations for seismic interferometry. *Geophysics* 71, SI33-SI46.
- Wapenaar K., Draganov D., Snieder R., Campman X. and Verde A. 2010. Tutorial on seismic interferometry: Part 1—Basic principles and applications. *Geophysics* 75, 75A195-75A209.
- Wéber Z. 2001. Optimizing model parameterization in 2D linearized seismic travelttime tomography. *Physics of the Earth and Planetary Interiors* 124, 33-43.
- Wu R. S., Luo J. and Wu B. 2014. Seismic envelope inversion and modulation signal model. *Geophysics* 79, WA13-WA24.
- Xiao X. and Schuster G. T. 2006. Redatuming CDP data below salt with VSP Green's function. 76th Annual International Meeting, SEG, Expanded Abstracts, 3511-3515.
- Xu Z, Juhlin C., Gudmundsson O., Zhang F., Yang C., Kashubin A. and Lüth S. 2012. Reconstruction of subsurface structure from ambient seismic noise: an example from Ketzin, Germany. *Geophysical Journal International* 189, 1085-1102.

- Yu J. and Schuster G. T. 2006. Crosscorrelogram migration of inverse vertical seismic profile data. *Geophysics* 71, S1-S11.
- Zhang F., Juhlin C. and Sopher D. 2014. Passive seismic ambient noise correlation: an example from the Ketzin experimental CO₂ storage site, Germany. *Energy Procedia* 59, 90-96.
- Zhao A., Zhang Z. and Teng J. 2004. Minimum travel time tree algorithm for seismic ray tracing: Improvement in efficiency. *Journal of Geophysics and Engineering* 1, 245-251.

초 록

근사 stationary point를 이용한 반사주시 토모그래피

반사주시 토모그래피를 이용하여 유추한 지하속도구조는 중합전심도구조보정, 완전파형역산의 초기속도모델로 사용될 수 있다. 전통적인 반사주시 토모그래피는 파선추적을 기반으로 구성된 거대한 토모그래피 행렬을 이용하여 지하물성을 유추하는데 이는 많은 메모리와 계산시간을 소요한다. 또한 전통적인 반사주시 토모그래피는 대다수의 데이터영역 토모그래피 방법과 마찬가지로 초기모델의 영향을 받으며 비유일해 문제(non-uniqueness problem)가 존재한다.

이 연구에서는 탄성과 간섭기법을 적용하여 지하매질에 대한 사전정보가 필요없이 유일해(uniqueness solution)를 제공할 수 있는 결정론적인 반사주시 토모그래피를 제안하였다. 실제 표면 위에 가상의 층(virtual layer)을 추가함으로써 컨벌루션(convolution)을 이용한 간섭기법을 적용하여 stationary point 위치, 즉 입사각을 대략적으로 추정할 수 있다. 첫 번째 층의 물성(P 과 속도 및 구조)을 알고 있으면 상호상관을 이용하여 stationary point 위치를 추정할 수도 있다. Stationary point 의 위치(입사각)가 추정되면 유추하려는 매질의 속도를 다양하게 가정함으로써 반사점 및 주시 차이를 구한다. 매질의 속도는 반사점

개수와 주시 차이를 이용하여 유추할 수 있으며 반사면은 유추한 속도를 이용하여 추정할 수 있다. 첫 번째 층을 유추하였으면 같은 방식으로 하부의 매질에 대해 제안된 방법을 적용함으로써 하부 매질의 물성값을 추정할 수 있다.

제안된 방법은 균질 및 불균질 매질에서 획득된 지표탐사 합성자료 및 해상에서 획득된 현장자료에 대해 적용하였다. 본 연구에 사용된 상호상관 및 컨벌루션을 이용한 여러 가지 지진파들의 조합(different types of wave combinations) 모두 지하매질의 속도와 구조를 성공적으로 유추할 수 있다는 것을 보여주었으며 그 중 가상층을 추가한 컨벌루션을 이용한 방법은 지하매질에 대한 사전정보 없이도 지하물성을 유추할 수 있다. 비록 제안된 방법은 비유일해 문제가 존재하지 않고 사전정보 없이도 실행 가능하지만 심도가 깊어질수록 속도 추정에 필요한 반사점을 충분히 획득하기 어렵기 때문에 다층구조모델에 적용하기 어렵다.

주요어: 반사주시 토모그래피, 역산, 속도 추정, 비유일해 문제, 파선추적, 지진파 간섭기법, stationary point, 입사각

학 번: 2013-30780